Title

Atom probe tomographic analysis of high dose oxide-dispersion strengthened steel (alloy MA957) at selected irradiation conditions

Author

Bailey, Nathan

Publication Date

2016

Peer reviewed|Thesis/dissertation

Atom probe tomographic analysis of high dose oxide-dispersion strengthened steel (alloy MA957) at selected irradiation conditions

By

Nathan Alexander Bailey

A dissertation in partial satisfaction of the requirements for the degree of

Doctor of Philosophy

in

Engineering – Nuclear Engineering

in the

Graduate Division

of the

University of California, Berkeley

Committee in charge:

Professor Rachel Slaybaugh, Chair

Professor Peter Hosemann

Professor Per Peterson

Professor Mark Asta

Summer 2016

Abstract

Atom probe tomographic analysis of high dose oxide-dispersion strengthened steel (alloy MA957) at selected irradiation conditions

by

Nathan Alexander Bailey

Doctor of Philosophy in Nuclear Engineering

University of California, Berkeley

Professor Rachel Slaybaugh, Chair

In an effort to understand the effect of high dose neutron irradiation on fast reactor cladding candidate materials, oxide-dispersion strengthened (ODS) alloy MA957 was irradiated to doses exceeding 100 displacements per atom (dpa) at various irradiation temperatures. The finely distributed Y-Ti-O particles, which provide MA957 its attractive properties, were examined by atom probe tomography (APT). Significant increases in oxide cluster number density and reductions in oxide cluster size were observed in specimens irradiated at 412 °C and below. A substantial hardness increase, measured by nanoindentation, was also observed at these low irradiation temperatures. It was found that the increase in oxide cluster number density, reduction in oxide cluster size, and associated increase in hardness is due to the inhibition of reformation processes of the Y-Ti-O particles following ballistic dissolution by incident radiation. Redistribution of oxide particle material along the grain boundaries is also observed at the low irradiation temperatures. The intermetallic phase α' was observed in the low temperature samples. This observation of this phase provides additional experimental evidence for the location of the phase boundary for this low temperature precipitate. The conclusion of this work is that MA957 is microstructurally stable under neutron irradiation at and above 495 °C.

Contents

Dedication

This work is dedicated to my wife, Justine Harlan, for her unending love and support throughout not only graduate school, but all of my life.

List of tables

List of figures

Acknowledgements

I would like to thank my advisor, Prof. Peter Hosemann, for his sage advice and direction during my thesis work and the drafting of this dissertation. His help has been invaluable in my development as a scientist, and as a person.

I would also like to thank my thesis committee; Prof. Rachel Slaybaugh, Prof. Per Peterson, Prof. Mark Asta and Prof. Peter Hosemann, for their counsel and guidance through the experimental processes described herein.

I would also like to thank the institutions which fostered my scientific development during my thesis work; University of California at Berkeley, Pacific Northwest National Laboratory, University of California at Santa Barbara, Center for Advanced Energy Studies, Idaho National Laboratory.

I would also like to thank the organizations which funded me and my experiments for the duration of my thesis work: Nuclear Energy University Program, Pacific Northwest National Laboratory.

I would like to thank Mychailo Toloczko for providing me access to the samples upon which my thesis work is based.

Finally, I would like to thank all those who lent an ear, offered advice, and gave me perspective during my time in graduate school. These people were instrumental in my success; Peter Hosemann, Mychailo Toloczko, Erich Stergar, Alicia Certain, Peter Wells, Nicholas Cunningham, Daniel Schreiber, Krishna Rajan, Rachel Slaybaugh, Melissa Teague, Yaqaio Wu, Joanna Taylor, Jeff Benson, David Frazer, Scott Parker, Ashley Reichardt, Jeff Bickel, Amanda Lupinacci, Brian Phan, Mitch Loff, Madicken Munk, Justine Harlan, Hi Vo, G. Robert Odette, Yuan Wu.

1 Motivation

1.1 Modern nuclear energy landscape

Future energy requirements

With global energy needs at an all-time high, innovation in all areas of energy production is vital. World-wide, nuclear energy is seeing renewed interest as an element to the solution to global warming while expanding electricity production. This excitement, however, is tempered by the aftermath of the Fukushima Daiichi nuclear power plant accident [1]. Further development of nuclear technology is necessary to answer the global energy demand, while mitigating the risk of future accidents and assuaging public opinion on nuclear energy. Current light water reactor (LWR) designs have the drawback of an open fuel cycle, a system where enriched fuel is consumed to generate power, and when the fissile material has been depleted the fuel is disposed of in a repository facility. Concerns about the safety and proliferation risks associated with repositories and the storage of spent fuel prior to transfer to repositories have garnered interest in reactor designs that reduce or eliminate this type of nuclear waste generation.

Generation IV International Forum

The Generation IV International Forum (GIF) was created in an effort to advance nuclear energy to its "fourth" generation (Figure 1.1) [2] [3]. Four goal areas were defined to advance nuclear power to its next stage: sustainability; safety and reliability; economic competitiveness; and proliferation resistance and physical protection. In terms of sustainability, the strategy revolves around closing the nuclear fuel cycle (e.g. reprocessing spent nuclear fuel to reclaim fissile material and creating from it new fuel forms). Many of the advanced fuel cycles use fast-spectrum reactors and, with recycling, there is potential to breed fissile material in such a way that the reactor produced more fissile material than

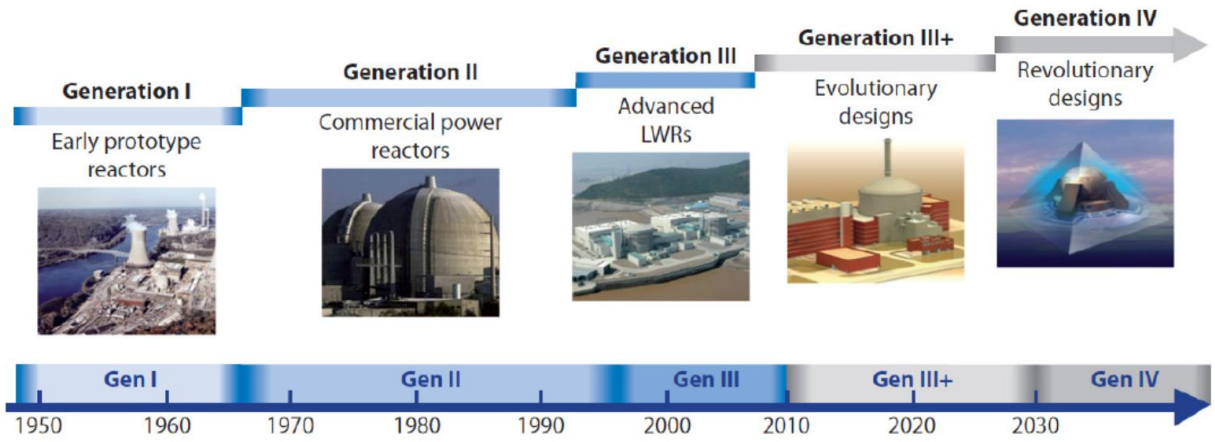

Figure 1.1 Evolution of nuclear power. The time ranges estimate the design and initial deployment of the different reactor generation.

it consumes. Such a closed fuel cycle has the added benefit of significantly reducing the production of ultimate waste (waste that can no longer be reprocessed) to be conferred to the spent fuel repositories. Furthermore, advanced separation technologies can enhance proliferation resistance by designing separation features that avoid the separation of sensitive materials.

Fast spectrum reactors

In the roadmap laid out by GIF, a number of the advanced reactor designs use fast spectrum (high energy) neutrons to initiate fission in the fuel. Such fast spectrum reactors are attractive designs for a number of reasons, but one of the biggest advantages is the ability to support a closed nuclear fuel cycle. Fast spectrum reactors are able to burn fuel that has been reprocessed, and in some cases are able to breed new fissile material for further reprocessing.

Table 1.1 Outlet temperatures of GIF fast spectrum reactor designs.

System	Outlet Temperature
Gas-Cooled Fast Reactor	850 °C
Lead-Cooled Fast Reactor (near term)	550 °C
Lead-Cooled Fast Reactor (far term)	800 °C
Sodium-Cooled Fast Reactor	510 – 550 °C
Supercritical-Water-Cooled Reactor	550 °C

However, the fast spectrum reactors elicit unique challenges in development. The advanced reactor designs put forward by GIF require outlet temperatures as high as 510 – 850 °C, in contrast to the LWR temperature range of 250 – 350 °C [4] [5]. This increase in temperature greatly increases the thermal load put on the reactor core internals, such as the fuel cladding material. Consequently, the fuel cladding in these reactors will be facing an operational environment without precedent [6] [7] [8].

In addition to increased operating temperatures, many of the GIF reactor designs are based on fast fission. Fast neutrons deposit considerably more energy into the cladding per evolved fission neutron, and therefore increase the dose per neutron [9]. The lifetime dose that cladding materials receive in a fast reactor core is substantially higher than that seen in thermal reactor environments [10]. Therefore, many aspects of fast reactor design are materials limited, driving the exploration of cladding material response to high dose neutron irradiation at elevated temperature. Most experience in radiation damage in materials is based on thermal reactor components, comparatively little is known about response to fast neutrons, and therein high dose materials. This dissertation focuses on understanding the effect of high dose neutron irradiation on a potential cladding material for fast reactors.

1.2 Fast reactor cladding development

Cladding

Cladding material is generally metal, although some ceramic cladding systems have been suggested such as silicon-carbide ceramic composites [11]. In reactor designs that require cladding, most designs fill the space between the cladding and fuel with helium to enhance heat transport from the fuel to the coolant and leave space for fuel swelling. A number of variables affect the material property requirements of fuel cladding, including, but not limited to, strength, ductility, creep resistance, swelling resistance, fuel-clad interaction, corrosion resistance, machinability, and joinability [12]. Each of these material properties is critical for cladding performance, but in this work the focus is on the response of the cladding material to radiation at the end of the cladding's useful life.

Cladding lifetime limiting factors

By examining the list of cladding material properties, it can be seen that the properties fall into two categories, functional properties and evolutionary properties. Functional properties are properties such as strength, ductility, machinability, and joinability. These properties are nominally what make an alloy sufficient to perform the require task. Evolutionary properties are material properties that affect the functional properties over time, such as creep resistance, swelling resistance, fuel-clad interaction, and corrosion resistance.

The evolutionary properties of a material are of critical importance in engineering design as they determine the lifetime of a part. For example, after a particular length of time being exposed to stress at elevated temperature, a structural component will no longer have the same shape as it did when it was initially installed. The geometry of the part was changed as a result of creep, and the stresses that the component was designed to sustain become distributed differently across the part. This redistribution of stress can lead to failure of the part. Therefore, creep resistance at operating temperature is a necessary design criteria for any high temperature system; if the material's shape evolves too quickly, it will not be able to sustain the design loads over the part's lifetime.

Applying similar logic to cladding, all of the above mentioned evolutionary properties can lead to failure. However, as fast reactors began operating to doses beyond 50 dpa, swelling and irradiation induced creep have become the life-limiting degradation mechanisms for fast reactor cladding and duct materials.

In early fast reactor applications, austenitic stainless steel was the cladding material of choice. However, this type of steel was found to readily swell after only 50 dpa [13]. While cold working along with the addition of selected solutes enhanced the resistance to swelling and creep up to 150 dpa, the desire for performance to even higher doses led to the discovery that ferritic steels were more swelling resistant [14]. However, the ferritic steels under investigation at that time were thought to be more susceptible to creep at higher irradiation temperatures than austenitic stainless steels. Attempts to obtain ferritic

steel with good swelling and high temperature creep resistance led to the concept of using ferritic oxide-dispersion strengthened (ODS) alloys as cladding material.

1.3 Assessing cladding viability

Mechanical property evolution

For any cladding system to be feasibly integrated into a reactor design, its properties must not only satisfy initial design criteria (tensile strength, ductility, etc.) but also maintain the performance throughout its operation lifetime. In order to adequately assess the viability of ferritic ODS alloys as a cladding material in modern fast reactor designs, the mechanical property evolution as a function of operating conditions must be evaluated.

Cladding material validation

Since the high temperature strength and creep resistance of ODS alloys is controlled by the properties and distribution of the dispersed oxide particles, it is of great interest to understand how the oxide particles evolve as a function of reactor operating condition, as changes to the oxides will likely correlate to a change in mechanical properties of the alloy.

Therefore, both mechanical testing and high-resolution microscopy at near end-of-life operating conditions are necessary to validate the feasibility of ODS alloys as fast reactor cladding material. Furthermore, an improved scientific understanding of the changes to the oxides at high doses is expected to allow design of new materials, allowing even higher dose to be achieved.

1.4 Hypothesis

Embrittlement through solute dissolution

This work will support the hypothesis that under neutron irradiation, the oxide particles, which control the desirable mechanical properties and creep resistance of ODS alloy MA957, will undergo ballistic dissolution by the incident neutrons. When enough thermal energy is available, it is expected that the dissolved oxide solutes will be able to reform. However, at low irradiation temperatures; this reformation process will be limited, leading to an increase in oxide particle number density and reduction in size. Therefore, at low irradiation temperatures, it is hypothesized that the MA957 will harden and embrittle, according to the redistribution of oxide solutes within the grain bulk and along the grain boundaries.

1.5 Summary

Mechanical property detriment in high dose MA957 irradiated below 412 °C

Using samples irradiated to high neutron dose (~100 dpa), the mechanical properties of ODS alloy MA957 are investigated using nanoindentation and the microstructural characteristics of the property-controlling Y-Ti-O oxide particles were investigated using APT. This evidence will show that specimens irradiated at 412 °C and below exhibit increased hardness, as well as increased oxide particle number density and reduced oxide particle size. Evidence in support of the hypothesis will be shown in the redistribution of oxide solutes along the grain boundaries in specimens irradiated at 412 °C and below. In addition, intermetallic phase separation of chromium into α' will be illustrated in specimens irradiated at 412 °C and below.

1.6 Outline

Background

The background section of this document will layout the theoretical and historical context for the concepts explored in this dissertation. It will discuss radiation damage and its consequences in materials; as well as discuss creep and the ways that ODS alloys combat the phenomena. This section will also lay out foundational mechanical property work conducted previously by collaborating researchers on these materials.

Experiment

This section will lay out the irradiation conditions and the sample preparation techniques that were used for this work. This section will detail the nanoindentation technique and experimental parameters utilized. It will also detail the APT technique, and summarize modern data analysis techniques for the interpretation of APT results.

Results

This section will describe the results of the nanoindentation experiment and lay out the results of the APT data collection.

Discussion

This section will interpret the results of the nanoindentation and APT, and relate them to the broader context of the materials performance. It will detail extensions and improvements to APT data analysis techniques that were specifically developed to address the problems in this manuscript. It will comment on theoretical explanations for the observations laid out in the results section. It will also detail aspects of the APT results that

were surprising and suggest where some of the information contained could be applied outside of direct use for cladding material validation.

Conclusion

This section will summarize the concepts laid out in the discussion, and describe the impact that this work will have on the field of nuclear materials study.

2 Background

2.1 Radiation damage in materials

Introduction

In this work, the discussion of radiation damage is limited to the effect of ionizing radiation on crystalline metals. Since most structural materials considered in reactor design fall within this category, the discussion applies to all structural metals such as fuel cladding, core internals and the reactor pressure vessel, etc.

Transmutation

When particles with sufficiently high energy collide with atomic nuclei, a nuclear reaction can occur. Nuclear reactions occur in several modes. In some cases, the incident particle transfers enough energy to the nucleus to raise its energy state, and when the nucleus returns to its ground state, a gamma ray is emitted. In other cases, the incident particle will be absorbed by the target nucleus, transmuting the lattice atom into another element or isotope, sometimes this process results in the emission of other particles. It is the change of one element into another by way of a nuclear reaction that is referred to as transmutation. Since transmutation is quite complex, the discussion will only highlight nuclear reactions that have a significant effect on the mechanical properties of the material.

In steel, under a fast spectrum neutron flux, transmutation of alloying elements does not typically happen in high enough quantities to have an effect on the thermodynamic stability of the alloy. However, reactions in which a neutron is absorbed on a target nucleus and produces an alpha particle (termed (n, α) reactions) do have a significant effect on the mechanical properties of the alloy. An α particle is a helium nucleus which is stripped of electrons. When this particle is ejected following an (n, α) reaction, it quickly captures two electrons from the surrounding metal matrix to form a helium atom. Helium is only soluble in iron in extremely low quantities, leading to subsequent extended defects and therefore microstructure and dislocation interactions.

Point defect production

Point defects come in two varieties, a vacancy (an unoccupied lattice site) or an interstitial (a lattice atom that is not occupying a lattice site). A vacancy-interstitial couple is another related concept and is referred to as a Frenkel pair. Typically, vacancies are generated by the thermal agitation of the crystal. The concentration of these unoccupied lattice sites is

dependent on the degree of thermal agitation, in other words, the temperature. Thermodynamically, this fraction of unoccupied lattice sites is known as the equilibrium vacancy concentration. In fields of ionizing radiation, incident high energy particles on a crystal lattice have the potential to generate point defects concentrations in excess of the equilibrium value. These excess point defects are generated by the incident particle striking an atom and displacing it from its lattice site: this produces a Frenkel pair.

Atoms held in a crystal lattice must overcome an energy barrier in order to move from their lattice site. This energy barrier is termed the displacement energy (E_d). When a high energy particle strikes an atom lying in the crystal lattice, if the scattering angle and incident energy are such that the energy transferred to the lattice atom exceeds E_d, then the atom will be knocked out of its lattice site. If the energy of the displaced atom is much higher than E_d, then a so-called displacement cascade will occur. In a displacement cascade, the initially displaced atom (the primary knock-on atom or PKA) displaces an adjacent atom, which displaces an adjacent atom to it, and so on until the energy is dissipated. A simulated displacement cascade from [15] is illustrated in Figure 2.1.

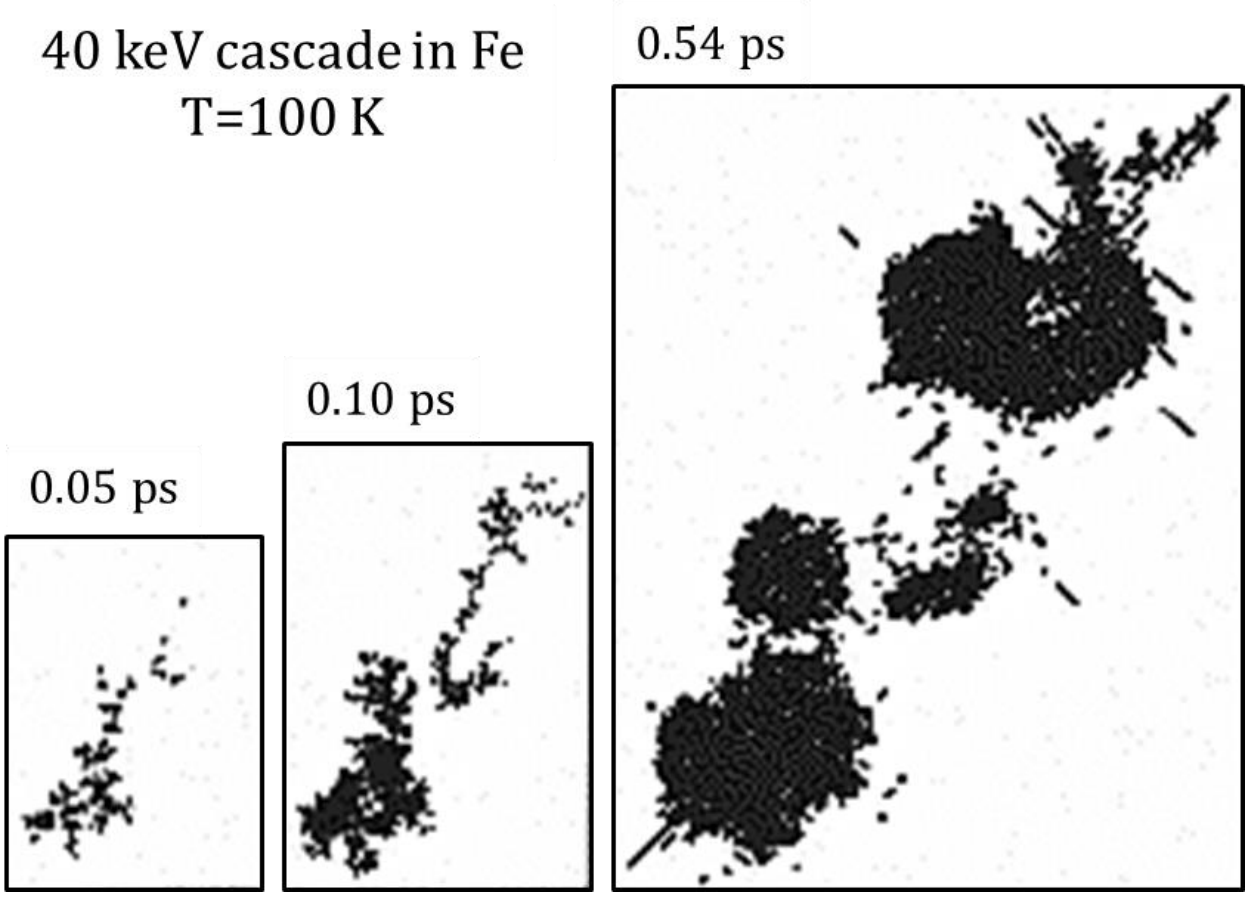

Figure 2.1 Displacement cascade simulation of the impact of a 40 keV iron ion on BCC iron at 100 K. The three images show the time evolution of the defect structures (the dark areas) after the initial displacement *[15]*.

Quantifying radiation damage

One of the first steps to understanding how radiation damage affects other material properties, such as strength or ductility or even corrosion resistance, is to develop a metric that can describe radiation damage.

Initially, scientists would report the reactor energy spectrum, flux profiles and fluences of the core in order to show all the variables controlling the properties of the incident particles and therefore, the generated displacements over the irradiation period. But, this provided little comparability between experiments, as each reactor was different, and even within one reactor, the position of the materials in the reactor core could change the flux, fluence and particle energies that affected each area. Therefore, radiation damage was parameterized to provide a method of comparison for irradiated materials from different experiments. This parameter is described in terms of displacements per atom (dpa) and can be calculated with for example the Kinchin-Pease (KP) model [16].

The Kinchin-Pease model

The KP model for radiation damage focuses on lattice atom displacements and displacement cascades as a means to measure the amount of damage a given material has sustained [9]. When a high energy particle strikes a lattice atom, some of the particles' energy is transferred to the PKA. In the KP model, the energy transfer is based on non-relativistic binary elastic scattering [9].

An incident particle of mass M_1 with velocity v_{1o}, approaches a stationary particle of mass M_2. Figure 2.2a shows the system in the laboratory frame reference. The equations describing the interaction can be simplified by transforming the coordinates to a moving center-of-mass reference frame. The velocity of the center-of-mass reference frame is given by:

$$v_{cm} = \left(\frac{M_1}{M_1 + M_2}\right) v_{1o}$$

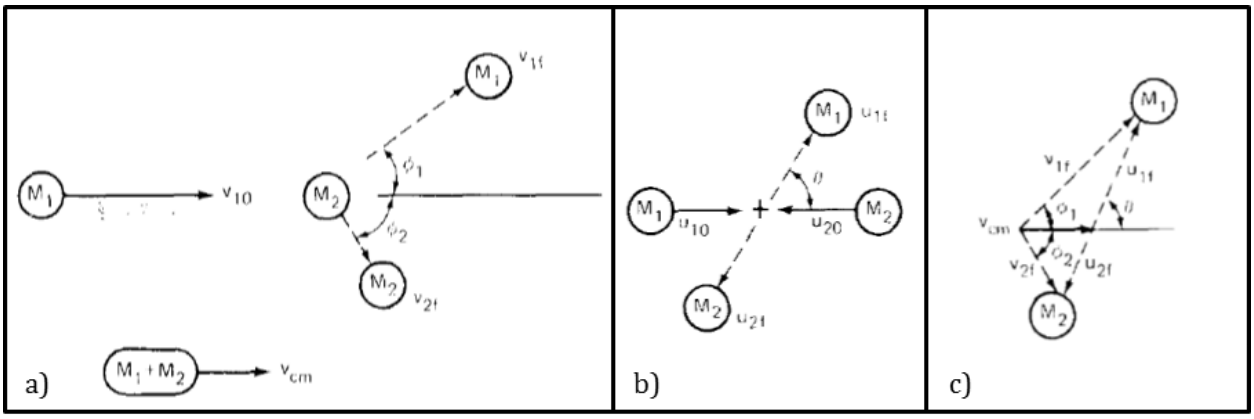

Figure 2.2 Binary elastic collision between particles a) laboratory reference frame b) center-of-mass reference frame c) Vector diagram relating the reference frames in a) and b). Reproduced from *[9]*.

Figure 2.2b shows the interaction in the new reference frame. The direction of the two particles are opposite in the center-of-mass reference frame and the scattering angle is given by θ. The initial speeds in the center-of-mass frame are given by:

$$u_{1o} = v_{1o} - v_{cm}$$

$$u_{2o} = v_{cm}$$

Conservation of momentum in the center-of-mass frame yields:

$$M_1 u_{1o} + M_2 u_{2o} = M_1 u_{1f} + M_2 u_{2f}$$

Conservation of energy yields:

$$\frac{1}{2} M_1 u_{1o}^2 + \frac{1}{2} M_2 u_{2o}^2 = \frac{1}{2} M_1 u_{1f}^2 + \frac{1}{2} M_2 u_{2f}^2$$

The conservation of energy and momentum require the following relations to be true:

$$u_{1f} = u_{1o} = v_{1o} - v_{cm}$$

$$u_{2f} = u_{2o} = v_{cm}$$

Figure 2.2c shows a vector diagram of the system after the collision, which allows determination of the final velocities of the particles after the collision. By vector addition:

$$v_{1f} = u_{1f} + v_{cm}$$

$$v_{2f} = u_{2f} + v_{cm}$$

Magnitudes of the final velocity vectors can be found by applying the law of cosines to Figure 2.2c:

$$v_{2f}^2 = v_{cm}^2 + u_{2f}^2 - 2 v_{cm} u_{2f} \cos\theta - 2 v_{cm}^2 (1 - \cos\theta)$$

Which can be simplified to:

$$v_{2f}^2 = \frac{2 M_1^2 v_{1o}^2}{(M_1 + M_2)^2} (1 - \cos\theta)$$

By noticing that:

$$E = \frac{1}{2} M v^2$$

The kinetic energy of the struck particle can be written in terms of the kinetic energy of the incident particle, the masses of the two particles and the scattering angle:

$$E_{2f} = \frac{2 M_1 M_2}{(M_1 + M_2)^2} E_{1o} (1 - \cos\theta)$$

To simplify notation, a substitutions are made, E_{1o} by E, and E_{2f} by T. The ratio of the masses can also be consolidated by:

$$\Lambda = \frac{4M_1M_2}{(M_1 + M_2)^2}$$

The simplified energy transfer equation then becomes:

$$T = \frac{1}{2}\Lambda E(1 - \cos\theta)$$

The maximum energy transfer occurs with a head-on collision (θ=π):

$$T_{max} = \Lambda E$$

The average energy transfer is then:

$$T_{avg} = \frac{1}{2}\Lambda E$$

If T (the energy transferred to the PKA) exceeds E_d, then the PKA is dislodged, and a Frenkel pair is formed. If T is lower than E_d, then no displacements will occur and the energy will be dissipate through lattice vibrations or the emission of photons.

The rate of atomic displacements (R_d [=] displacements/cm^3/sec), then, is proportional to the atomic density of the target (N [=] atoms/cm^3), the displacement cross-section ($\sigma_d(E)$ [=] cm^2) and the flux ($\phi(E)$ [=] particles/cm^2/sec) of incident particles with energy E. R_d is given by:

$$R_d(E) = N * \sigma_d(E) * \phi(E)$$

The dpa is then calculated by dividing R_d by N and the irradiation time (t [=] sec):

$$dpa = \frac{R_d(E) * t}{N}$$

Calculating the cumulative neutron dose, can be achieved by integrating $\sigma_d(E_n)\phi(E_n)$ or the probability of a neutron of energy E_n displacing a lattice atom and the flux of neutrons of energy E_n with ($0 < E_n < \infty$). Of course, in any real system, the upper bound is replaced by the maximal neutron energy (E_{max}) and the lower bound is given by E_d/Λ, as neutrons with less energy will not generate a PKA and thus will not contribute to the dose. The cumulative dpa is given by:

$$dpa = t\int_{\frac{E_d}{\Lambda}}^{E_{max}} \sigma_d(E_n)\phi(E_n)dE_n$$

By summing the number of displacements initiated by PKAs of energy E_d to ΛE_{max}, $\sigma_d(E)$ can be calculated from a differential energy transfer cross section ($\sigma(E_n,E)dE$). The differential

energy transfer cross section is the interaction probability of a neutron with energy E_n producing a PKA with energy T.

$$\sigma_d(E_n) = \int_{E_d}^{\Lambda E_{max}} \sigma(E_n, T) * \nu(T) dT$$

The KP model presents a simple description of the number of displacements ($\nu(T)$) that will be generated by a PKA with energy T. Figure 2.3 schematically illustrates $\nu(T)$.

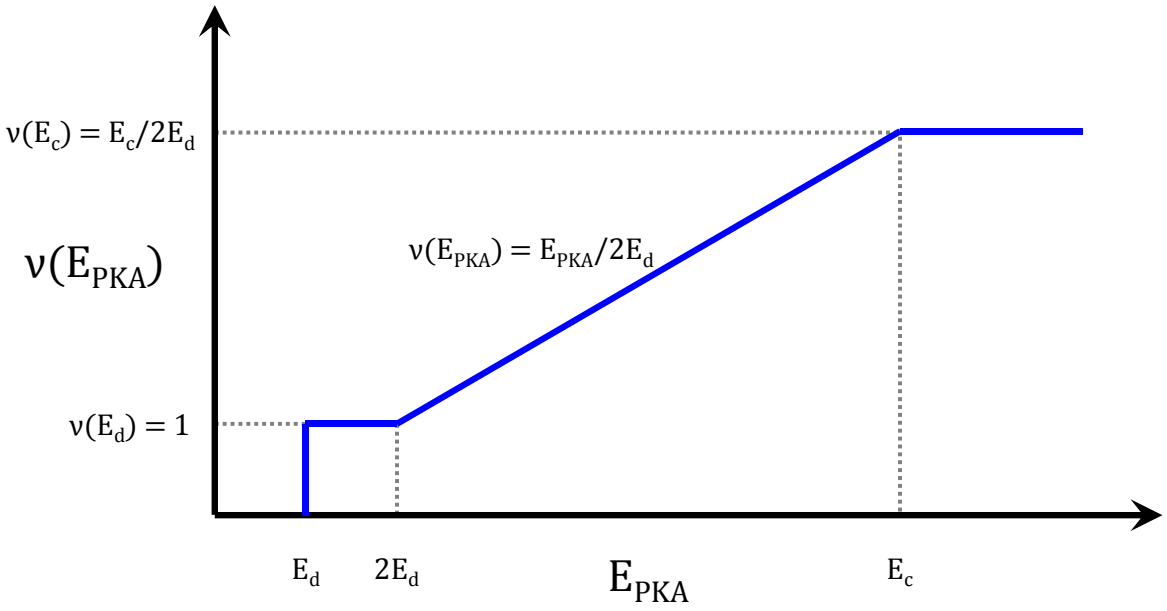

Figure 2.3 Schematic illustration of the number of displacements generated as a function of E_{PKA}.

The KP model also describes a limit to the value of ν. When an atom at high energy (~MeV) strikes a solid, the orbital electrons are stripped off, and the resulting ion transfers its energy to the surrounding material through the Coulomb interaction. The threshold energy for such an interaction is called the Coulomb energy (E_c). The KP model assumes that when $T>E_c$, no additional displacements will occur, since energy dissipated through electronic stopping will not generate any atomic displacements. Therefore, in the energy range where ν varies with T, $\nu(T)$ is given by:

$$\nu(T) = \frac{T}{E_d}$$

The KP model is based on a number of additional assumptions. Already implicitly assumed in the derivations above, only 2-body, elastic collisions are considered, using the hard-sphere particle model. Further, atomic displacements only occur when the T exceeds E_d.

Beyond these, the KP model also assumes negligible energy consumption in the displacement of an atom, no point defect annihilation occurs, and that the arrangement of atoms in a medium is random and isotropic (e.g. the KP model does not account for changes to the atomic density along different crystallographic orientations).

Residual point defects

While the impact of a sufficiently high energy particle on a lattice atom will generate a displacement cascade, the Frenkel pairs that are generated in the cascade are extremely localized. As can be seen from Figure 2.4, quickly following the initial PKA being displaced, the majority of the Frenkel pairs annihilate. However, it is the point defects that do not recombine in that initial cascade that are, in large part, responsible for subsequent and lasting radiation damage in materials [17] [18].

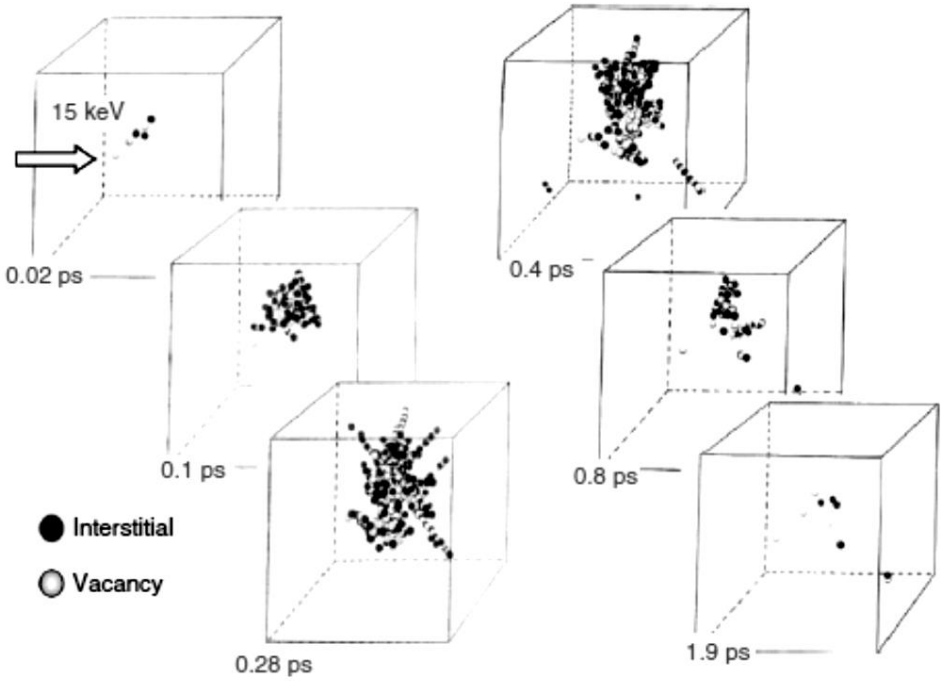

Figure 2.4 Simulated time evolution of a displacement cascade in iron of a 15 keV iron atom. Reproduced from *[17]*.

2.2 Consequences of radiation damage

Increased kinetics

Displacement cascades substantially increase the mobility of atoms in the solid. Fast mixing of atoms in the immediate vicinity of the displacement cascade occurs during the creation and subsequent recombination of Frenkel pairs created by each atom displacement. In addition, a number of point defects will survive the initial recombination

creating an excess point defect concentration of both vacancies and interstitials. Thermodynamic processes that are diffusion-limited will be accelerated due to the increased mobility in the material. As a result, unexpected phase transformations have been known to occur in materials exposed to radiation. Under normal circumstance, the mobility offered by the thermal agitation of the atoms would not be sufficient for observation of the phase change in laboratory time-scales.

If a material is held at temperature for a sufficient period of time, a steady-state vacancy concentration will be reached. In a similar manner, exposure to a radiation field for a sufficient period of time will result in a steady-state point defect concentration. At low temperatures, the point defect population is dominated by the radiation induced point defect, and is in excess of the equilibrium vacancy concentration. However, as the temperature is increased, given the same flux, particle species and energy spectrum, the equilibrium vacancy concentration will exceed the defect population introduced by irradiation. When this occurs, the material will heal out any damage induced by radiation, as the atomic mobility due to the elevated temperature allows rapid reorganization of the phase to accommodate the atoms displaced by a displacement cascade. At sufficiently high temperatures, radiation induced point defects will no longer play a role in determining the kinetic pathways of the system.

Creep

One of the principal challenges in engineering high-temperature materials is the creep phenomenon [19]. Creep is a type of plastic deformation that occurs over an extended period of time to a material that is exposed to elevated temperature and stress. Predominately governed by diffusion, every mode of creep requires mobility of point defects which enable mass transfer from one area to another.

There are several modes in which creep can occur. A stress-temperature map of creep deformation mechanisms is given in Figure 2.5. The first, which takes place at the relatively high stresses and relatively low temperatures, is dislocation climb. While the topic of dislocations can quickly become quite cumbersome, for the purposes of discussion of creep mechanisms, a dislocation can be thought of as an extra plane of atoms extending partway through the crystal. This type of dislocation is known as an edge dislocation. The atomic configuration of an edge dislocation is depicted in Figure 2.6. Using edge dislocations as a general model of dislocations, plastic deformation of a crystal can be achieved by shifting this extra plane of atoms one lattice spacing across the crystal plane. As dictated by their crystalline geometries, dislocations can only move along particular atomic planes. The planes along which dislocations can propagate are known as glide planes. If the glide plane of the dislocation is blocked by another dislocation, a precipitate, or some other disruption of the crystalline uniformity, it must either loop around the obstacle, or cut through it in order to continue to gliding. Since dislocations are effectively a plane of interstitial defects, the termination line of that plane, or dislocation line, can be moved up or down by absorbing or emitting a point defect. A dislocation can “climb” up or down in its glide plane. The “climb” of an edge dislocation by the absorption of a vacancy is shown schematically in Figure 2.7.

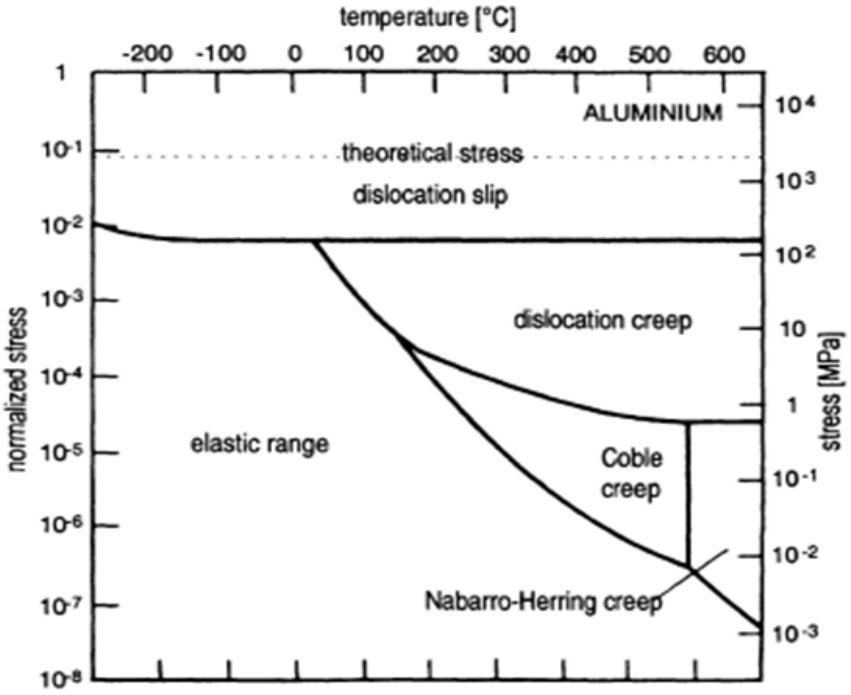

Figure 2.5 Deformation mechanism map of aluminum. Reproduced from *[19]*.

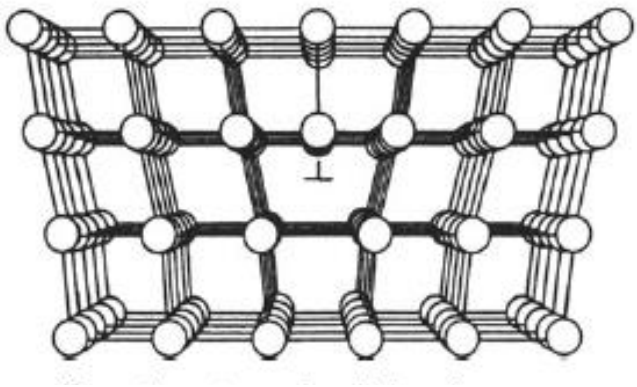

Figure 2.6 Schematic illustration of atomic configuration around an edge dislocation. Reproduced from *[19]*.

If enough point defects are absorbed, the dislocation can move up or down glide planes until it is able to glide past the obstacle. Outside of radiation fields, this only occurs at temperatures above about a third of the materials melting temperature. Under irradiation, the excess point defects can contribute to the onset of dislocation climb at lower temperatures than what would be observed otherwise.

The second creep mechanism is called Coble creep [20]. Coble creep occurs at relatively moderate temperatures and stresses, as can be seen in Figure 2.5. In Coble creep, the deformation mechanism does not involve gliding dislocations, rather the deformation proceeds by atoms diffusing along the grain boundaries, allowing conservation of volume, but eliciting shape change. Like dislocation climb, Coble creep is a diffusional process and

is therefore controlled by the number of point defects available in the material, and their mobility. Typically, Coble creep is observed when materials are held under stress at about half of the melting point. Again, like dislocation climb, when materials are exposed to radiation, the excess point defects that are produced can lead to observation of Coble creep at lower temperatures.

The third creep mechanism is known as Nabarro-Herring (NH) creep [21] [22]. NH creep begins to occur at high temperatures, around three-quarters of the melting temperature and under very little stress. In NH creep, atoms diffuse across the grain bulk in order to transfer the material to accommodate deformation. Excess point defects induced by radiation can contribute to the observation of this form of creep. However, the onset of NH creep typically takes place at such a high temperature that the equilibrium vacancy concentration exceeds that which is induced by irradiation, leading to kinetic behaviors which are dominated by temperature rather than radiation.

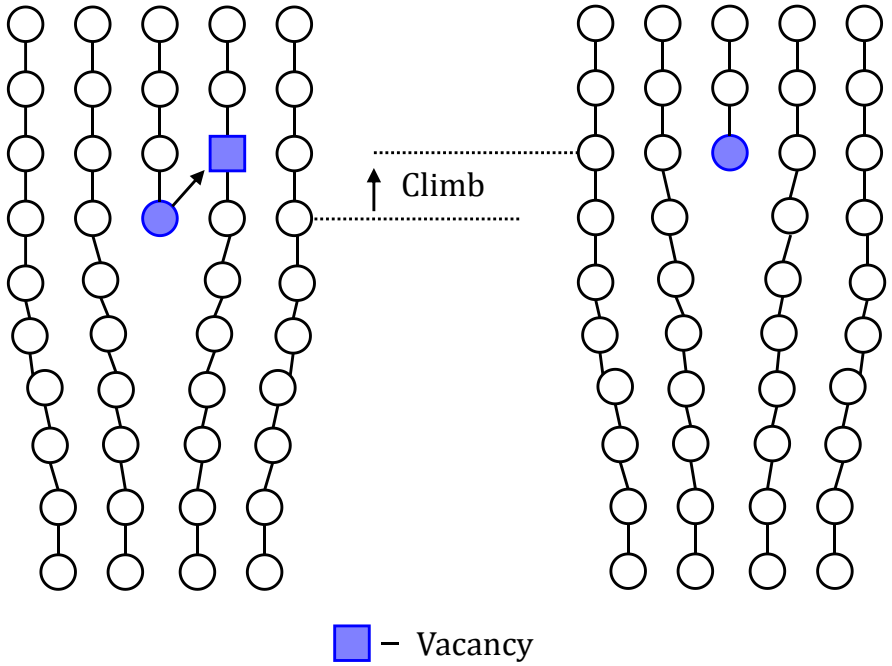

Figure 2.7 Schematic illustration of dislocation climb by the absorption of a vacancy. Of course, many such absorptions must occur to move the entire dislocation line.

Swelling

One consequence of irradiation that is not observed in other scenarios is termed swelling [23]. In fact, swelling was only discovered after examination of fuel and structural materials that had been irradiated in a fast reactor for long periods of time [24].

The mechanism behind these macroscopic changes was first pointed out by Cawthorne and Fulton using TEM. Swelling is the volumetric increase of a material and the coupled reduction of the density [25]. In the initial displacement cascade, interstitials and vacancies are created in equal numbers, and an equal number of them recombine quickly

after formation. However, interstitials are able to travel through the crystal lattice more rapidly than vacancies as the energy barrier for movement of an interstitial is lower than that for a vacancy. In addition to higher interstitial mobility, dislocations have a larger capture radius for interstitials than vacancies; this is due to the larger stress field that an interstitial imposes on the surrounding crystal. The interaction of the interstitial stress field with the dislocation stress field is, therefore, more probable than that of the smaller vacancy stress field. For these two reasons, the excess interstitials are quickly absorbed by dislocations, leaving behind an excess of vacancies.

Swelling exhibits temperature dependence. The dependence is based on the relative rates for the mobility of vacancies and interstitials, the concentrations of both, as well as the bias for absorption/emission from point defect sinks. When the temperature is too low, swelling is inhibited, as the point defects do not have sufficient mobility to coalesce into voids. If the temperature is too high, then the high mobility of point defects allows them to be consumed by point defect sinks at a rate exceeding that of void production. In the moderate temperature range, approximately 400 – 700 °C for 316 stainless steel, void swelling is able to occur, as the point defects have sufficient mobility to cluster, but insufficient mobility to reach absorption sites [26]. Within the moderate temperature range, the degree of swelling will be governed by the point defect concentrations, which were developed through point defect balance equations, evaluating the strength of each source and sink for each type of defect at a given temperature [27] [28] [29].

Like any solute, when the concentration exceeds the thermodynamic equilibrium concentration, the solute will experience a driving force to precipitate. While vacancies differ from typical solute atoms in that they will be annihilated by interacting with an interstitial, they still experience a driving force to precipitate. First, vacancy clusters form. If those clusters achieve a critical radius, where the energy removed from the system by the formation of a cluster exceeds the surface energy that is added to the system by its formation, the clusters will be stable. The stable vacancy clusters will continue to absorb vacancies and grow into voids. By absorbing more vacancies, these voids expand the materials dimensions and reduce its density, increasing the component's size.

Embrittlement

Another of the major consequences of material irradiation is embrittlement. Embrittlement is a bit of a broad term in this case, as it covers several distinct mechanisms through which a material can become more brittle as a result of radiation damage. The term embrittlement is the material's inability to deform plastically without fracture. Embrittling is associated with a hardening of the material, an increase in yield strength as well as a reduction in ductility, fracture toughness and total and uniform elongation. The mechanistic reasoning behind embrittlement is typically an increase in the number and/or strength of the obstacles to dislocation motion. For example, cold working embrittles a material because the forced material deformation results in a large number of dislocations being generated in the grain. Since dislocations are themselves a disruption of the crystal lattice, they impede each other's motion. The dislocations tangle up and are unable to glide further. Since the dislocations are unable to glide, the material is unable to deform under stress and it will crack.

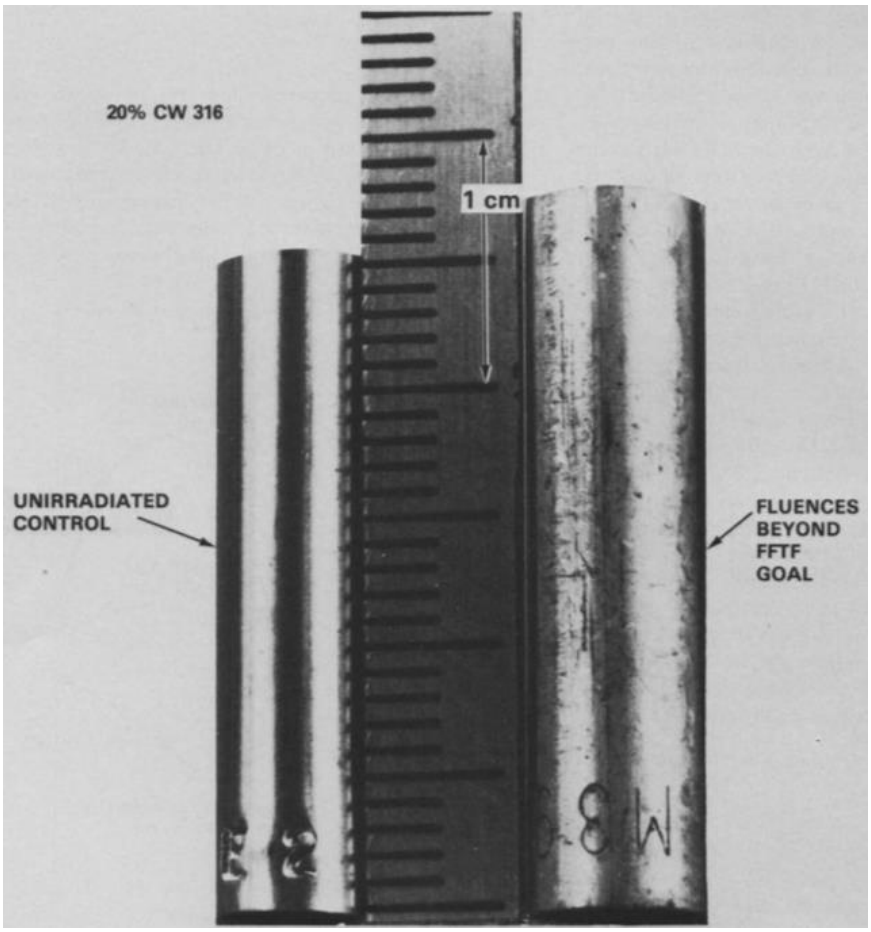

Figure 2.8 This image, reproduced from *[24]*, demonstrates the severity of the problems that swelling can create. The alloy featured here is 20% cold-worked AISI 316. After reaching a dose of ~75 dpa, the material is nearly 10% longer than the control.

Although high dislocation densities can clearly embrittle a material, any obstacle to dislocation motion can cause this to happen. Under irradiation, a number of such obstacles can be developed. The interstitials, vacancies and helium produced under irradiation all provide point defects in the lattice which impede dislocation motion. While solid solution hardening may not be the only factor in embrittlement, it certainly contributes to the overall effects taking place.

Vacancy clusters, if they have not yet formed voids, often collapse into dislocation loops, which also act as barriers to dislocation motion. In this case, the type of dislocation loop would be a vacancy loop, although if the interstitial concentration exceeds the equilibrium concentration then the formation of interstitial loops is also possible. Any voids that are formed during swelling, or any precipitates that form under irradiation also act as barriers to dislocation motion. These types of barriers tend to be very strong and contribute to the majority of the hardening akin to precipitation hardening observed in metals. Any and all such barriers can cause embrittlement of different degrees of a material under irradiation.

Helium embrittlement is of particular concern in materials expose to high energy neutron fluxes [30]. As mentioned earlier, (n, α) reactions release helium into the matrix. The

helium atoms are only soluble in low concentrations, and can act as barriers to dislocation motion. In addition, helium can diffuse into small vacancy clusters. The presence of the helium in the vacancy clusters acts to stabilize them, which results in a higher density of voids in the material.

Changes to grain boundaries can also cause changes to the mechanical properties of the material. Helium tends to migrate to the grain boundary, which is believed to weaken the bonds between the grains, and therefore weakening the material overall. In addition, precipitates that exist on the grain boundary can be broken up, and their constituent atoms redistributed along the boundary. This redistribution of solutes also weakens the grain boundary. Other solutes are also known to build up on the grain boundaries and the increased kinetics offered by the radiation field increases the potential for formation of brittle phases at this interface. This is known as grain boundary embrittlement.

2.3 Material design for radiation tolerance

Introduction

Material design for radiation tolerance is characterized by four possible phenomena. 1) reduce the interaction of a material with radiation in order to reduce the number of cascades (e.g. using materials with low interaction cross-section) 2) use materials which foster more instantaneous annihilation (high and equal mobility of vacancies and interstitials) 3) use materials for which additional defects do not add to already pre-existing microstructure (e.g. amorphous materials, liquids, etc.) 4) use materials which provide trapping sites for unavoidable defects, therefore removing them from the matrix. Another possible approach would be to modify the irradiation conditions. For example, if the irradiations were carried at a sufficiently high temperature, the equilibrium point defect population would be comparable to the population induced by irradiation. In this case, the damage induce by irradiation would be healed out immediately by the thermally available vacancies. In most cases however, the conditions of the irradiation are inflexible, defined by reactor design, rather than material design, and furthermore, at elevated temperature other material properties (e.g. tensile strength, creep rate, etc.) are severely degraded. Approach 1) is not practical for structural material design, as the interaction cross-section is tied with the elemental (or isotopic, more precisely) identity of the material. Since there are relatively few available structural materials composed of different bulk elements, selection of material by cross-section is not generally feasible. For example, if iron had an unfavorable cross-section, then all steels would be removed from the material candidate pool. Approach 2) is also not practical, in that it is not clear that a material exists that could provide extremely fast annihilation pathways for the point defects generated in the prompt cascade. In most structural materials considered for nuclear applications, approaches 3 and 4 seem the most practical. These approaches can accommodate more conventional structural materials, and focus on the extraction of point defects that are not healed out immediately following the displacement cascade. The strategy to develop radiation tolerant materials is to not necessarily prevent the initial

radiation interaction (although there are a few strategies that use this idea) but to prevent the buildup of point defects that enhance the kinetics of the material system, leading to creep, swelling, embrittlement and the precipitations of undesired or unexpected phases. By preventing the buildup of defects and the mitigation of the result of those defects, mechanical property changes can be reduced or avoided entirely.

Low interaction cross-section

One strategy to provide radiation tolerance is to reduce the probability for the material to interaction with the radiation. Elements which have an extremely low cross-section will have fewer displacement cascades, because fewer PKAs will be generated in a given irradiation time. However, from the standpoint of structural materials design, this approach can be impractical as it severely limits the pool from which alloying elements can be drawn. This, in turn, limits the types of environments that material can be exposed to, i.e. high temperatures, corrosive environments, high stresses, cyclic stress states. Furthermore, drawing on a limiting alloying element pool can also have consequences in the machinability and weldability of the alloy.

Amorphous materials

Another possible route to mitigating radiation damage might be to utilize amorphous materials (materials without long-range atomic order). Since these materials do not derive their mechanical properties from a particular crystal structure, disruptions of their atomic ordering should have little to no effect on their mechanical properties. However, generally, amorphous structural materials will have limited potential applications.

Point-defect annihilation sites

One of the most promising strategies for radiation tolerant material design is point-defect annihilation sites. This strategy acknowledges that prompt defects, triggered by the incident radiation and displacement cascade, cannot be avoided through material design easily. This is especially true if the elements and class of material is selected. Rather, this strategy focuses on the continued removal of the defects which survive annihilation in the initial cascade. It is these defects which induce microstructural evolution, so by removing them, the microstructural integrity can be maintained. There are a number of microstructural features that can provide point defect recombination. For instance, dislocations, precipitate interfaces and grain boundaries are all common structures which allow point defects to be trapped and further removed from the system [31] [32]. Removal of the excess point defects reduces the kinetic pathways a material has to creep, or precipitate, or otherwise change properties.

While grain boundaries can also act as recombination sites, in many cases the site density offered by grain boundaries is too low to provide substantial radiation tolerance. Recombination sites can be handily introduced into a material through cold working. During cold working, large numbers of entangled dislocations are generated in the crystal bulk, which impede each other's motion and as a result, reduce the material's ductility. Cold-working is able to provide alloys with moderate radiation tolerance and is employed in some modern LWR cladding [33]. While cold-working can provide some degree of

radiation tolerance, at elevated temperatures, dislocations migrate and annihilate, greatly diminishing the radiation tolerance available at lower temperatures.

Dominating the efficacy of the point defect absorption strategy is the number density and defect sink strength of the recombination sites. As the dislocation density of an alloy is increased, this generally leads to an undesirable (and quite significant) reduction in toughness. Another possible strategy is to mix large interstitial atoms into the metal matrix, these atoms can be finely dispersed at extremely high densities, and can be chosen such that they will not precipitate out at elevated temperature. However, these large interstitial atoms do migrate at elevated temperatures and tend to build up in the grain boundaries after being held for long periods of time at high temperature. Therefore using large interstitial alloying elements is also not viable.

However, the introduction of small precipitates into a metal matrix can provide an extremely high number density of recombination sites. Moreover, careful selection of a thermally stable phase can yield precipitate interfaces that do not migrate or change character over a broad range of temperatures.

Helium capture sites

The same interfaces that enable point defect recombination often can provide helium storage capacity to reduce the concentration in the matrix. While grain boundaries have been found to embrittle materials as they become saturated with Helium, precipitate interfaces are thought to perform similarly in their function of enabling point defect recombination regardless of the presence of helium. So, introducing high number densities of small precipitates not only can provide radiation tolerance, but offers a simultaneous solution for helium embrittlement.

2.4 Oxide-dispersion strengthened (ODS) steels

Introduction

To understand the origin and development of ODS alloys, it is important to recognize that ODS alloys are a subset dispersion-strengthened (DS) alloys, and that the term ODS has been used to refer to a very specific class of composite materials. DS alloys have been used and developed for centuries. Archeological evidence suggests that even prehistoric humans made use of silica dispersions in copper to harden tools and weapons [34]. Thoria-bearing tungsten (ductile tungsten) was the first commercially available DS metal. Developed by scientists at General Electric, it was used for filaments in incandescent lamps [35]. Following the development of an internal oxidation process to grow oxides in copper [36], Irmann discovered that by sintering aluminum powder, the resulting bar had an increase in strength of an order of magnitude over conventionally produced aluminum at 300 °C [37] [38]. This result, coupled with growing technical problems in the production of gas-turbines, drove efforts to explore similar responses in other metallic systems.

It is important to note at this point, that DS and precipitate-strengthened do not mean the same thing. Precipitate strengthening often relies on heat-treatments to produce the precipitates in the matrix, leading to the desirable properties by carefully manipulating chemistry and temperature profiles. Since the precipitates formed in the matrix originate from a saturated solution the precipitates can return into the solution under the right conditions (temperature). DS materials differ, in that once the dispersion has been formed, it is relatively insensitive to changes in temperature. As such, the prospect of DS materials became quite interesting as they could withstand much higher temperatures than other alloys. Throughout the late 1950's to the mid 1960's, a considerable research effort has been put into understanding how DS alloys can be made, which systems they can be applied to, how to produce the materials as well as theories concerning their creep properties and dispersion strengthening [39] [40] [41] [42] [43].

The insensitivity to temperature caught the attention of many scientists, as many of the previously studied materials, such as aluminum and copper, had relatively low melting points. Du Pont and Sherrett Gordon both developed a DS nickel alloy boasting strengths an order of magnitude higher than other nickel alloys at high temperature. Following the flurry of commercial development of DS alloys, NASA, as well as a few universities, private laboratories and industry continued to research DS materials [44]. Mainly, the challenges were to explain how adding such a small quantity of dispersoids yielded such tremendous improvements in creep strength, understanding how to add reactive elements, to create superalloys strengthened by both precipitation and dispersion, and to develop joining methods.

New methods of preparing the constituent powders were developed in the 1970's. Beginning with the use of stirred attrition milling developed at NASA, Benjamin developed the mechanical alloying process while at International Nickel [32]. Mechanical alloying consisted of smashing dry, elemental powders together in a controlled atmosphere. An attrition mill is used to input energy into the powder through milling media, to weld, compress, fracture and reweld powders together. This process was attractive as it could be used to prepare any metal and stable oxide, and guards against contamination that previous chemical and wet milling processes could not. The majority of DS material today is manufactured using this process.

High temperature structural applications are the main uses for DS alloys. Turbine blades, rocket nozzles, and other such parts are the main engineering motivation for the development of such materials.

Ferritic ODS steels

The specific class of DS alloys that are being considered for fast reactor cladding materials are ferritic ODS steels. The unique high temperature strength and creep resistance attributed to ODS alloys are due, in part, to high number densities of oxide particles located both within the grain bulk and along grain boundaries, shown in an overview image obtained with a scanning transmission electron microscope (STEM) in Figure 2.9a). Figure 2.9b) is an image of a single oxide precipitate obtained using bright-field high-resolution transmission electron microscopy (BF-HRTEM) [45].

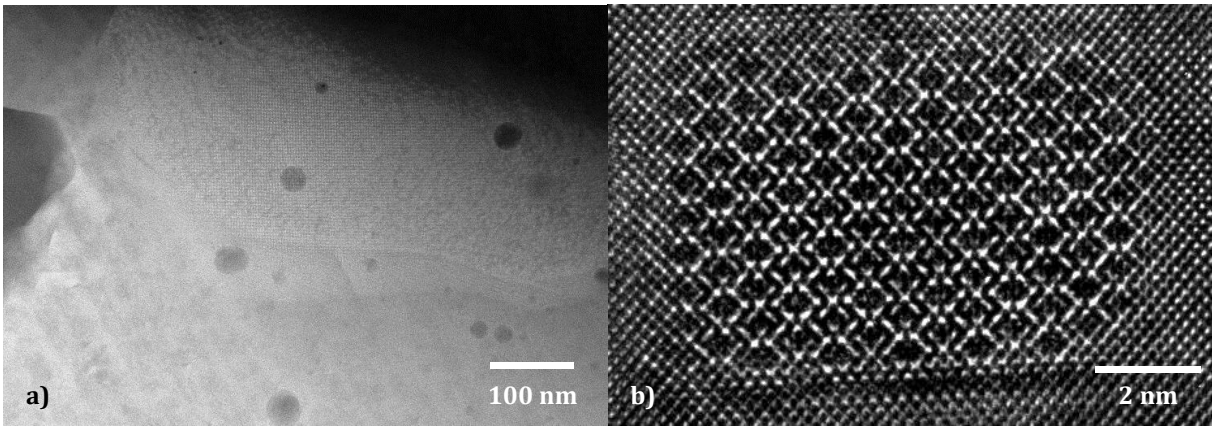

Figure 2.9 a) Overview STEM micrograph of ODS alloy. b) BF-HRTEM micrograph of ~8 nm oxide particle [45].

The oxide precipitates serve several functions in the ODS alloy. First, they provide obstacles to dislocation motion, which enhances the ODS alloys resistance to creep. In addition, the oxide particles pin grain boundaries, preventing grain growth and recrystallization allowing it to maintain ultrafine grained structure even at high temperatures. The impeded dislocation motion and resistance to grain growth provide ODS alloys their high temperature strength. The high number density of oxide precipitates is thought to offer notable radiation tolerance as it provides extremely high surface area of point-defect recombination sites [46] [47] [48] [49].

Ferritic ODS alloys are also more swelling resistant than austenitic steels. This is due to the body-centered cubic (BCC) crystal structure that is characteristic of ferritic steels. The reason that BCC materials are more radiation tolerant than austenitic (FCC) materials is that the dislocation bias for point defects is smaller in BCC materials. In FCC materials, the remnant point defects tend to agglomerate into several large clusters of vacancies. In BCC materials, the excess point defects are more evenly distributed, in a diffuse cloud of single defects or perhaps in pairs, which greatly improves the probability of encountering a recombination site or interstitial, rather than forming voids. This superior defect distribution in ferritic materials is what provides some of the radiation tolerance, and resistance to swelling.

On the other hand, ferritic alloys, in general, have inferior creep properties to austenitic steels. Use of ferritic ODS alloys solves this problem by way of the oxide particles. Not only do the oxide particles block dislocation motion and contribute to the materials strength, but one of the modes of creep relies on dislocation climb. In ODS steels, the oxides are present in such a fine distribution, at such high density, that even if a dislocation managed to climb over one obstacle, it will only be able to glide several nanometers before encountering another obstacle. Therefore, ferritic ODS steels offer not only resistance to radiation damage and swelling, but also creep resistance in the dislocation climb regime of approximately one third to half of the melting temperature.

In addition, the oxide particles pin grain boundaries. At high temperatures, through diffusion, driven by the reduction of grain boundary surface area, large grains grow at the expense of small grains. However, the oxide particles along the grain boundaries provide an energetic barrier to the movement of the boundary. Since moving the grain boundary off the oxides would require input of energy into the system that exceeds the surface energy of the oxides that would be left behind in the bulk crystal. As the driving force for grain boundary motion cannot exceed this barrier, the gain boundaries do not move, and thus normal grain growth does not occur. Abnormal grain growth, or secondary recrystallization is also limited in ODS steels. Typically secondary recrystallization occurs when precipitates that are pinning dislocations are near their solvus temperature. When this happens, statistically, several of the precipitates will dissolve first. Once the grain boundaries those precipitates pinned are able to move, they quickly consume the grains around them, creating extremely inhomogeneous grain structures. However, the oxide particles melting point is substantially higher than the melting point of the ODS alloy, therefore, the conditions for secondary recrystallization cannot be met.

ODS alloys also exhibit a sub-micron grain diameter, with elongated, columnar grain structure depending on the detailed processing parameters. Although this structure is not necessarily inherent to ODS alloys, in order for an alloy to be shaped into a useful part, a certain and sometimes substantial amount of forging, rolling and extrusion must occur. ODS alloys, while maintaining attractive properties at high temperature, are brittle at lower temperatures. Thus, in order to shape them, many rolling/forging passes are required to achieve the final part form. High numbers of rolling steps result in texturing (the relative alignment of the crystal structures of adjacent grains) and grain elongation. This is taken to an extreme in ODS alloys, as during the post-rolling anneal, recrystallization is not taking place due to the oxide particles. Columnar grain aspect ratios can reach as high as 50, (200 nm diameter by 10 μm in length). The extreme anisotropy of the grain structure as well as the texturing of the grains give ODS alloys different mechanical responses, depending on the orientation of the stress with respect to the rolling direction.

Ferritic ODS alloy selection

A number of ferritic ODS steels are commercially available for testing irradiation response. In this study, MA957 will be used as an example of an archetypical ferritic ODS steel. Extensive studies have been conducted on the mechanical properties, creep resistance, corrosion resistance, thermo-mechanical properties and microstructural features, making it an ideal candidate for radiation studies, as it is a well understood material in the unirradiated condition [50] [51] [52] [53] [54]. Although MA957 has been studied for its thermomechanical properties in great detail, few studies on the effects of high dose neutron irradiation (>100 dpa) near target operating temperatures have been conducted, making these materials of high value for understanding neutron radiation effects on ferritic ODS alloys.

MA957 demonstrates all of the attractive characteristics of a ferritic ODS steel. It has an ultrafine distribution of oxide particles with a very high number density. It has sub-micron grain size, which substantially contributes to its high strength. Like other ODS alloys, the

oxide particles in MA957 are thermally stable up to ~1000 °C, resisting even coarsening, much less melting.

ODS alloys are notoriously known for microstructural inhomogeneity as a result of the mechanical alloying manufacturing process [55]. Therefore, it is important to track the exact heat in which the material of interest is produced to keep sample to sample variation to a minimum. Unlike conventionally prepared alloys, two ODS steels with the same composition may have very different properties depending on the mechanical alloying parameters as well as the conditions of the consolidation process. In this work, conclusions about the effect neutron irradiation to extremely high dose will be drawn from two heats: DBB0111 and DBB0122, prepared by an industrial alloy manufacturer, International Nickel (Inco).

2.5 Post irradiation mechanical property insights

Irradiation experiment

In order to validate the performance of MA957 under neutron irradiation to high doses, long term performance studies are required. Irradiation tests were conducted at the Fast Flux Test Facility (FFTF) in Hanford, WA. The specimen geometry was creep tubes. The samples have been irradiated from 43 up to 121 dpa making some of them the highest neutron dose ODS samples known to the author.

These irradiation tests were designed to accomplish several goals at once. By using pressurized tubes, the irradiation induced creep properties can be studied, while simultaneously producing a number of mechanical test specimens and samples for high resolution microscopy.

Mechanical properties testing

Collaborating researchers at Pacific Northwest National Laboratory (PNNL) performed micro-tensile tests on the irradiated specimens. Tensile testing is a standard method for assessing the yield strength, ultimate tensile strength, elastic modulus, and total elongation of a material. These metrics are extremely important for materials selection for application in reactors or any engineering use.

Observable from **Error! Reference source not found.**a) specimens irradiated at 550 °C nd higher exhibited normal ductile fracture. However, as can be seen in **Error! Reference source not found.**b), at irradiation temperatures of 412 °C and below, compound brittle fracture was observed. In order to understand the changes in the oxide particles that presumably caused this transition in properties, high resolution microstructural characterization is necessary.

The overall irradiation performance of MA957 will be evaluated based on a battery of mechanical testing, as cladding is a structural material, the expectations of its performance are based on strength, resistance to deformation, and ductility.

2.6 High resolution microscopy

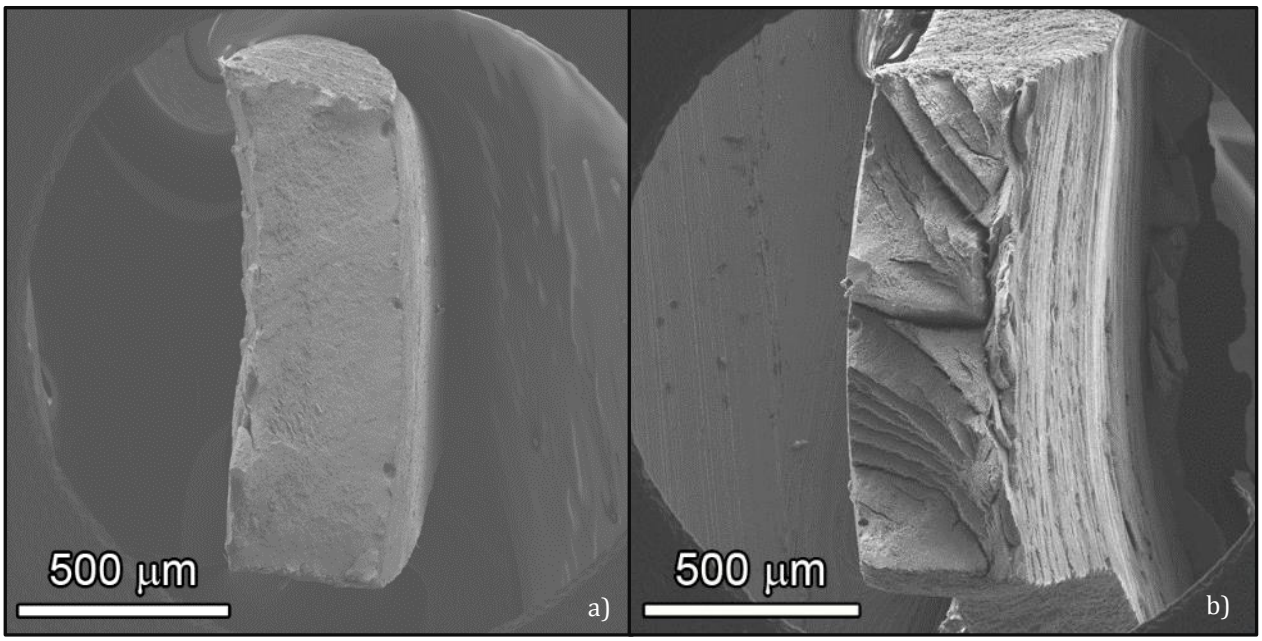

Figure 2.10 a) fracture surface of microtensile specimen irradiated at 550 °C b) fracture surface of microtensile specimen irradiated at 412 °C *[66]*.

Oxide particle properties

In order to understand the changes in mechanical properties as a function of irradiation condition, the microstructure must be evaluated, as its properties control the desired mechanical properties of MA957. In other words, it allows understanding of the "why" of a property change. Insight into the microstructure of ODS materials requires high resolution microscopy.

The goals of the microscopy are to investigate the oxide particle property change, in terms of number density, size, distribution and composition. Further, the microscopy study will investigate the grain boundary properties, such as solute enrichment and assessment of the oxide particles which pin the grain boundary. Finally, the microscopy will investigate the development of any secondary phases, additional oxides, intermetallics, or any other phases.

Due to the small size of the oxide particles, a limited number of experimental techniques are available. The most widely accepted technique for analyzing such small structures is high-resolution transmission electron microscopy (HRTEM). However, concurrent work

by the author, as well as other researchers, has shown that quantitative analysis of these features within the metal matrix using HRTEM is quite difficult [56] [57] [58] [59] [60]. Small-angle neutron scattering (SANS) is another technique capable of measuring the desired properties of the oxides. However, SANS is a bulk sampling technique, so it is not able to distinguish between individual particles. Furthermore, SANS requires significant interpretation and experimental assumptions to understand the output data since it is a spectroscopy based method.

Another technique which has been put to considerable use to investigate ODS alloy microstructure is atom probe tomography (APT) [61] [62] [63] [64] [65] [66]. Although significant data interpretation is necessary to draw conclusions from APT measurements, its element-specific high resolution and ability to render the atomistic data in three dimensions makes it an ideal candidate for investigating MA957 (and other ODS alloys) on a local scale.

APT provides the clearest insight into relative changes in the oxide particle properties (including number density, size and relative composition) as a function of irradiation condition. APT can evaluate changes to oxide particles themselves, in terms of size, distribution, and composition. It can evaluate changes to grain boundaries, as a change to the character of the grain boundaries could manifest in similar mechanical property change. It is also able to investigate the possibility of secondary phase formation, which could also cause or contribute to mechanical property change.

The post-irradiation condition of oxide particles was investigated using APT measurements. The data analysis section of this manuscript will consider cluster analysis parameter selection, allowing comment on oxide particle density, size and chemistry. The discussion will also include investigation of grain boundary properties and comment on the presence of secondary phases.

3 Experiment

3.1 Irradiation conditions

Experimental program description

As part of ongoing experiments in support of the Liquid Metal Fast Breeder Reactor (LMFBR) program that ended in the 1980's, commercially produced MA957 underwent a comprehensive irradiation series in the Fast Flux Test Facility – Materials Open Test Assembly (FFTF – MOTA) [31] [67]. Some of these specimens, in the form of in-reactor creep tubes, were recently recovered from long term storage for analysis as part of the DOE-NE Fuel Cycle R&D program. The compositions of the specific MA957 heats investigated in this study are given in Table 3.1**Error! Reference source not found.** [68]. Irradiation conditions for the investigated specimens are presented in Table 3.2 [69].

Table 3.1 Nominal composition of MA957 heats under investigation.

Alloy	Heat	Cr	Ni	Mn	Mo	Si	C	V	W	Ti	Y_2O_3	Fe
MA957	DBB0111	13.8	0.13	0.05	0.31	0.05	0.014	-	-	1.05	0.22	bal.
MA957	DBB0122	14.2	0.10	0.06	0.31	0.03	0.013	-	-	1.03	0.22	bal.

Table 3.2 Irradiation conditions for MA957 specimens under investigation.

Heat	Specimen ID	Dose [dpa]	Irradiation Temperature [°C]	Hoop Stress [MPa]
DBB0122	TX12	43	385	0
DBB0122	TX15	48	495	0
DBB0111	EV46	109	412	60
DBB0111	EV34	113	550	60
DBB0111	EV06	110	670	60

3.2 Sample preparation

Post-retrieval sectioning

The creep tube specimens were sectioned using wire electrical discharge machining (EDM) by collaborating scientists at PNNL. Micro-tensile dog-bone samples were fabricated for mechanical properties evaluation. For high resolution microscopy, several 3 mm TEM disks, and several 1.0 mm x 0.5 mm x 0.5 mm sample coupons were taken from each tube as can be seen in Figure 3.1.

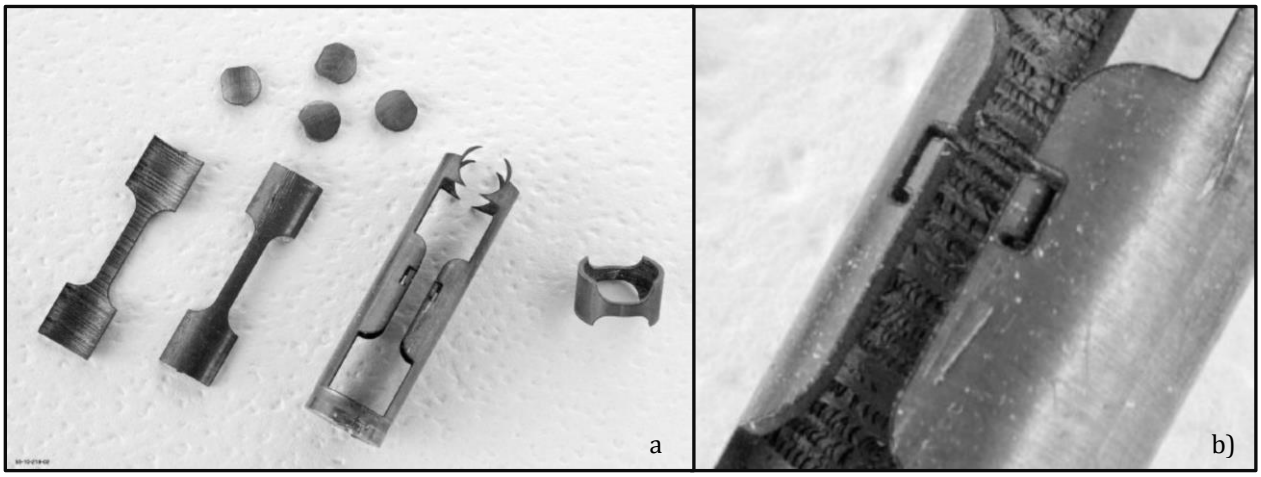

Figure 3.1 a) Microtensile, ring-pull test and high resolution microscopy specimens as prepared by wire-EDM b) High magnification image of APT sample coupons.

Mounting and polishing

The 1.0 mm x 0.5 mm x 0.5 mm sample coupons were shipped to the University of California at Berkeley (UCB) where they were fixed to aluminum SEM stubs with glue and colloidal silver suspension (Figure 3.2a). The small size of the samples allowed minimal handling risk as the active volume was significantly reduced. At the UCB nuclear materials laboratory the specimens were mechanically polished (up to 1200 grit) to remove any surface damage induced by the EDM process.

APT specimen manufacture

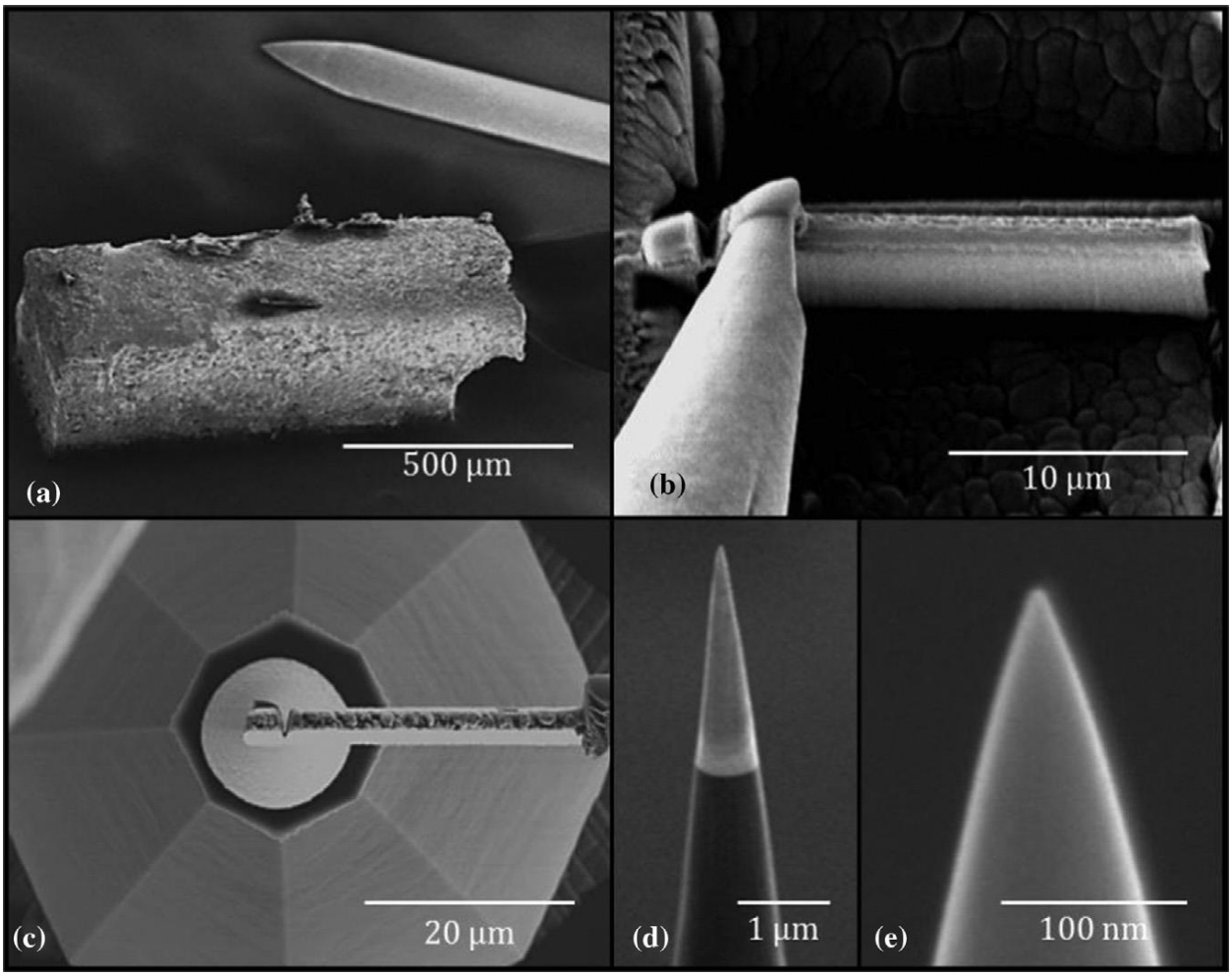

Figure 3.2 a) APT sample coupon, mounted on SEM aluminum stub b) Lift-out technique step one, removing lamella from trench c) Sectioning lamella, and welding to APT Si sample coupon post d) Sharpening of APT tip e) Final cleaning step of APT tip using low energy ions.

APT specimens were manufactured using a standard lift-out technique (Figure 3.2b-d) with a FEI Quanta 3D FEG Focused Ion Beam (FIB) tool, instrumented with a Kleindiek micro-manipulator apparatus and a platinum gas injection system as documented previously [70] [71] [72] [73]. The APT specimens were mounted on Camecas Si needlepads. Gallium damage, known to be induced by the FIB beam during specimen preparation, was largely

removed with a final cleaning step (Figure 3.2e) which utilized low energy (2 keV) gallium ions in order to reduce aberrations in the collected APT data [74]. After preparation, no residual activity was measurable (using standard Geiger counters) on the APT specimens.

3.3 Atom probe tomography

Technique summary

Illustrated schematically in Figure 3.3, atom probe tomography (APT) is a destructive analysis technique in which a high voltage is applied to a sharp specimen tip (radius < 50 nm) with a local electrode. The voltage is then pulsed, initiating field ionization of an atom

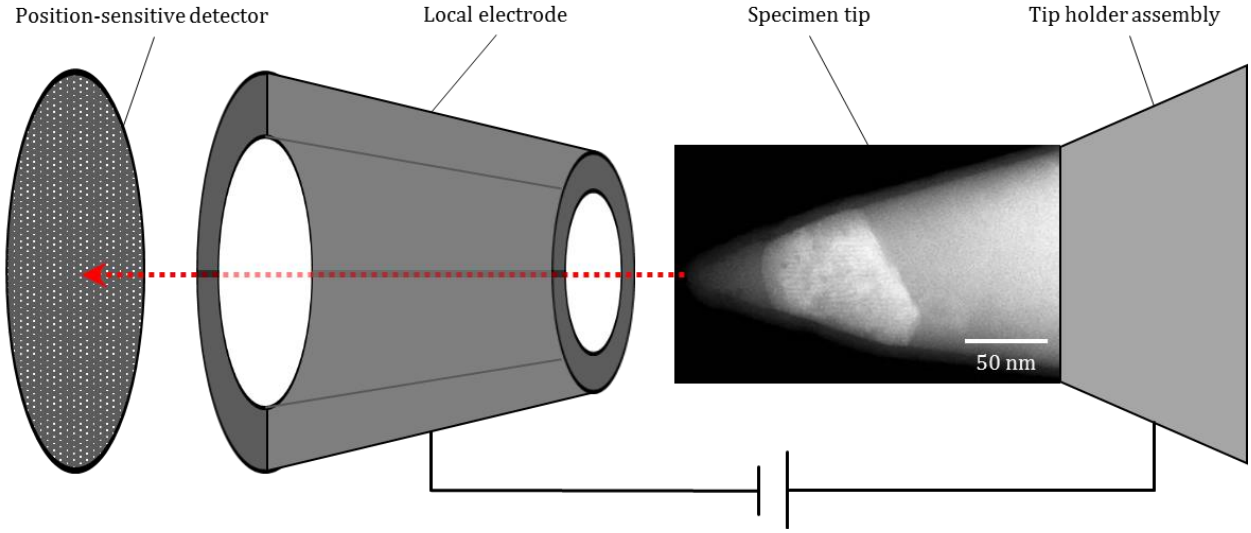

Figure 3.3 Schematic illustration of local electrode atom probe tomography instrument.

at the apex of the tip, which subsequently leaves the tip surface. The ion then accelerates quickly through a hole in the electrode and travels through a time-of-flight mass spectrometer, allowing the identification of its isotopic identity. Finally, the ion strikes a position-sensitive detector. This process is repeated until the tip breaks or data acquisition is stopped. Three dimensional, element-specific data can be acquired from APT. Although the moniker APT implies detection of individual atoms, the hits on the detector actually indicate *ion* strikes, which can be singular or molecular. Several excellent textbooks describe the details of this process at length [75] [76].

Development of APT technique

The history of APT is long and involved, beginning with field-emission electron microscopy (FEEM). Figure 3.4a) shows one of the most promising images obtained via FEEM, which shows clearly the two-fold symmetry of the <110> orientation of a tungsten needle [77]. Spurred on by the promise of FEEM, the imaging technique was further refined, leading to the development of field ion microscopy (FIM). FIM then led to the atom probe field ion microscope (APFIM), then to the imaging atom probe (IAP), then to the position-sensitive atom probe (PoSAP), then to the scanning atom probe (SAP), then finally to the local electrode atom probe (LEAP) which is the basic instrument architecture used in modern atom probe tomography.

APT is the modern progeny of FIM. FIM has been performed for over 70 years and was the first technique with the ability to image individual atoms as illustrated by Figure 3.4b) [78] [79]. FIM images surface structures on a specimen tip by applying a high field to the specimen tip, which ionizes a low-pressure fill gas (such as argon). As a neutral gas particle approaches the charged specimen surface, some of its outer shell electrons are liberated into the tip. The loss of outer electrons results in the ionization of the gas atom. Thereafter, the positively charged gas ion is repelled from the positively charged tip surface, and is accelerated toward a detector plate. By reversing the bias, it was possible to eliminate the fill gas, and evaporate ions from the tip directly. A time of flight mass spectrometer was

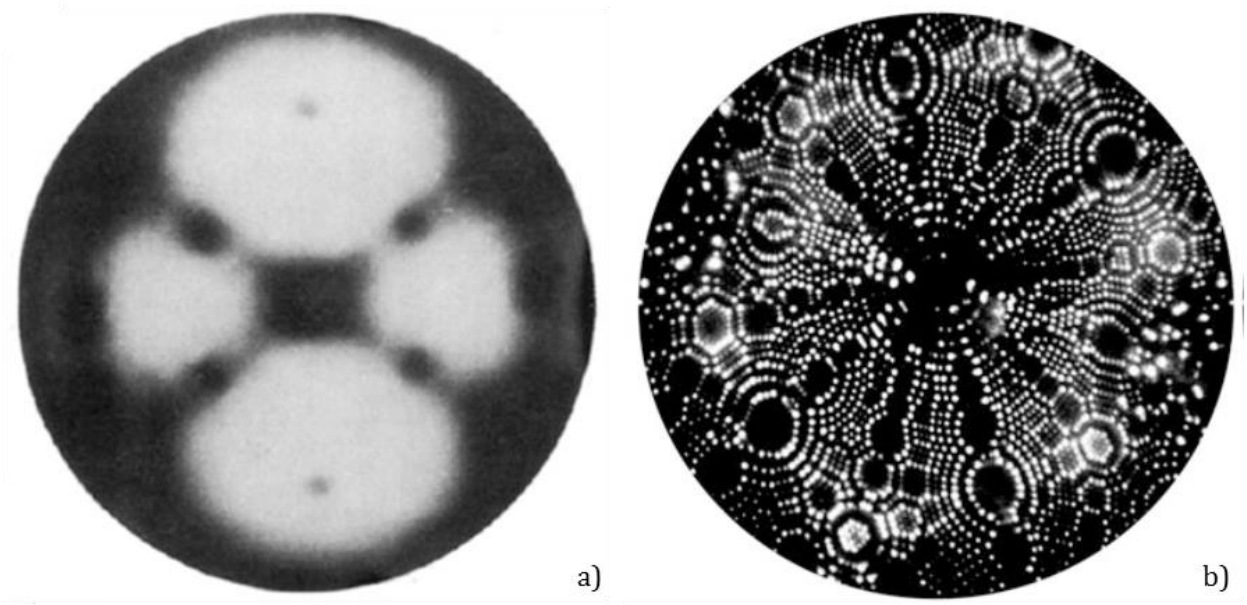

Figure 3.4 a) Image of the <110> orientation of tungsten using a FEEM b) FIM image, the first time atoms had been resolved, circa 1956 *[79]*.

added to the system to allow identification of the ions that were evaporating in addition to their position.

With the addition of micro electrodes, it became possible to investigate samples in rapid succession. This is the defining characteristic of the modern APT instrument the local-electrode atom probe (LEAP). Further advancements have been made. Adding a laser

allowed for field evaporation to be induced in non-conducting materials. Improving the detector has increased the collection efficiency in some recent instruments to as high as ~80% [80].

Theory of field evaporation

All theories of field evaporation are based on the concept that, by some mechanism, an atom sitting on the surface of a specimen is moved sufficiently far from the surface that it breaks its bonds, is subsequently ionized and accelerates away from the surface. While the mechanisms of this process are not fully understood, several models have been developed to provide estimates of the *critical distance*, or the distance at which the atom will become ionized and leave the specimen surface.

The image-hump model is a widely applied model for describing field evaporation, proposed by Müller [79]. In this model, the critical distance can be calculated analytically for materials with well-known electronic properties.

The basis of the image-hump model is the comparison of the atomic and ionic potential energy wells for the atom in question, which are depicted schematically in Figure 3.5. The depth of the atomic potential energy well is given by the sublimation energy of the atom and is denoted E_{sub}. The depth of the ionic potential is summarized as:

$$I_{depth} = \sum_{i=1}^{n} I_i - n\varphi_e$$

Where I_i is the ionization energy of the i^{th} charge state, n is the number of electrons liberated back into the specimen surface, and φ_e is the work function for that material. Therefore the total depth of the well is given by the sum of the sublimation energy and the ionization energy, shown in Figure 3.5b as Q_o.

The electric field (F) changes as a function of distance (x) from the original atom location on the surface, and is given by:

$$F(x) = \frac{-neV_{applied}x}{k}$$

Where n is the number of electrons liberated back into the material, e is the charge of an electron, $V_{applied}$ is the voltage bias applied between the specimen and the electrode, and k is the radius of curvature of the specimen tip. In Figure 3.5, the height of the energy barrier is a function of F, and is denoted by $Q(F)$.

Applying an electric field to the specimen has no effect on the character of the atomic potential energy well, but bends the ionization potential energy curve, therefore lowering the energy barrier between the atomic and the ionic state shortening the critical distance, as is shown in Figure 3.5b [81]. Once the applied field is sufficiently high, the energy barrier for ionization becomes negligible and the critical distance can be surmounted by thermal vibration (Figure 3.5c). Therefore, the critical distance can be related to the specimen temperature.

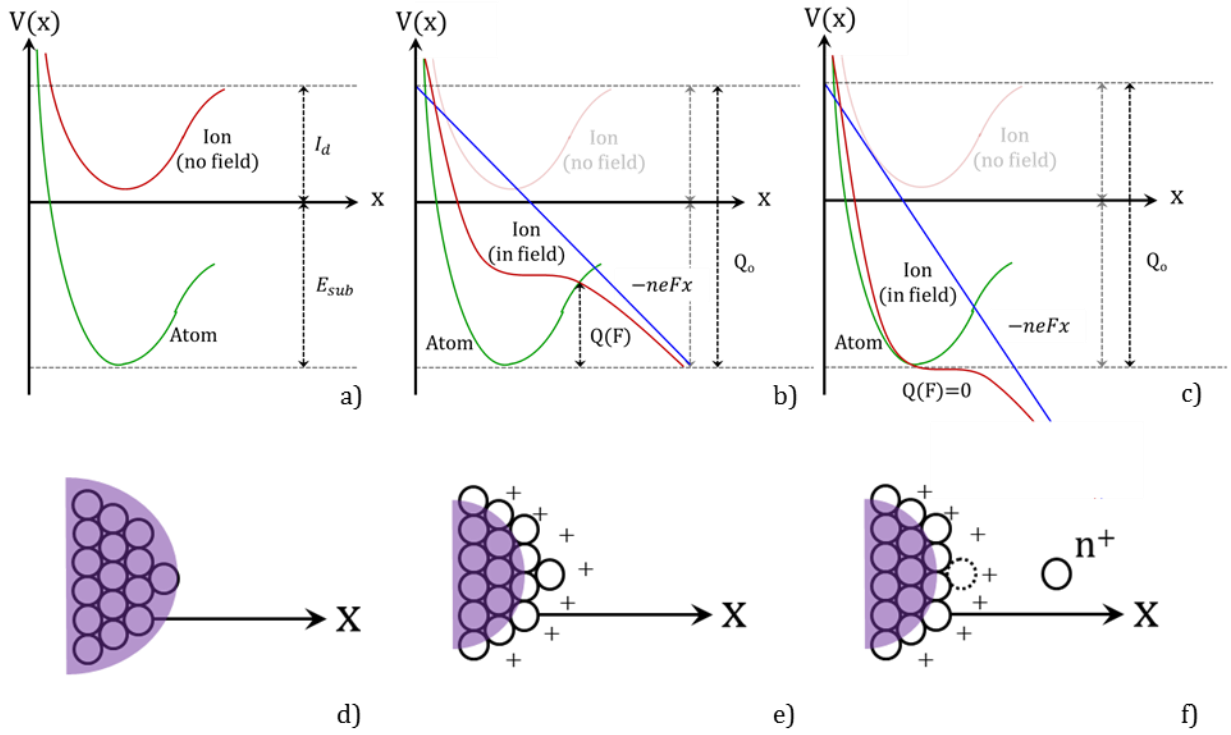

Figure 3.5 a) Ionic (red) and atomic (green) potential energy wells describing the energy involved for an apex atom to leave the specimen surface b) Shape of atomic and ionic energy wells in the presence on an electric field (blue) c) Shape of atomic and ionic energy wells when the electric field reduces the energy barrier to evaporation to zero d) Depiction of metal atoms near the apex of the tip with no applied electric field, the electron gas distribution illustrated in purple e) Depiction of metal atoms and electron gas distribution near the apex of the tip with an applied electric field f) Depiction of metal atoms and electron gas distribution near the apex of the tip once the applied electric is high enough to allow field evaporation.

The image-hump model suggests that by pulsing the voltage applied between the specimen tip and the electrode, field evaporation can be initiated in a controlled manner. The probability for evaporation, in terms of instrument conditions, is controlled by the applied voltage and the specimen temperature. Careful control of instrument parameters can theoretically allow the evaporation of a single atom with each voltage pulse.

However, as with many analytical models, there are problems that point to fundamental misconceptions about the processes that take place during field evaporation. The image-hump model allows for calculation of the critical distance, and the height of the energy barrier that withholds the atom from evaporation. But, when comparing the height of the supposed energy barrier to the expected coulombic repulsion forces present between the charged nuclei at the critical distance, the repulsive forces dominate any other forces that may be present. Therefore the energy barrier to evaporation does not exist at the critical distance.

In many cases, materials investigated using APT do not have well enough defined electronic properties to be able to analytically determine the evaporation voltage, or required specimen temperature. Therefore, the image-hump model is most often used as an intuitive guide, providing a working knowledge of the field evaporation process.

Of the other models that describe field evaporation, charge draining is the most broadly accepted, which was originally developed by Gomer [82] [83] [84]. In charge draining, rather than the ion being fully ionized at the critical distance, the charge is progressively drained out of the ion as it leaves the surface [85].

Full quantum mechanical treatments of field evaporation have not yet been achieved, although some initial insights are available from simulation and density functional theory [86]. These are areas of current field evaporation research and will not be focused on in this document.

Instrumentation

All reported datasets were acquired with local electrode atom probe (LEAP) systems. Some data was acquired at the Center for Advanced Energy Studies – Microscopy and Characterization Suite (CAES-MaCS) in Idaho Falls, Idaho using their LEAP 4000X-HR system under user proposal number CCN 224229. Another group of data acquisitions were performed using the LEAP 3000X-HR system at University of California at Santa Barbara. The final datasets referenced in this document were acquired at the Environmental and Molecular Sciences Laboratory (EMSL) at PNNL, using their LEAP 4000X-HR system.

Both the LEAP 3000X-HR and LEAP 4000X-HR systems utilize reflectrons to improve mass-resolving power. The most significant difference between the two systems is an improved laser system (in the LEAP 4000X-HR). The laser system allows LEAP instruments to acquire APT data from non-conducting materials. However, since MA957 is conductive, all datasets in this work were acquiring using voltage pulsing. Therefore, when operating in voltage pulsing mode, there is no difference between the two instrument models.

A LEAP system records a number of controlled and uncontrolled variables during acquisition of a sample dataset. Controlled variables are those specified in the run conditions, such as specimen temperature, pulse frequency, voltage pulse fraction, vacuum chamber pressure, applied voltage, and detection rate. Typically, in voltage mode, an acquisition is controlled by changing the applied voltage to maintain a constant detection rate.

All presented data was collected in voltage mode, at a temperature of 50 K (measured at the cryogenic heater), with a pulse frequency of 200 kHz, a pulse fraction of 0.2, chamber pressure between 10^{-10} and 10^{-11} Torr, and a data acquisition rates between 0.3% and 0.5%.

The LEAP output is three-fold. First, the position sensitive multi-channel plate detector records the location (x, y) of ion counts on the plane normal to the specimen tip axis. Second, by measuring the time between a voltage pulse and a hit on the detector, a time of flight for each ion count is also recorded. Lastly, the sequence of evaporation is logged, which, through a geometric transformation, is converted into the location of the ion count along the tip axis (z). An archetypal APT data acquisition results in a four-dimensional dataset with the number of ion counts ranging from millions to billions. In this study, Microsoft Excel and Ametek Inc. – Cameca's integrated visualization and analysis software

(IVAS) package located at UCB was utilized to perform all data processing and analysis [87].

Principles of tomographic reconstruction

Reconstruction in APT is a complex problem, in that not only are the specifics of the algorithm not publicly known, but the physical processes behind field evaporation are not fully understood or quantified. However, basic principles of the reconstruction process are well known. All reconstructions are founded on the idea that the radius of curvature of the tip and the electric field are related, and that the sequence of evaporation can be converted into a depth coordinate for each ion. The equations and figures in this section are exquisitely laid out in [75], and are reproduced in this document for clarity of discussion.

Knowing that the electric field (F) is inversely proportional to the curvature of the surface, and assuming that the shape of the specimen apex is spherical and smooth, the radius (R) can be determined by

$$F = \frac{V}{k_f R}$$

Where V is the applied voltage and k_f is the "field factor" or a constant that modifies the resulting field by accounting for the shank of the tip, reducing the field relative to that of a sphere [88].

Creating a reconstruction requires the knowledge of the evolution of the radius of the tip over acquisition duration. Since the shank angle of a specimen tip is non-zero, over the course of the acquisition, the tip will blunt. In order for field evaporation to continue, the applied voltage must be increased, as the radius of curvature increases. To address this, most APT acquisitions are controlled based on maintaining a constant detection rate, increasing the applied voltage if the detection rate falls below a certain threshold. Then, by assuming that the tip apex is spherical, and that the material exhibits a constant, global evaporation field (F_e) throughout the acquisition, the radius of the tip for the i^{th} ion count is given by

$$R_i = \frac{V_i}{k_f F_e}$$

Once the radius of curvature of the specimen for the i^{th} ion count is known, the coordinates normal to the tip axis (x_i, y_i) can be determined using the location of each hit on the detector and the known lensing/magnification effects of the instrument.

The location of each ion count along the tip axis (z_i) is determined by the sequence of evaporation. Assuming that each ion is emitting from a surface whose apex is located at z_{tip}

for each detected ion. As ions are emitted, the emitting surface is retreating from the detector by a small amount, *dz*.

$$z_{tip}^{(i+1)} = z_{tip}^{(i)} + dz$$

The calculation of *dz* is related to the total volume of the acquisition. The acquired volume is given as

$$V_{evap} = \sum_{n_{evap}} \Omega_i = n_{evap}\Omega$$

Where V_{evap} is the total acquired volume, n_{evap} is the number of ion counts, Ω_i is the ion volume for the i^{th} ion count, and Ω is the average ion volume. Of course, limited detection efficiency η, reduces n_{evap} to n_d by $n_d = \eta n_{evap}$.

The evaporated volume can also be described by the geometry of the specimen containing the n_{evap} ions. If a function w_V is defined that describes how the tip geometry evolves with changing z, and $w_V n_{evap}$ describes how the tip volume evolves with changing z, then V_{evap} can also be written as

$$V_{evap} = \int_0^{z_{max}} w_V(z) n_{evap} dz$$

Combining the two equations defining V_{evap}, it can be seen that *dz* is given by

$$dz = \frac{\Omega}{\eta w_V(z)}$$

Estimating $w_V(z)$ remains the biggest difference among the existing reconstruction methods.

Aberrations

While APT data in general suffers from a number aberrations resulting from different physical processes, detection efficiencies, geometric features and reconstruction procedures, the most important aberration to consider when analyzing reconstructions of ODS steels is termed trajectory aberration.

Implied in the reconstruction model, is an assumption that $w_V(z)$ is not dependent on ionic identity. That is to say that field evaporation occurs homogeneously across the spherical tip surface. While this may be true (or at least to good approximation) with pure metals (such as single crystal iron or tungsten), more complex systems may deviate significantly. In the case of ODS steels, the oxide particles maintain a much lower evaporation field than that of the iron matrix. This means that the oxides see a much higher evaporation rate, which causes high hit densities on the detector and local changes of tip geometry. The modern reconstruction process cannot accommodate the local change in evaporation

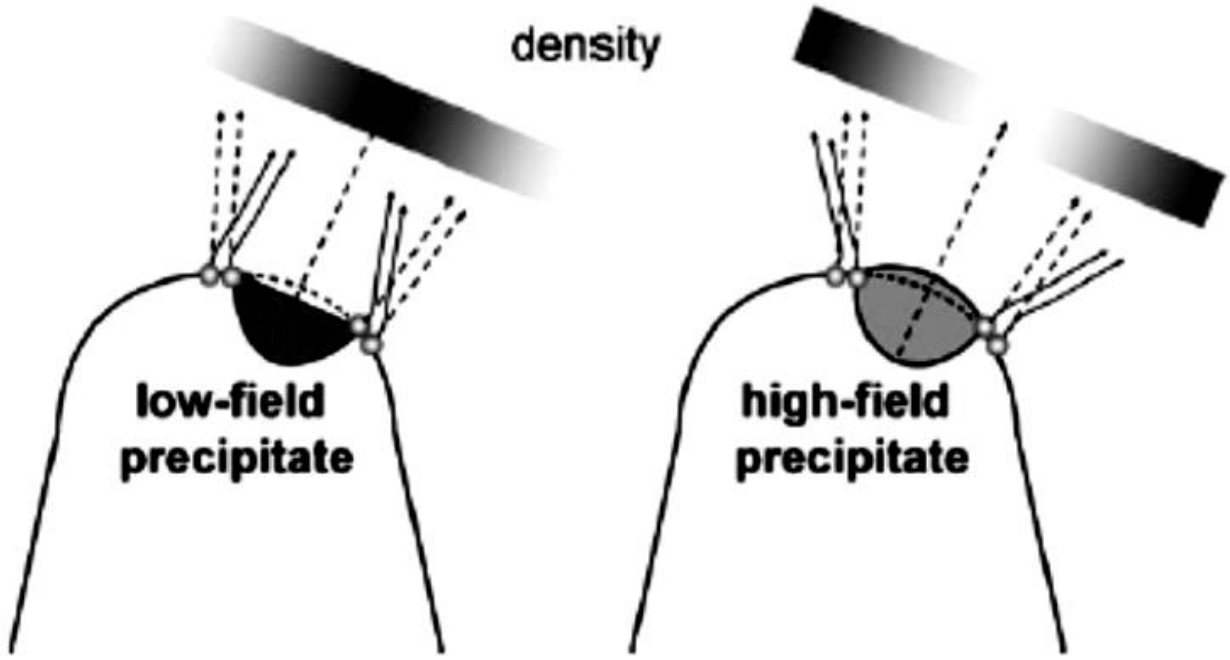

Figure 3.6 Schematic illustration of trajectory aberration in APT. Reproduced from *[75]*.

sequence or location. Such artifacts affect the entirety of the reconstruction in complex ways.

Not only does the rate of evaporation differ between the oxide and the surrounding metal, but the local geometry change causes variation in the initial trajectory of the emitted ions. This is shown schematically in Figure 3.6. As ions tend to leave the surface along the electric field lines, when a local change in geometry occurs, the ions no longer evaporate with an initial trajectory tangent to the presumed surface geometry. This off-tangent initial trajectory can cause ions to be detected in locations that are not where they originally were located.

Reconstruction approaches

While principles of generating an APT reconstruction provide a skeletal framework for creating a reconstruction, the ambiguity from the $w_V(z)$ term creates a number of problems. Since the exact mechanisms of field evaporation are not understood, and there exist a number of known aberrations, such as trajectory aberration, reconstructions are generally done on a case by case basis with the understanding that some or all of the data may be affected. With the current state of knowledge of APT, this drawback is unavoidable. Therefore different reconstruction methods exist for looking at different types of material, and for answering different types of inquiry. The reconstruction and analysis is then adjusted so that the result is minimally affected by all known aberrations.

One method to calibrate a reconstruction, or to change the reconstruction parameters to achieve an improved $w_V(z)$ is to utilize *a priori* knowledge about the material system. Correctly reconstructing that aspect of the system implies the calibration of other features. For example, in ODS alloys, one could consider the lattice constant for body-centered cubic

(BCC) iron (2.87 Å). By indexing one of the crystallographic poles in the APT dataset and adjusting reconstruction parameters to meet the expected distance between the atomic planes of iron in that orientation, the reconstruction could be calibrated to the iron matrix. However, the trajectory aberrations occur with the location of the oxide particles. Calibrating the reconstruction to iron, substantially distorts the structure of the oxide particle. Since the oxide particles are the feature of interest in these investigations, it does not make sense to utilize a calibration approach that is certainly going to contribute to further distortion of the reconstruction in the area of interest.

Another method for calibrating the reconstruction is to vary the reconstruction parameters such that the oxide features exhibit their "average" shape. The idea is akin to adjusting the stigmation on an electron microscope. In an electron microscope, it is desired that the beam spot be round, in order to induce the least distortion to the images formed by its interaction with the subject. By adjusting reconstruction parameters; the shape of the oxide enrichments can be modulated, from flattened ellipsoids (pancakes), to spheroids, to elongated ellipsoids (hot dogs). The effect of varying reconstruction parameters (in this case the global evaporation field F_e) on precipitate geometry can be seen in Figure 3.7. By selecting parameters that yield spheroid particle morphologies, the reconstruction can be presumed to exhibit the least distortion.

Interestingly, Figure 3.7 illustrates that changing the F_e not only affects the apparent precipitate morphology, but also has an effect on the length scale of the reconstruction. The length along the tip axis (z) in the right image in Figure 3.7 is ~30 nm, while the length of the same dataset with an increased evaporation field on the left is ~80 nm. So, given one set of reconstruction parameters, the length of the acquired volume may not be the same as

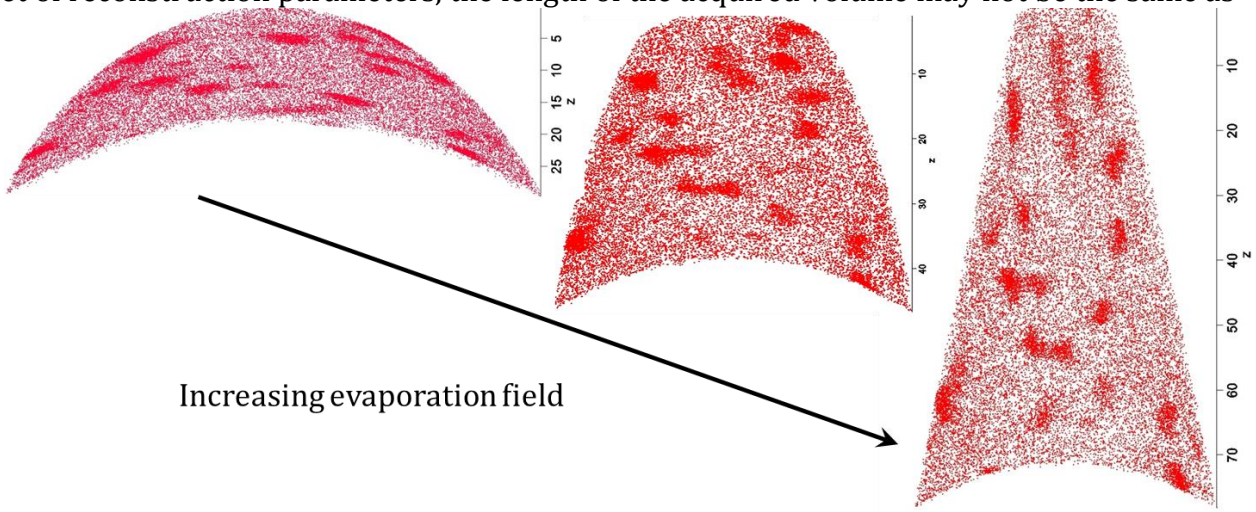

Figure 3.7 Illustration of the effect of increasing the global evaporation field on the shape and size of the reconstruction.

that of another set of reconstruction parameters.

Furthermore, this methodology contains a tacit assumption that the oxide particles were spheroidal in the first place. This is not necessarily the case. In fact, HRTEM studies carried out by the author and collaborating researchers have shown that in MA957, the

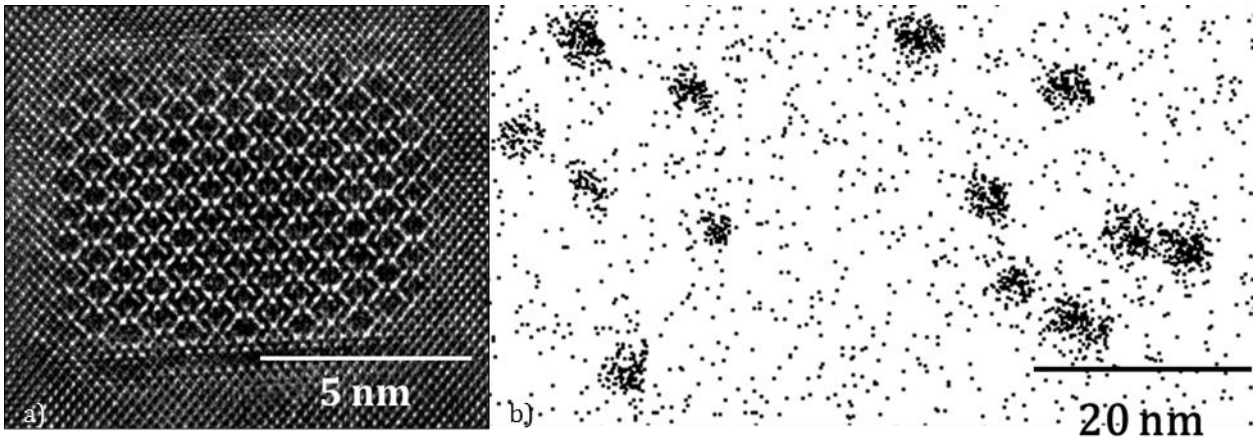

Figure 3.8 a) HRTEM image showing a cuboidal oxide particle in ODS metal matrix *[45]* b) APT reconstruction showing spheroidal oxide particles in the ODS metal matrix.

geometry of particles with diameters ~1-10 nm is cuboidal (Figure 3.8a) [45]. Assessment of the crystalline structure (pyrochlore) of the oxide particles supports this cuboidal nature. However, in APT, the oxide particles are spheroidal (Figure 3.8b), even when examining particles on the larger end of the spectrum (8 – 10 nm). This consistent loss of shape information implies a significant loss of spatial resolution in the ion counts in and around the oxide particles.

Therefore, if the investigation is attempting to measure oxide particle features, such as size, then using this method of modulating the oxide particle shape will bias these measurements, as the nature of the reconstruction has changed in order to induce a particular shape to the particles of interest.

Both of the above listed approaches induce artifacts and/or bias to the measurement of the oxide particles. In fact, the trajectory aberrations prevent any current reconstruction method from provide artifact-free reconstruction. Therefore, no matter what reconstruction methodology is used, the oxide particles will always be distorted in some manner. Since there is no established metric to compare the degree to which each reconstruction method distorts the oxide particles, there is no way to make a least-worst-of determination.

Therefore, the method of reconstruction chosen to be employed in this work was the simplest and most repeatable option, which is to reconstruct the data using a constant evaporation field (the evaporation field of iron 33 V/nm) and a constant global ionic volume (atomic volume of an iron atom – 0.0084 nm^3). This methodology will certainly induce distortion to the reconstruction, but it will induce similar distortion to each dataset, and thus the measurements will be comparable to one another. All data analysis was performed on datasets that were reconstructed with a constant evaporation field of 33 V/nm.

As a consequence, in this study, reconstructions are not regarded as quantitative tools for material evaluation. Reconstructions are used to visualize APT data and to suggest areas for further quantitative analysis by some other means. In this work, reconstructions only

offer visualizations of data, and do not contribute to the quantitative analysis of the microstructural features. Figures showing reconstructed data are intended to illustrate most clearly the feature of interest in the figure. Reconstruction parameters may have been changed to improve the visual clarity of the feature.

Reconstruction space versus real space

As should be apparent at this point, reconstruction space, the four dimensional grid upon which the experimentally obtained ion counts are distributed, is fundamentally different from real space. Although the reasons for this difference have been explained above, it is critical that this distinction between reconstruction space and real space be maintained. The reason for this distinction is that an APT reconstruction may look very close to expectation, e.g. a planar enrichment of solutes may look like a grain boundary, however, due to reconstruction aberration and data collection problems, that plane may not have the same character as the grain boundary did in real space. Further it is impossible to verify the plane's character (perhaps it is some other planar enrichment feature and not a grain boundary at all) post facto, as the specimen has been destroyed.

Unlike electron microscopy, APT has no defined image transfer function. While this may push some to claim unreliability of APT data, in fact, APT still provides unparalleled clarity into nanoscale three dimensional structures. Simply put, one must ask the right questions of APT to get a correct answer.

Isotopic measurement

Until this point, the discussion of reconstruction has been limited to the distribution of the Cartesian coordinate system to the detected ions. The final piece of completing a reconstruction is the classification of the ion species contained within the analyzed volume. The APT process measures the time of flight of the ions, which can be used to deduce the mass-to-charge ratio. The potential energy (E_{pot}) of a charged particle in an electric field (V) is given by

$$E_{pot} = neV$$

Where n is the charge state, e is the charge of an electron. If it is assumed that all of E_{pot} is quickly converted into kinetic energy (KE) then

$$E_{pot} = neV = KE = \frac{1}{2}mv^2$$

Where m is the mass of the particle and v is the velocity of the particle. Noting that the particles velocity is simply the length across which the particle traveled divided by the time it took to traverse the distance, and rearranging

$$v = \frac{L_{flight}}{t_{flight}} \therefore \frac{m}{n} = 2eV\left(\frac{t_{flight}}{L_{flight}}\right)^2$$

By combining the measured time of flight for each ion and the known flight length of the instrument, the mass to charge ratio of the ion can be determined.

Isotopic identification

Having converted the time of flight measurements into mass-to-charge ratios, an isotopic identity can be assigned to each ion count. These identities are based on the natural isotopic distributions of elements in the periodic table.

Interpretation of mass spectra, like the one shown in Figure 3.9, can be complex. One complicating aspect is the existence of so-called "peak overlap." Peak overlap is a situation in which two isotopes of different elements occupy the same mass to charge state. Since mass spectroscopy cannot distinguish between elements, some degree of uncertainty in the elemental assignments is introduced by the peak overlap phenomena. For example, in

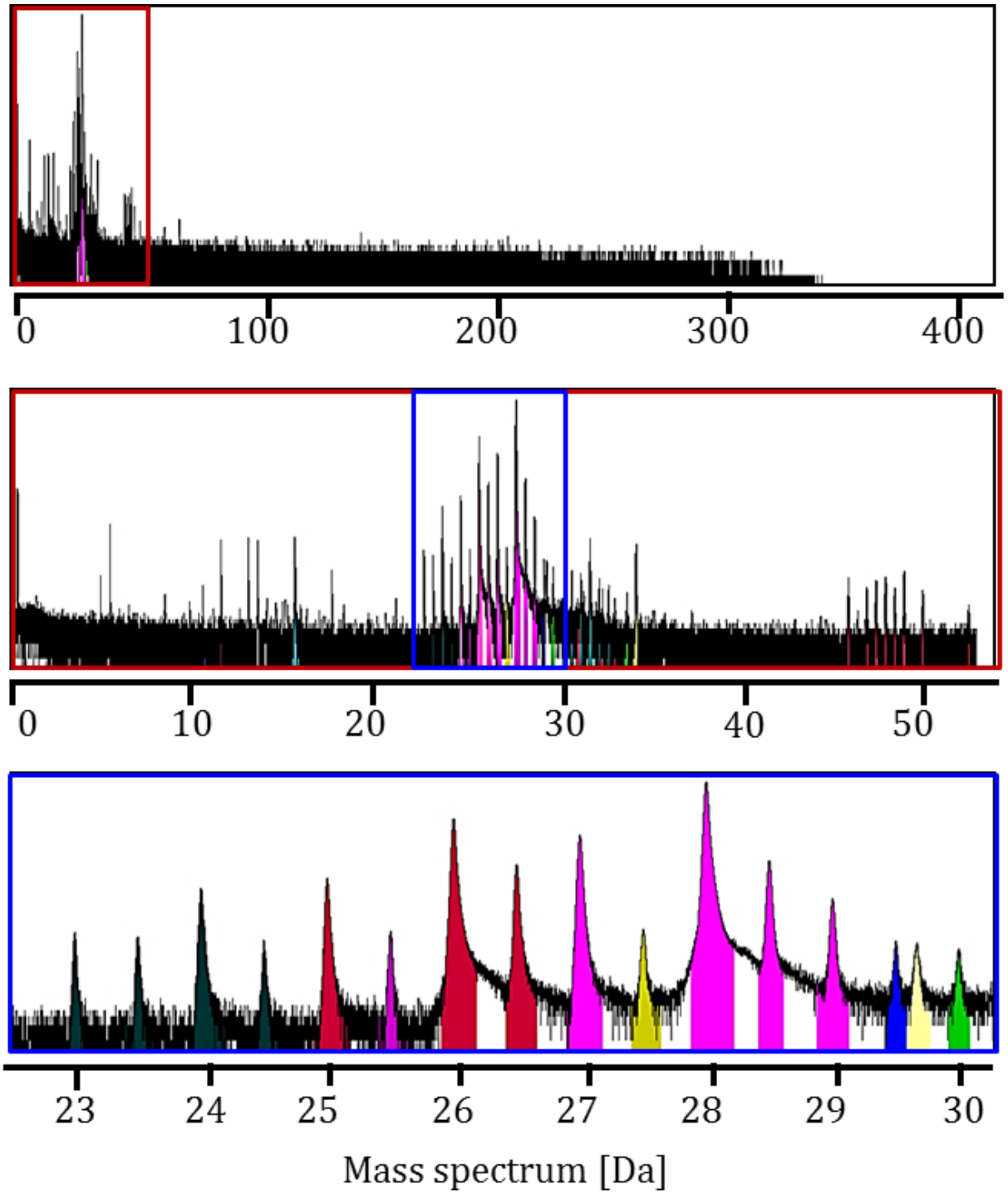

Figure 3.9 Representative mass spectrum from APT acquisition of an ODS steel alloy.

Figure 3.9, iron and chromium exhibit peak overlap at a mass to charge ratio of 27 (In fact, this peak is also shared by aluminum). As a result, any ion count that falls within that peak in the mass spectrum has some probability of being iron, chromium, or aluminum. These ratios in some cases can be determined by measuring the height of adjacent peaks. By assuming natural abundance of isotopes, the height of the iron contribution to the 27 peak can be calculated from the known ratios to the heights of other iron isotopes peaks. A similar process can be done for chromium, and the excess is attributed to aluminum, as it only has one major isotope.

Another complicating feature of classifying the isotopes is how to bin and range the spectrum. By increasing the bin size, the statistics for the number of counts within each bin are improved, but the resolution of the spectrum is reduced. By reducing the bin size, the resolution is improved, but the confidence in the number of counts in each bin is reduced. This is a problem common to any measurement based on count statistics; however, as APT is a destructive technique, small peaks cannot be grown to larger size by adjusting the counting time, they are simply small peaks. Many authors simply rely on the default settings of the IVAS suite to determine the binning of the mass spectrum. In this work, the default binning schema used by IVAS will be utilized.

Ranging is the term used to describe selecting a region of the mass to charge spectrum and classifying it as a single element. The width of such ranges is entirely controlled by the user. Using a thin range, relative to the full-width half-max of the peak, the ions added to the reconstruction will contain very little noise. Using a wider range, will include more real isotope counts, but also increase the noise counts visible in the reconstruction.

While in theory, peak width varies from charge state to charge state, the width of peaks within each charge state should be the same. For example, in Figure 3.9 the iron peak at 28 is wider than the chromium peak at 26. However, this difference in width is only due to the increased number of iron isotopes counted with a mass to charge ratio of 28. So, it would follow that the two peaks should have a range that is the same width. But, if this logic is applied a peak that is much smaller, such as the manganese peak at 27.5, this will lead to a substantial increase in the signal to noise ratio, and in fact lead to overcounting of dilute solutes. Reversing this idea, using small peaks to determine the range width for the larger peaks will lead to systematic undercounting of major species.

Currently, many authors use their own best judgement to apply classifications to the mass spectrum. This, of course, leads to concerns about the comparability of APT data even in its most raw form, as what element a count is classified as directly influences all subsequent measures of that count. This is one of the foremost standing problems in APT research today. Developing a clear binning and ranging strategy is paramount to the furthering of APT research. Due to time and experiment constraints, in this work, ranges were picked to attempt to capture the entire peak, but exclude contributions from the noise floor. No standard peak width was applied, each peak was addressed individually.

All range files (the file used to interpret the mass-to-charge spectrum of the LEAP output data into elemental identities) were created assuming natural abundances of the detected isotopes.

Another curiosity illuminated by comparing APT data on ODS steels to HRTEM data on ODS steels is the difference between reported stoichiometries. HRTEM reports vary on the identity of the crystal structure of the oxide precipitates; $Y_2Ti_2O_7$ pyrochlore, YTi_2O_5 orthorhombic, $Y_xTi_{1-x}O$ defective halite, and amorphous Y-Ti-O have all been reported. In all likelihood, many or all of these phases are present in some capacity in ODS steels. In many cases, HRTEM studies report the properties of a handful of oxide precipitates. APT on the other hand, reports the composition of a relatively large number of oxide precipitates. In this study, more 3000 oxide precipitates have been characterized. However, the composition measured by APT is suspicious. This is due to the fact that the Y concentration is too low. Not only is the yttrium content of the oxide particles significantly lower than the stoichiometric composition suggested by HRTEM studies, but is lower than the expected value from bulk composition studies. This systematic undercounting of yttrium has been reported before, and the compositional measurements of APT investigated oxide particles is consistent.

Undercounting of yttrium is a long-standing problem in the APT study of ODS steels and one that has no simple solution. It is thought that a problem with interpretation of multiple ion hits on the detector may result in the loss of yttrium data, but this theory has yet to be unequivocally proven. This draws into question the validity of stoichiometric measurements of oxide particles in APT. However, again, the discrepancies between reconstruction space and real space are consistent. Therefore, particle compositions are comparable between APT sets, but should not be compared to other compositional measurements.

Raw data treatment

To begin the description of data analysis, it is important to point out the ambiguity in the term raw data in APT. Raw data, in principle, would be the machine output data, with no filter, or manipulation. The data would be given as machine settings, then log data for each collected ion, such as time of last voltage pulse, time of detector hit, current measurements from each node of the multi-channel plate, standing voltage at the time of the voltage pulse, pulse amplitude, specimen temperature, and chamber pressure. However, due to the proprietary nature of the LEAP instrument, its operation software and the IVAS suite, this raw data is interpreted internally, prior to, and during the reconstruction process.

Due to this closed-source data manipulation leading to the generation of a reconstruction, the data stream and physical process models contained within it are largely unknown. Moreover, aberrations inherent to the field evaporation process itself add further unknowns, and poorly accounted for, uncertainty to the raw data, which then translates to an even more uncertain reconstruction.

While it is obvious that these practices will raise concern about the validity of the results, as well as any claim to accurate experimental uncertainties, there is no clear path to avoidance without building a machine and software packages from the ground up.

As such a ground up approach is not feasible within the scope of a single thesis, reconstructions generated using the IVAS suite will be considered the “raw data”. Validity

of results and conclusions will rely on careful selection of analysis questions: investigating metrics that are insensitive to such distorted and messy data. Furthermore, the data analysis will address metrics that provide meaningful results for materials properties estimation.

Ion maps

Ion maps are used in this document to illustrate chemical distributions within the samples. In literature, atom maps are commonly used to this end. However, the use of atom maps misconstrues possible differences in distributions of different ionic species. For example, Figure 3.10 compares atomic and ionic distributions of titanium in a sample dataset. Figure 3.10a depicts an atomic map of titanium, while Figure 3.10b shows an ionic map of titanium. The strong clustering evident in Figure 3.10a is not due to clustering of titanium ions, but in fact, the clustering of titanium oxide (TiO) ions, which are shown in Figure 3.10c. The use of atom maps would obscure such information in a way that is not recoverable. Therefore, all analyses are based on ionic identity until post-processing where metrics requiring decomposition, such as atom fraction, are calculated.

Analytical approaches for oxide characterization

The goal of the study of irradiated MA957 using APT is to understand the response of the

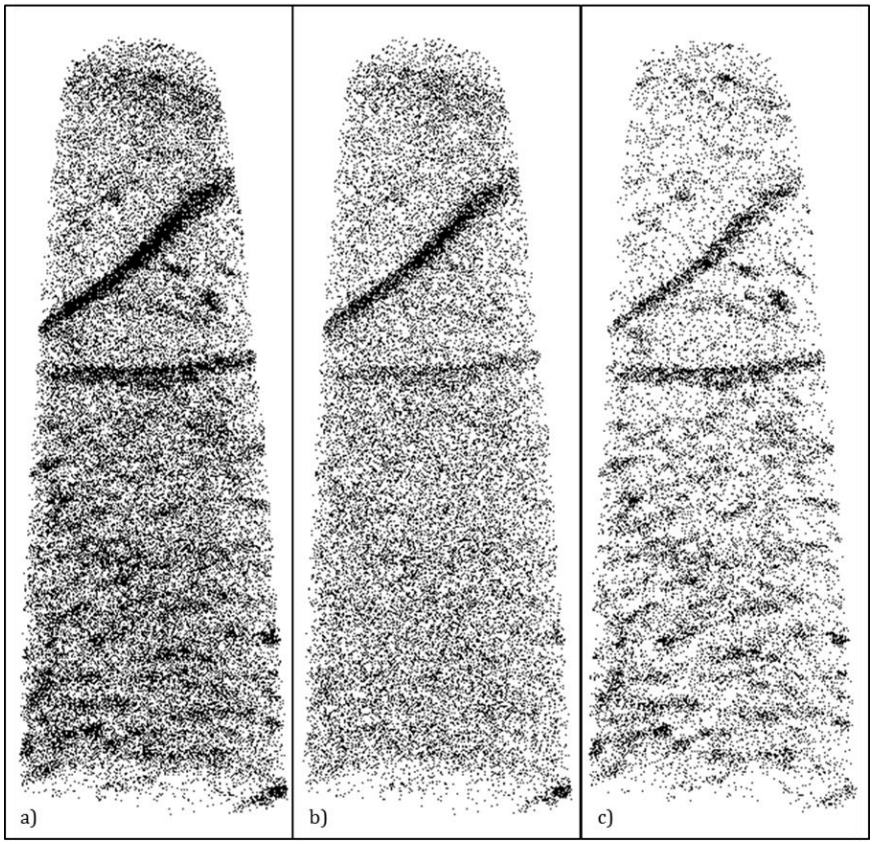

Figure 3.10 a) Atom map of titanium in a representative APT dataset b) Ion map of titanium in a representative APT dataset c) Ion map of titanium oxide in a representative dataset.

oxide particles to high radiation dose and elevated temperature over extended periods of time. In particular, this study strives to draw conclusions based on microstructure that explain the mechanical response of the materials to the experimental conditions. The dispersion hardening model proposed by Bacon, et al maintains that the increase in yield strength afforded by the introduction of dispersed particles is proportional to two factors: the number density and the particle size [89].

$$\Delta\sigma_{xy} = f(N_x, d_x) = \alpha_x M \mu b \sqrt{N_x d_x}$$

Where α_x is the obstacle strength, M is the Taylor factor, μ is the shear modulus, b is the magnitude of the Burger's vector, N_x is the particle number density and d_x is the average particle diameter. Besides α_x, which is typically empirically determined, all of the proportionality constants in this model are properties of the matrix rather than the dispersed particles. Therefore, when studying dispersed barriers for their effect on the change in yield strength the quantities of interest are N_x and d_x.

APT has some unique challenges in the analysis of dispersed particles. The major problem is trajectory aberration, resulting in the unexpected geometry changes exhibited by the oxide particles in Figure 3.8. This results in uncertainty the location of oxide solutes in and around the oxide particles that is not trivial in quantification. Furthermore, reconstruction space and real space diverge most dramatically at the oxide particles, again evidenced by the shape change, and therefore even with quantified uncertainties, it is not clear that a length measurement of an oxide will correspond to a length measurement made in real space. Therefore, the quantity d_x is not a real space quantity that can be directly measured from APT data. However, trends of size change (and compositional change for that matter) between APT datasets are perfectly valid, and will be used extensively in this work.

Eliminating measurement of a real-space value for d_x, the remaining property that governs the mechanical change induced by particle dispersion is N_x. Unlike d_x, N_x is a real space measurement that can be measured equivalently in reconstruction space. The number of particles is not dependent on the particle size, morphology or size of sample, the only criterion is to be able to reliably identify the existence of a cluster in the reconstruction. Cluster analysis is a methodology for identifying clusters within a dataset.

Cluster analysis

Cluster analysis is a technique which groups objects in a dataset by similarity [90]. The groups established are called clusters. The objects are the data points (in this case, Y-Ti-O solute ions) to be grouped by the analysis. Typically, the similarity of the objects is described by their closeness in data space. Data space is an n-dimensional space in which all of the data points lie, and n is the number of coordinates each data point is described by.

In the case of APT data, data space and reconstruction space are synonymous. The closeness of the objects is often measured using a distance metric in data space. The four dimensional reconstruction space contains three spatial dimensional (x, y, z) and one categorical dimension (ion identity). The ion identity could be thought of as another spatial dimension, as it is based on a time-of-flight measurement; however, thinking of the time-of-

flights as a spatial dimension radically complicates the problem, and does not offer significant improvements on the results. Therefore, the range file will be used to assign simple ion labels to ion counts with m/c ratios falling into the ranges specified by the range file. Since the remaining three dimensions are spatial, Euclidean distance is a perfectly adequate metric for defining the similarity between solute ions.

To maintain separation between descriptions of observations in real space and in reconstruction space, different terminology will be employed to describe the oxides. Oxide particle will be used to describe the oxides in real space and oxide cluster will be used to describe the oxides in reconstruction space.

While cluster analysis has been used for many years, recently it has been used in many applications of data mining, to simplify large and complicated datasets, identifying areas of interest. As a result, a number of cluster analysis algorithms have been developed. In APT, such algorithms and approaches have been studied for some time, and it has been found that it is important to optimize cluster search algorithms for each analyzed system. No single technique or set of parameters can universally be applied [75] [91] [92] [93] [94] [95].

Cluster analysis methods in APT

The cluster analysis approach that is used in APT is based on the evaluation of the distance between nearest neighbors. While there are a number of variations of this cluster analysis method, they are consistent with regard to two foundational parameters. The first parameter is the link distance, denoted d_{max}, which is illustrated schematically in the upper portion of Figure 3.11.

If two objects (or solute ions) lie within d_{max}, then they both belong to the same cluster. The second basic parameter is the order. The order describes the minimum of how many solutes must be within d_{max} of the solute being evaluated for inclusion in a cluster in order for the solute to be included. In Figure 3.11a), the order is one, so if there are any solutes within dmax of the evaluated solute, then it is added to the cluster. The smallest possible cluster is indicated in red, which consists of two atoms. In Figure 3.11b), order 2 is depicted. Even though the top-most solute has one nearest neighbor within d_{max}, since it does not have two nearest neighbors within d_{max}, it is not added to the cluster. Figure 3.11c) illustrates the corresponding cluster for an order of 3.

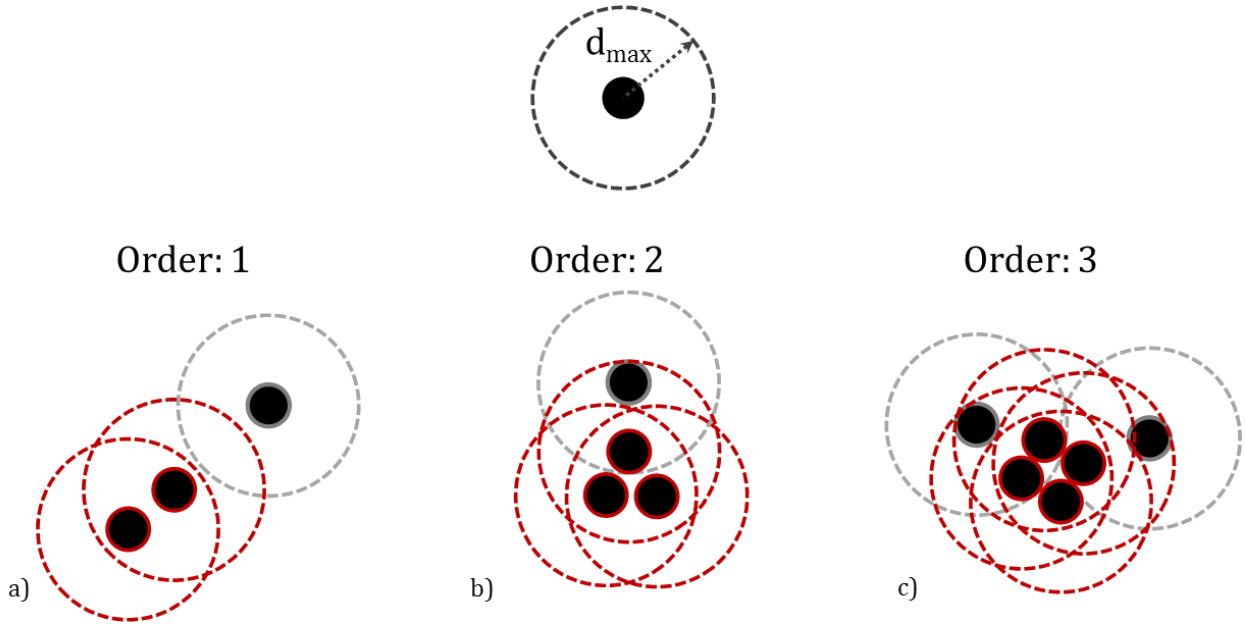

Figure 3.11 Schematic illustration of nearest neighbor cluster analysis parameters. a) depicted in red are two objects grouped by d_{max}, with an order of 1. b) depicted in red are three objects grouped by d_{max}, with an order of 2. c) depicted in red are four objects grouped by d_{max}, with an order of 3.

Since the primary goal of cluster analysis in APT is to find the number of clusters in the dataset, it is important to understand how the number of clusters found in a dataset changes with changing input parameters. This is shown in Figure 3.12. As d_{max} is increased, with order held constant, the number of clusters is reduced, as more solutes are added to existing clusters, and clusters are merged together. The density of solutes at the boundaries is also reduced, bloating the cluster morphology. As order is increased, with d_{max} held constant, the number of clusters is also reduced, but it is due to the smaller more disparate clusters no longer meeting the clustering criteria. The boundaries of the cluster maintain an increased solute density. The simulated dataset below was specifically designed to give the impression that there are two clusters in the data. However, due to the variations in the solute density across the dataset, the cluster search parameters had to be varied before the two clusters were identified. But, depending on the set of parameters that were chosen, the size and shape of the two identified clusters are radically different.

Clearly, the output of the cluster analysis is intimately tied to the selection of the input parameters. However, few methodologies exist that allow repeatable selection of such parameters. Furthermore, details of the individual systems cluster analysis is being applied to and the details of the particular cluster analysis algorithm result in the inability to use prescribed input parameters, as they must be redefined for each dataset.

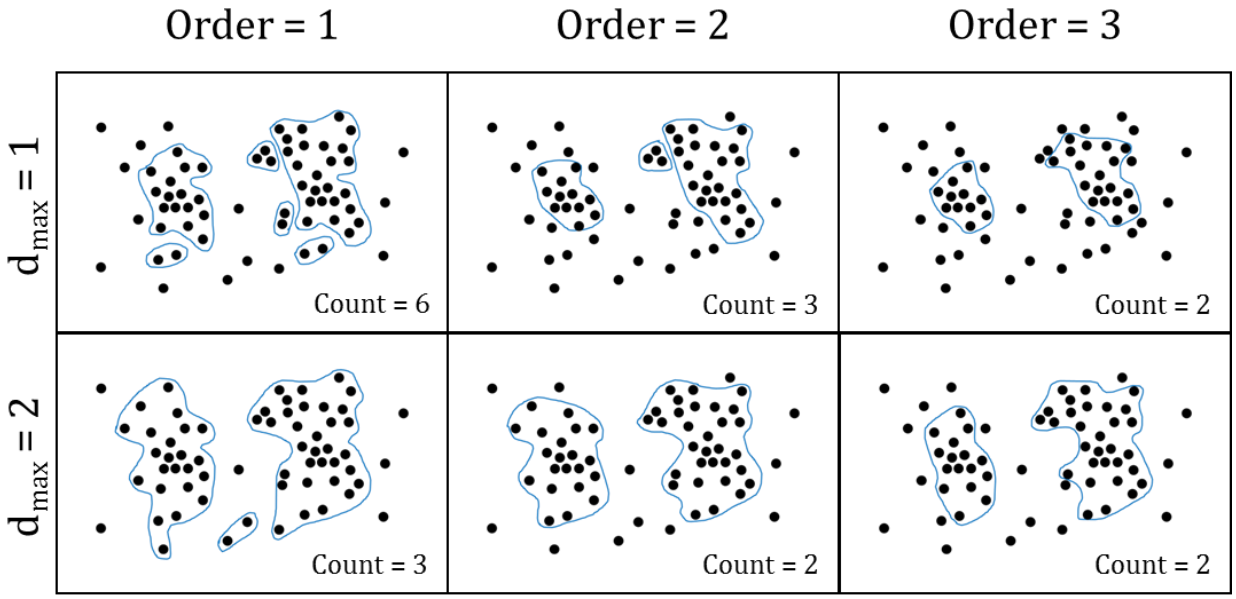

Figure 3.12 Cluster analysis results on a 2D simulated dataset illustrating the trends in the number of clusters found as d_{max} and order are varied. The identified clusters are indicated by the blue lines.

Since APT is a technique mainly utilized by materials scientists and physicists, the research motivations and priorities often vary from group to group. Many applications of APT require the use of cluster analysis to understand fundamental aspects of the data. While sometimes *ad hoc* parameter selection is sufficient it may lead to variations between authors and a more systematic approach might result in better data comparability.

For example, without the use of correlative microscopy, it is not possible to determine exactly the nature of the features that are being investigated. This is due to the nature of APT in that the image transfer function is not well known, thus the effect of the technique on the resulting image is not fully understood. The purpose of cluster analyses have been to select clusters whose properties (namely size) match most closely with correlative microscopy experiments. By comparing the precipitates shape and size in APT and the correlative imaging, cluster analysis parameters can be selected to "paint" the cluster in APT.

While there is no fault in using this methodology for validating the comparability of APT to other techniques, relying on correlative microscopy to verify the results of an APT experiment underutilizes APT's resolution and causes excessive work. In that approach, interpretation of features is limited to features that can be resolved by the correlating method. Furthermore, since the two images of the clusters are obtained through fundamentally different techniques, selection of clustering parameters is based on the scientists' interpretation of how well the clusters fit to the correlating image. This does not provide a repeatable method of analysis and prevents comparison to the work of other authors.

Another *ad hoc* approach has been to compare the resulting clusters to isoconcentration surface of a particular solute. An isoconcentration surface is a surface that connects all the

areas in the dataset of a given concentration. In the cases of dense solute segregations, isoconcentration surfaces draw ellipsoids that encompass the segregation. However, when the number of ions in an enriched region is small, the uncertainty in the location and morphology of the isoconcentration surface is large. Therefore, cluster analysis is used to quantitatively select the ions that are to be included in the cluster, but parameter selection is based on a visual comparison to the original isoconcentration surface. Again, this approach leaves room for interpretation in terms of the shape of the particle and the particle boundary, in a similar way to that of correlative microscopy. Furthermore, its repeatability is limited.

Both of the above methods for cluster analysis fail to provide repeatable experimental methods and introduce significant uncertainty to the generated results. A number of researchers have investigated the possibility of using cluster analysis itself to generate insights from APT data. This approach provides the possibility of repeatable measurements and methodological approaches that take full advantage of the resolution and character of APT data.

Modern methodological cluster analysis approaches

One of the most well-known approaches to APT cluster analysis utilizes a sensitivity analysis of input parametes, which was first suggested by Kolli, et al., [96]. Kolli used the maximum separation method, which was developed by Hyde [97] and varied the search parameters (d_{max} and N_{min} – the minimum number of solutes per cluster). While the maximum separation method used by Kolli does not use the same parameters as the density-based method used in this document, for the purposes of this discussion they function very similarly. Cluster analysis parameters were chosen from the d_{max} range where the number of clusters found does not vary with changing d_{max}. The plateau method was further developed by Williams, et al., [98] by defining an objective function that locates the region in the parameter space plateau where the number of clusters contributed from random association of solute ions is minimal. In that case, the maximum separation algorithm was also used.

Since cluster analysis is a generalizable technique, assertions must be made to reduce the number of possible cluster sets that might be of interest to the researcher. It is the selection of these reductions of cluster input parameter space that gives cluster analysis its inherent subjectivity. However, solutions that are valid for any material with precipitates can be established. The first rule is that clusters that indicate precipitates are assumed to be regions of high enrichment of solute ions. While distortions may exist in the data, this is the most reliable way to identify whether or not a precipitate existed in that spot.

The second assumption is to acknowledge that even in a randomly distributed set of points; some of the points will lie closer together than others. In order to establish cluster sets that have a low probability of containing clusters formed as a result of random association of solutes, a comparative cluster analysis is made to a homogenized APT dataset as shown in Figure 3.13.

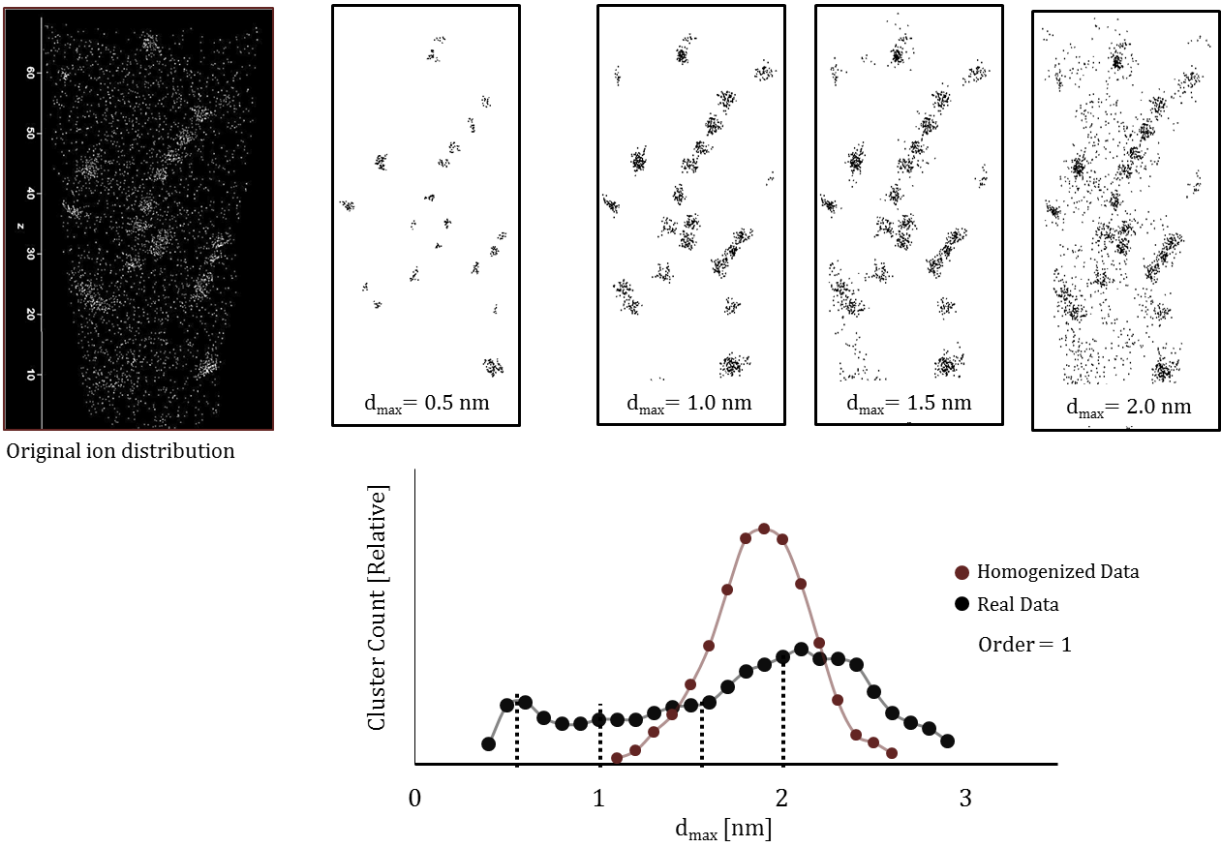

Figure 3.13 Illustration of effect of selecting parameters that overlap with clusters in the homogenized dataset.

The homogeneous dataset is generated by randomly re-assigning the ion labels on the existing x, y, z coordinates in the dataset. While this does not generate a perfectly homogeneous distribution, it provides a reasonable approximation while increasing the speed of calculation. Furthermore, using this methodology the distribution of ion labels is held constant, e.g. the number of counts of any species does not change.

Shown with a black background in Figure 3.13 is the raw test data from an example APT dataset. In the plot on the bottom, the number of clusters identified in the homogenized data and the test data are calculated for a number of values of d_{max}. In the plots with white backgrounds, the solutes that are determined to be clusters are shown, for each value of d_{max}. When d_{max} is low, and the number of clusters identified in the real data is high relative to that of the homogenized data, the clusters are fairly well-defined, with few solutes interspersed between the clusters. However, once d_{max} is increased such that the number of clusters found in both datasets is comparable (1.5 nm) or when the number of homogenized clusters exceeds the number of clusters found in the real dataset (2.0 nm), the influence of randomly associated clusters being identified can be seen.

In both of the datasets generated with a high d_{max} value, a significant fraction of the solutes are included in the cluster set, and a large number of the solutes are interspersed between the cluster cores that were pointed out at lower d_{max} values. This is a visual representation

of the concept of improving the signal-to-noise ratio in cluster analysis. The cluster count curve of the homogenized data can be thought of as the cluster background. These clusters are formed not by any causal mechanism in the system, but occur simply due to the random association of solutes at that density. It is paramount in a good cluster analysis that the signal to noise ratio be maximized in order to ensure that randomly generated clusters are not contributing significantly to the properties of the clusters that are being measured.

By the logic of maximizing the signal-to-noise ratio, the value for d_{max} that should be selected in Figure 3.13 is 0.5 nm. However, when examining the resulting clustered solutes and visually comparing to the original dataset, it seems that the clusters may be too small, excluding portions of the edge of the cluster that appears to be strongly contrasting the bulk solute concentration visually. There are some flaws in the way Figure 3.13 is plotted. The solutes that are plotted on the white backgrounds are the clustered solutes, but no distinction is made between which cluster each solute belongs to. Furthermore, this plot only illustrates the effect of varying d_{max} on the resulting cluster sets, while it has been shown above that varying the order can have a substantial impact on the results of the cluster search.

Figure 3.14 is a much clearer representation of the same concepts presented in Figure 3.13. This illustration applies cluster analysis of different orders and d_{max} to a constant test dataset. On the left side of Figure 3.14 is a cluster set of order 2, with a low d_{max}, selected by

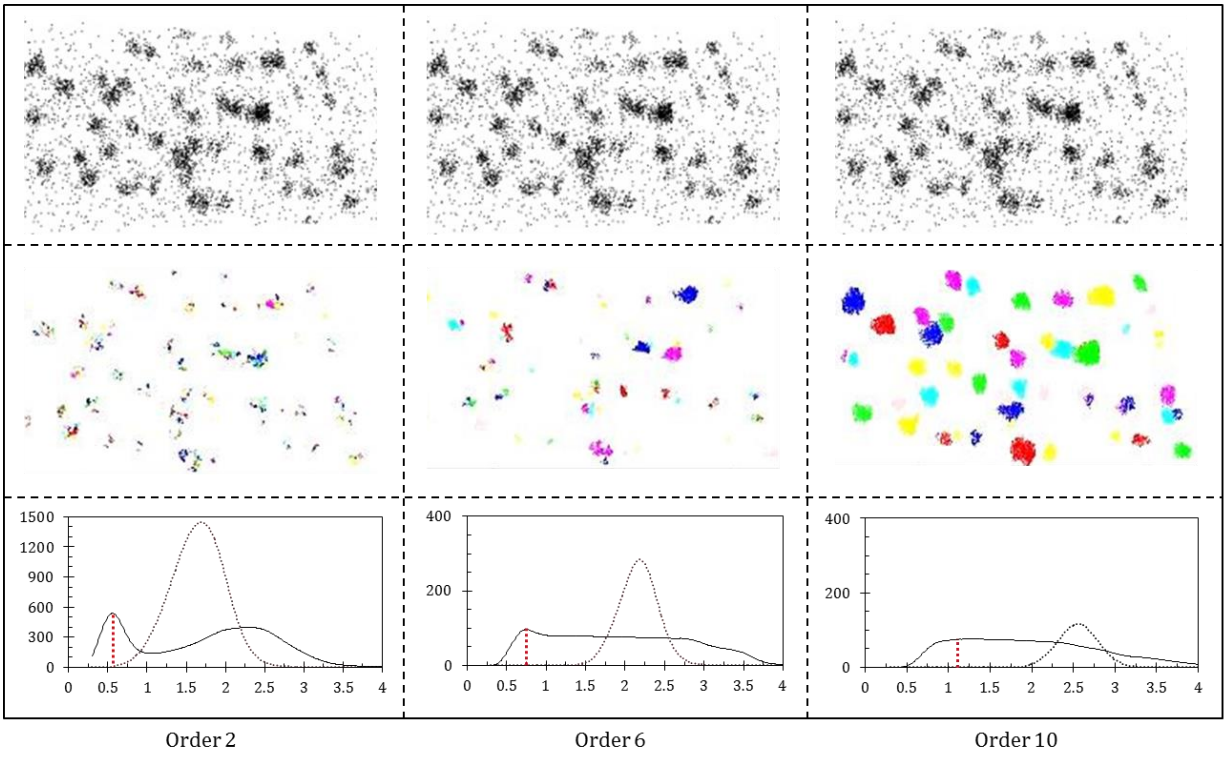

Figure 3.14 Illustration of the effect of changing the order on the cluster count vs d_{max} curve. The top plot shows a 2D example dataset. The middle plot depicts the result of the cluster analysis with the given order, and d_{max} value indicated by the red dotted line which was determined by maximizing the signal-to-noise ratio. Each different colored region in the middle plots indicate an individual cluster.

maximization of signal-to-noise. There is a distinct peak in the cluster count curve of the real dataset (the black line) for low values of d_{max}. In the image of the resulting clusters at order 2, the visually distinct clusters are broken up into several different regions, which greatly increased the number of clusters identified. As the order is increased, this separation of the visually distinct clusters is reduced, and at the same time, the height of the peak in the low values of d_{max} is reduced. By the time the order is 10, the peak at the low d_{max} values is completely gone, and the cluster sets marks very closely to the clusters that are expected to be included by visual inspection of the dataset. Intuitively, this approach makes sense. If there is a part of the dataset that has clearly defined clusters, then that implies that there is a finite, and well-defined number of clusters. Therefore, by varying the input parameters, there should be a region in parameter space where the number of clusters identified by the cluster analysis does not vary significantly. It is in this region that the input parameters should be selected.

This solution can also be seen from a different perspective. A cluster analysis algorithm that uses a link distance and an order parameter is an algorithm that links solutes into clusters that have the same solute density around them. In Figure 3.14, at order 2, the clusters are broken up into several smaller clusters. This is because even at low order, the d_{max} is so low that this search is finding the regions of high density in the dataset. While the high density regions are located in the visually-apparent clusters, the density is variable across their width enough that the high density regions are not linked. This is schematically illustrated by the blue line in Figure 3.15. What Figure 3.15 also illustrates is that the contrast between the background density and the visually apparent density can still be quite high. Once the search density has dropped to a sufficiently low value, the

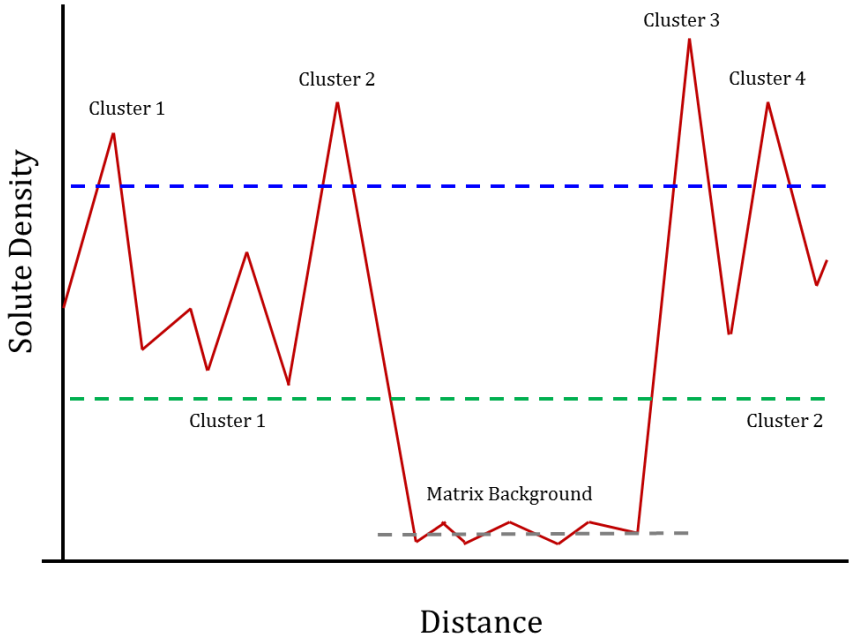

Figure 3.15 Schematic representation of solute density linescan across a region of clustered data. The blue line indicates a cluster analysis that looks for high density regions, e.g. low d_{max}, high order. The green line represents low density cluster search, e.g. high d_{max}, low order.

green line, the number of clusters found along the linescan does not change until the density is approximately equal to the background. The green line would indicate the type of search that is shown in Figure 3.14 by the right side.

The cluster count distributions shown in the bottom of Figure 3.14 are actually showing 2D slices of a 3D plot (d_{max}, order and cluster count), by showing iso-order plots in succession. In parameter space, a dataset with well-defined clusters has a large plateau in parameter space. An example of such a 3D plot is given in Figure 3.16. However, this plot only shows the number of clusters found for each parameter set in the test dataset. It does not account for the number of clusters found in the homogenized dataset (Figure 3.17). By subtracting the number of homogenized clusters found for each parameter set from the number of

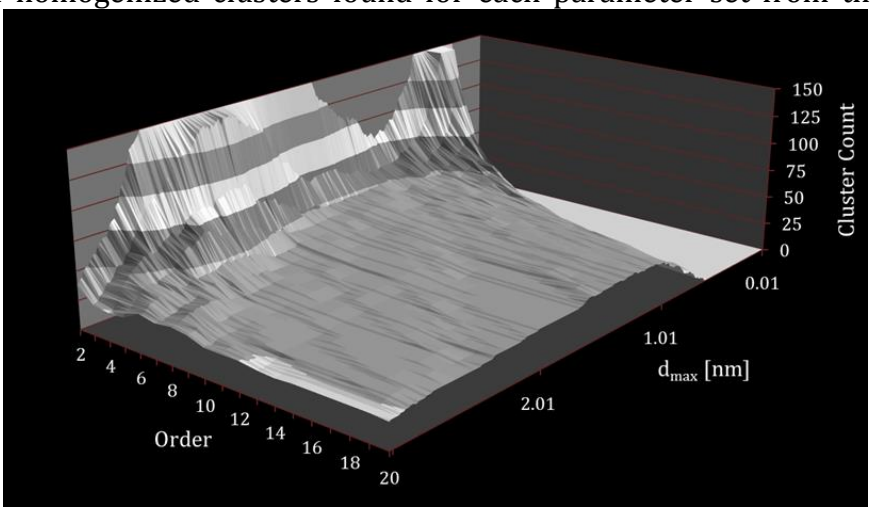

Figure 3.16 Parameter space plateau for a test dataset.

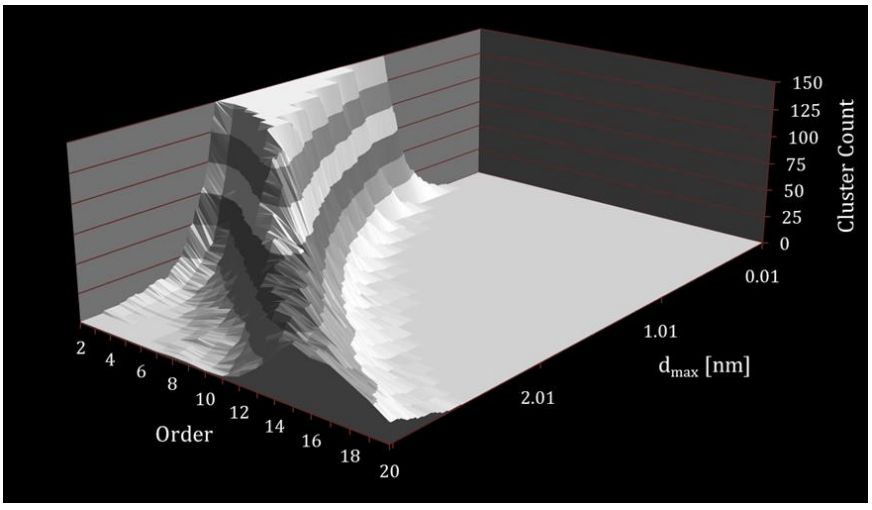

Figure 3.17 Parameter space plateau for homogenized dataset.

clusters identified by those parameters in the test data set, a new plot can be obtained: Figure 3.18. Figure 3.18 provides upper and lower bounds for the value of d_{max} and yields similar numbers of clusters over a wide range of order values.

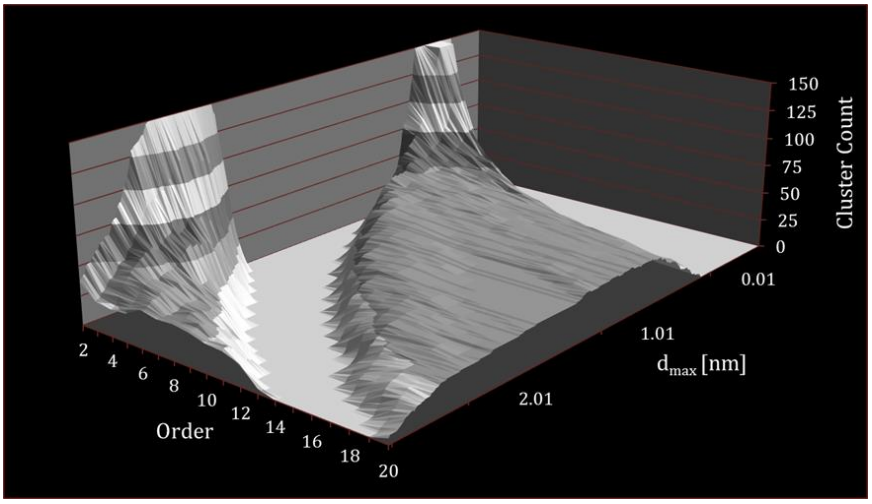

Figure 3.18 Parameter space plateau of the number of clusters from the homogenized dataset subtracted from the number of clusters found in the test dataset.

This method can be thought of as a sensitivity analysis of the cluster analysis algorithm. Since each dataset is different, the cluster analysis parameters that appropriately describe one dataset may not be appropriate for another. The advantage to using the sensitivity analysis procedure is it can be applied to different datasets, find different input parameters, but will identify the materials-relevant clusters in both cases. This allows cluster analysis results from the datasets to be comparable and repeatable.

In this work, the method of locating a plateau in parameter space will be used to determine the best cluster search parameters for analysis, but several modifications will be made to the method, in particular, the cluster search algorithm itself, and the method for selecting parameters from the plateau region. A density-based cluster search algorithm will be used to define the clusters, and a set of input parameter pairs with similar cluster analysis results will be used and pooled to define the cluster properties of the dataset.

In this study, Ametek Inc. – Cameca's IVAS package was utilized to perform all data visualization and data analysis procedures. Cluster analysis was used to investigate oxide enrichment features.

Post-processing of the resultant data from the cluster analysis tools was carried out with Microsoft Excel. This included data cleaning, statistical analysis and plotting.

Analytical approaches for grain boundary characterization

A prominent feature in many of the ion distributions that are shown in this document are planar enrichments of various solute ions. Although it may seem that such features are grain boundaries, this study contains no direct evidence for the assignment of that identity. No particular areal selection was performed, no *a priori* crystallographic data was obtained and the orientations of rolling direction and crystallography with respect to the tip axis were not controlled during sample preparation. Therefore, there is not sufficient direct proof to claim these features are grain boundaries.

Nonetheless, planar enrichments of solutes were observed. The composition of the planar objects is not the same as the bulk composition. The distribution of oxide clusters along the planar objects is not the same for all observations. In a number of cases, these planar objects intersected with clear triple-point boundaries, and some samples even contained several such boundaries.

These coincident facts suggest that the planar features are representing some sort of physical feature in the specimen tip. Generally speaking, perpendicular to the rolling direction, grain diameters can be as small as 100-200 nm. Therefore, it is not inconceivable that grain boundaries were intersected by the extracted tips fortuitously.

Accepting that there is no direct proof that these enrichments are, in fact, grain boundaries, the author believes the considerable circumstantial evidence for these features being grain boundaries justifies discussing them as such. For the remainder of the document, such features will be treated and discussed as grain boundaries.

Grain boundaries cannot be defined in terms of a number density, so the study of grain boundaries requires the development of some other metric. This metric must be independent of shape distortion. Compositional line scans are the metric of choice in this case. Line scans are chosen due to their areal specificity, and their insensitivity to contours of the plane. Since reconstruction only changes the compression of the image, data point relationships are maintained. Therefore, line scans are insensitive to reconstruction parameters and planar morphology

In this study, Ametek Inc. – Cameca's IVAS package located at UCB was utilized to perform all data visualization and data analysis procedures. Compositional linescans were used to investigate planar enrichment features.

Post-processing of the resultant data from the linescan tools was carried out with Microsoft Excel. This included data cleaning, statistical analysis and plotting.

3.4 Nanoindentation

Technique summary

Nanoindentation is a technique deploying a load cell and a displacement sensor during in an indentation instrument with high resolution and can be also viewed as high resolution instrumented indentation. This allows to produce well controlled and very small indents in a material sampling small volumes of material. Modern tools are highly automated so that a large number of indents can be performed in a desired position delivering large statistics.

The ability to collect data with good statistics from very small samples is especially important when dealing with radioactive materials, as the samples must be as small as possible to reduce the amount of activity which needs to be handled.

Nanoindentation is a technique which is able to measure the mechanical properties of a material at the sub-micron scale. A sharp indenter tip is pressed into a specimen material, and as the indentation is proceeding, the applied force and the displacement are simultaneously and continuously measured. By interpretation of the resulting load-displacement data, mechanical properties calculations can be made without needing to image the indent (Vicker's hardness requires imaging of the indent to calculate the hardness value). Furthermore, the positioning capability of the instrument is also sub-micron; it is possible to create arrays of indents to map the hardness of very small specimen regions.

Theory of nanoindentation

Using the method based on the unloading process developed by Oliver and Pharr [99] [100], nanoindentation strives to measure two material properties, the hardness (H) and the elastic modulus (E). A schematic of a typical load-displacement curve is given in Figure 3.19. Three quantities are gained from this plot, the maximum load (P_{max}), the maximum displacement (h_{max}) and the elastic unloading stiffness ($S=dP/dh$), which is the slope of the unloading curve at P_{max}.

Determination of E and H is based on the unloading process, shown schematically in Figure 3.20. Given a conical indenter of half-angle ϕ, and that pile-up is negligible, the amount of sink-in, h_s, is given by:

$$h_s = \epsilon \frac{P_{max}}{S}$$

where ϵ is a constant dependent on indenter geometry. Thus the contact height, $h_c = h_{max} - h_s$ is:

$$h_c = h_{max} - \epsilon \frac{P_{max}}{S}$$

By defining an area function, $A(h_c)$, that describes the contact area of the indenter as a function of h_c, H is given by:

$$H = \frac{P_{max}}{A(h_c)}$$

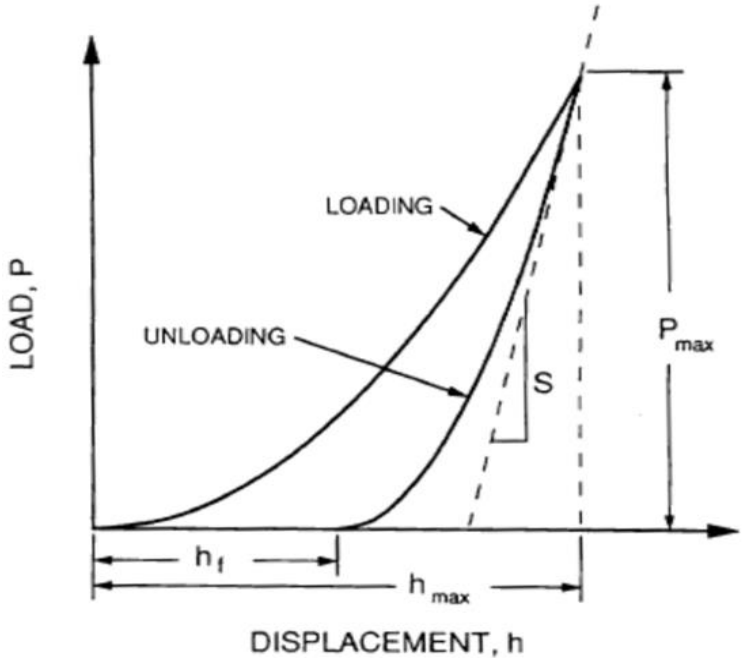

Figure 3.19 Schematic load-displacement curve for a typical nanoindentation experiment *[99]*.

Although the initial elastic deformation of the material is lost to the plastic deformation induced by the indenter tip, elastic information is still available via the material spring-back as the force on the indenter is unloaded. Determination of E follows from the unloading stiffness, S, given by

$$S = \beta \frac{2}{\sqrt{\pi}} E_{eff} \sqrt{A(h_c)}$$

Where E_{eff} is related to the E by

$$\frac{1}{E_{eff}} = \frac{1 - \nu^2}{E} + \frac{1 - \nu_i^2}{E_i}$$

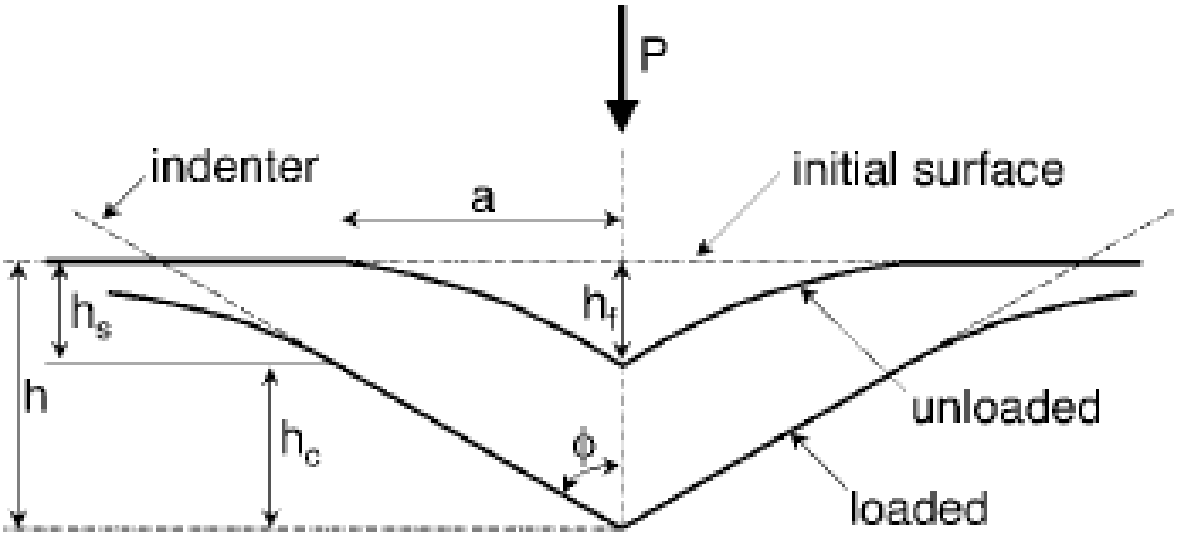

Figure 3.20 Schematic of the unloading process of a nanoindentation experiment *[100]*.

This takes into account the elastic deformation of the indenter tip itself, with elastic constant, E_i, and Poisson's ratio, ν_i.

This method relies heavily on the independent measure of the indenter contact area as a function of indentation depth (h_c) on material standards. Typically these standards are fused silica, copper, or stainless steel. It is also important to note, that is some cases, elastic-plastic deformation of materials leads to material pile-up at the edges of the indent. This phenomenon causes changes to the indenter contact area from the material standards, and thus requires careful treatment.

Samples and instrumentation

The mechanically polished sample coupons used to extract APT samples were utilized for the nanoindentation measurements.

The nanoindentation measurements were conducted at UCB on the Micro Materials NanoTest™. The NanoTest is designed with a horizontal tip-sample arrangement. This system allows loads of up to 500 mN without changing the transducer. In addition, the Micro Materials system is capable of heating the sample and tip assembly to 750 °C, allowing the possibility of high temperature material investigations. However, the effect of temperature was not investigated in this study.

Instrument conditions

Using a Berkovich indenter tip, 1 μm indents were performed in 5 by 5 indent arrays with a spacing of 30 μm between indents. The indentations experiments were depth controlled at a constant loading rate.

Instrument outputs and data analysis

The load-displacement curves output by the nanoindenter for each successive indent were collated and analyzed by the Micro Materials software suite, using tip area functions measured from fused silica material standards. Post-processing, statistical analysis and plotting of the datasets were performed using Microsoft Excel.

4 Results

4.1 Atom probe tomography

Oxide particle solute ion distributions

The aim of this section is to not only point out trends in ion distributions as a function of irradiation temperature, but also to identify the ion distributions that mark features of interest. Once an ion is chosen as a marker, the evolution of that ion distribution with irradiation condition can imply the evolution of the feature of interest with irradiation condition.

Shown in Figure 4.1 are representative ion distributions from a specimen irradiated to 113 dpa at 550 °C. These distributions are intended to illustrate the relationships between different ion species originating from the oxide particles, in order to establish a clear marker ion or set of ions. In MA957, oxide particles are primarily composed of titanium, yttrium and oxygen. The ion distributions that are shown in Figure 4.1a-e are titanium, yttrium, oxygen, titanium oxide, and yttrium oxide, respectively. It should be noted that the relationships demonstrated in Figure 4.1 are insensitive to changes in irradiation condition (e.g. an ion marker established at low temperatures can be applied equally well at high temperatures).

In general, the titanium distributions are uniform and homogeneous, with the exception of planar enrichments that are visible in Figure 4.1a. Since titanium is present in the metal matrix, and is not strongly clustered, titanium ions are poor markers of oxide particle location.

While oxygen ions (Figure 4.1b) do form clusters, these clusters are somewhat diffuse relative to other ion distributions. The diffuse nature of these ion enrichments is likely due to oxygen surface migration, which has been observed on other materials with complex electronic interfaces [101]. Due to the apparent delocalization of oxygen, it is also a poor marker of oxide particle location.

Although ion distributions of yttrium (Figure 4.1c) are strongly clustered, low counts lead to poor oxide particle identification. Systematic undercounting of yttrium is an outstanding research problem in APT [102]. It is expected that such undercounting is occurring in ODS systems, but the extent and exact mechanism is not well understood. Therefore, yttrium is not an adequate marker ion for oxide particle location.

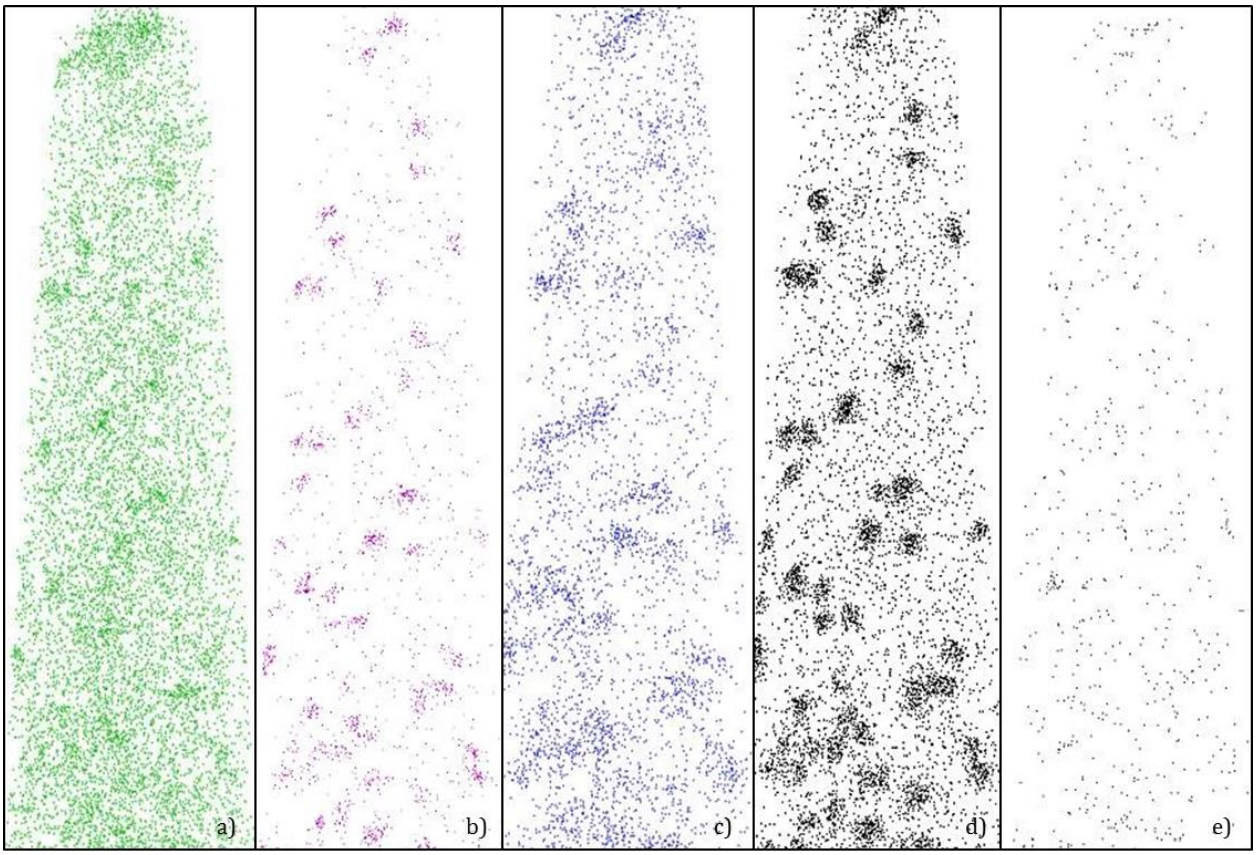

Figure 4.1 a) Titanium ion distribution (Ti^{+}, Ti^{++}) b) Yttrium ion distribution (Y^{++}, Y^{+++}) c) Oxygen ion distribution (O^{+}) d) Titanium oxide ion distribution (TiO^{++}) e) Yttrium oxide ion distribution (YO^{++}).

Titanium oxide (TiO) is a molecular ion which forms as a result of simultaneous evaporation of titanium and oxygen. It is expected that this event occurs only in the immediate vicinity of oxide particles, as titanium oxide is known to exist in the oxide particles, but not in the metal matrix. The titanium oxide ion distributions (Figure 4.1d) are strongly clustered, and maintain high counts. Titanium oxide is therefore the best ion marker to distinguish the oxide particles. It appears obvious that the TiO is the preferred method of evaporation from an oxide cluster from this figure. Considering that the total amount of Ti and O is set in a material and most of it evaporates as TiO it can be understood why the Ti and O signal alone is weak.

Yttrium oxide (YO) is another molecular ion that has been observed (Figure 4.1e). However, count rates are extremely low. In some specimens no yttrium oxide was detected. Therefore yttrium oxide is a poor marker ion for oxide particles.

Titanium oxide is used as the primary marker for the oxide particles, and for observation of oxide particle evolution over irradiation temperature. Though the other constituent ions contribute little to cluster identification, they are clustered in the same regions as the titanium. This supports the argument that titanium clusters mark the location of the Y-Ti-O particles.

Figure 4.2 shows representative titanium oxide distributions for each irradiation condition. At 385 °C (Figure 4.2a), relatively small titanium oxide clusters are observed at a high number density. At 412 °C (Figure 4.2b), slightly larger titanium oxide clusters are observed at a similarly high number density. At 495 °C (Figure 4.2c), titanium oxide cluster number density is noticeably reduced, and the size is increased. At 550 °C (Figure 4.2d), titanium oxide cluster number density is further reduced, and the titanium oxide cluster size is increased. At 670 °C (Figure 4.2e), titanium oxide number density is further reduced, and the titanium oxide cluster size is increased.

These changes in titanium oxide cluster size and density roughly fit into two categories: low temperature (385 °C, 412 °C), and high temperature (>495 °C). The transition from low to high temperature shows a stark drop in cluster number density, and increase in cluster size. However, transitions between irradiation conditions in each group are more subtle. It is observed that the low temperature group maintains a higher cluster number density and a smaller cluster size than exhibited by the unirradiated control material (Figure 4.2f). While the high temperature group maintains nominally the same number density and cluster size as the control material.

Overall, titanium oxide cluster number density tends to decrease as irradiation temperature is increases. Titanium oxide cluster size tends to increase as irradiation temperature increases.

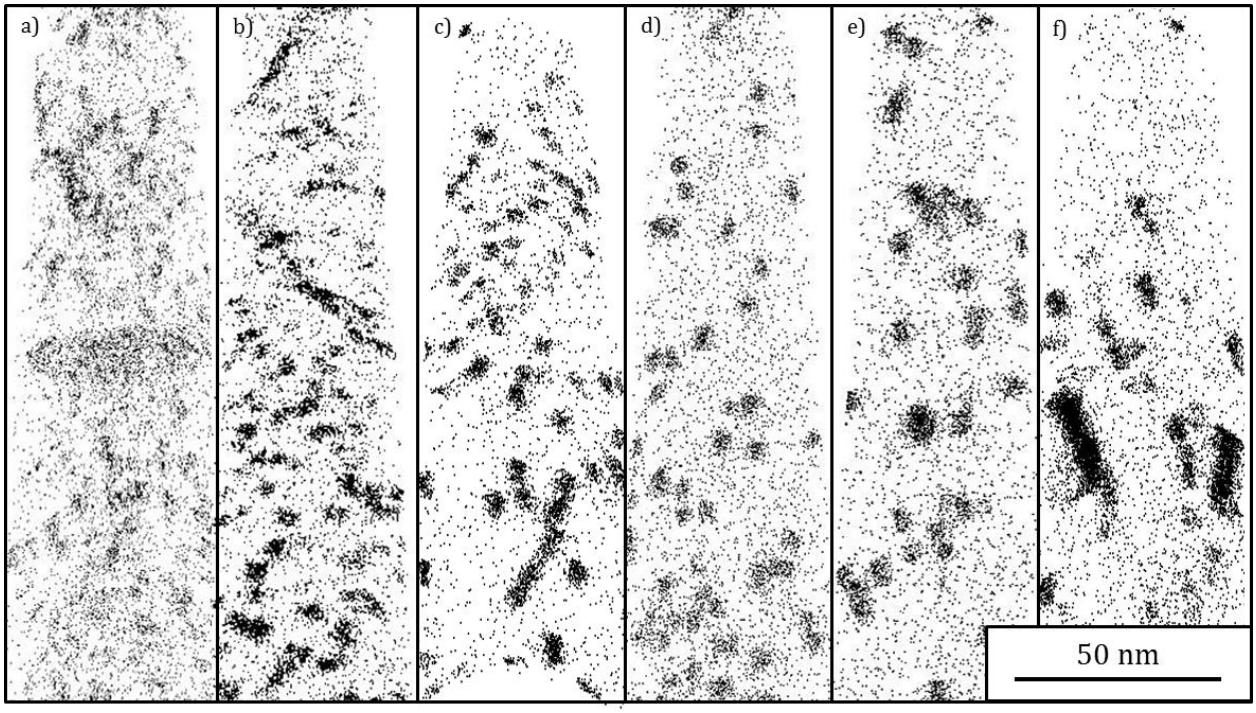

Figure 4.2 Titanium oxide molecular ion distributions as a function of irradiation temperature. a) 43 dpa - 385 °C b) 109 dpa - 412 °C c) 48 dpa - 495 °C d) 113 dpa - 550 °C e) 110 dpa - 670 °C f) Control.

Planar enrichments of solute ions

Similar to the identification of titanium oxide ions as markers for oxide particles, it is also desirable to find a marker ion for these enrichments that are observed in a number of datasets, so their properties can be measured.

Figure 4.3 shows representative ion distributions of the character of the planar interfaces. It is of note that titanium (top row of Figure 4.3) in enriched at the interface at all irradiation temperatures and is thusly a reliable marker to indicate the location of the interface for comparison of enrichment of other ion species.

To investigate the distribution of oxide particles along these interfaces, the middle row of Figure 4.3 shows the titanium oxide distributions. At low temperatures, the titanium oxide is strongly enriched at these interfaces, and is evenly distributed across the surface.

However, at higher temperatures, although a number of titanium oxide clusters lie on the interfaces, the ions are consolidated into clusters, similar to those clusters found in the grain bulk. Furthermore the titanium oxide is not enriched at the interface in between the aforementioned clusters. The control material emulates the high temperatures samples again in this case. The control material maintains titanium oxide clusters distributed across the interfaces, with little to no enrichment at the interface between the clusters. At low temperatures, chromium is not enriched at the planar interfaces as shown in the bottom row of Figure 4.3. At high irradiation temperatures, chromium is enriched at the interfaces, to a similar degree to the enrichment observed in the control material.

Various other solutes, contaminates, additives and alloying elements can be found at the interfaces, but there is no obvious trending among them as a function of irradiation temperature. It is expected that these differences in interfacial enrichment may be due to local composition variations that are well documented in MA957 and other ODS alloys.

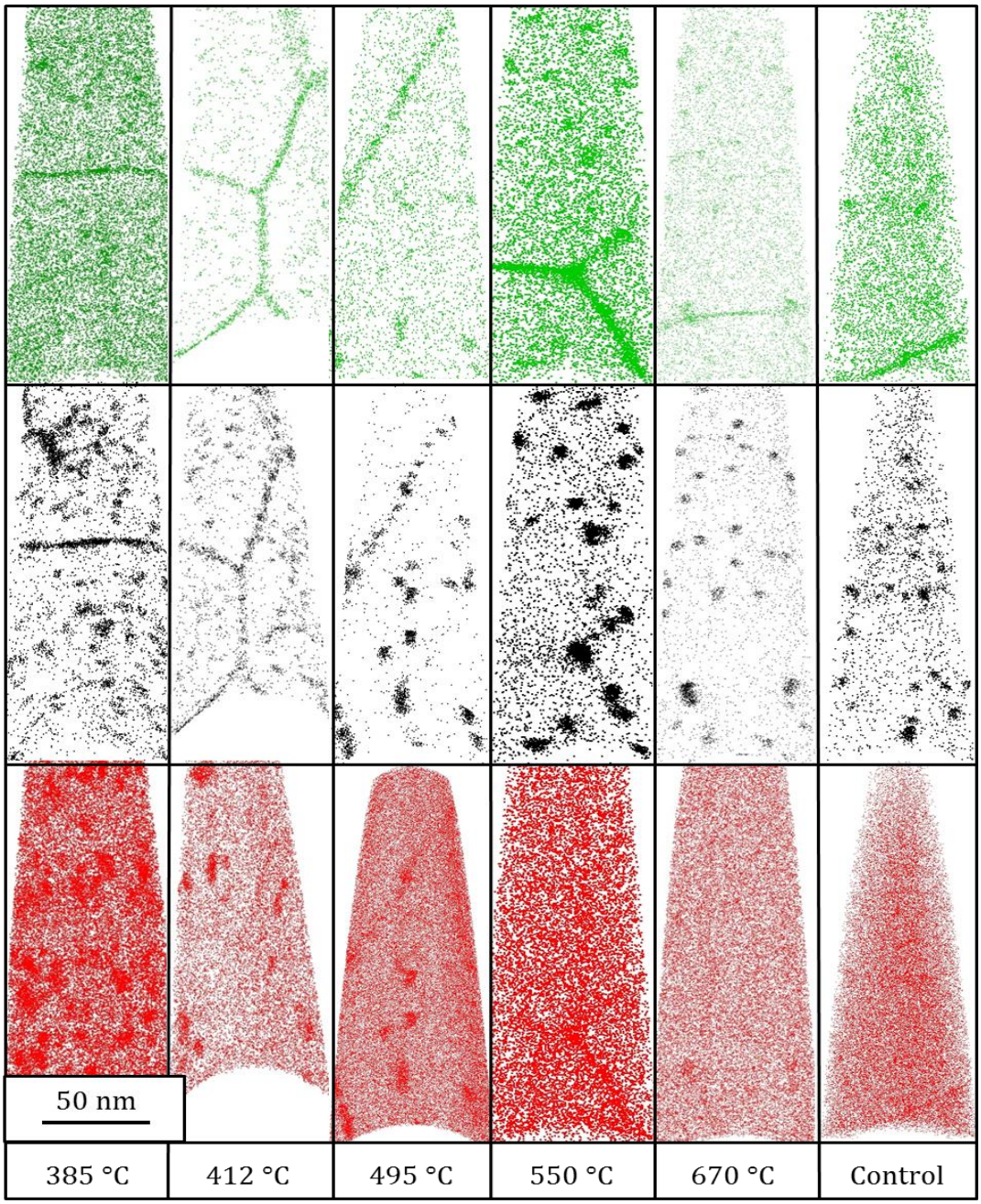

Figure 4.3 Planar enrichments of solutes observed at each irradiation condition. The top row (in green) is titanium ions, the middle row (in black) is titanium oxide molecular ions and the bottom row (in red) is Cr ions. Note that the varying ion densities in this case do not indicate a compositional variation. These images were generated by slicing the APT reconstructions in such a way that the features at the interface were most pronounced, for visual aid.

Secondary phase formation

Figure 4.4 shows chromium ion distributions as a function of irradiation temperature. At all irradiation temperatures some degree of chromium enrichment is visible.

However, when viewed simultaneously with the titanium oxide ion distributions (indicating the location of oxide particles), Figure 4.5, some interesting patterns emerge.

At high temperatures (>495 °C) chromium is enriched in association with the oxide particles. The degree of enrichment of chromium at the oxide particles is similar to the enrichment of chromium noted on the grain boundaries at high temperatures in the previous section. This suggests that rather than indicating distinct phases, the chromium enrichments at high temperatures indicate the chromium tends to enrich interfaces, including both precipitate interfaces and grain boundaries.

At low irradiation temperatures on the other hand, it seems that chromium no longer enriches on the oxide particle interface (and neither does it enrich on the grain boundaries

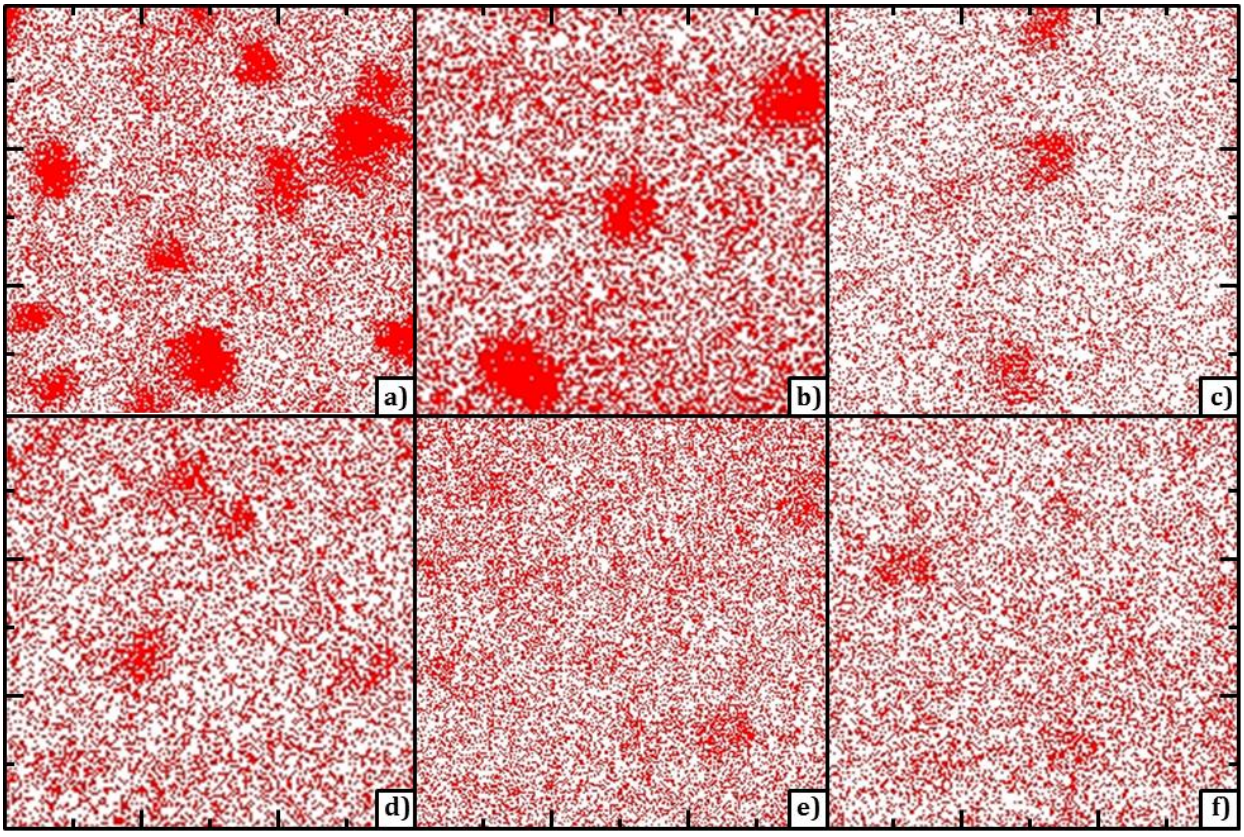

Figure 4.4 Chromium ion distribution as a function of irradiation temperature. Each section is a square region is a slice (30 nm x 30 nm x ~2 nm) taken from a representative area of the reconstruction. The number of chromium enrichments in each section is not necessarily indicative of the chromium enrichment densities overall, but rather are intended to illustrate the clustering character of the chromium ions. a) 43 dpa - 385 °C b) 109 dpa - 412 °C c) 48 dpa - 495 °C d) 113 dpa - 550 °C e) 110 dpa - 670 °C f) Control.

at low temperature). Rather the chromium enrichments form in between oxide particles. The enrichment is also significantly higher density than the higher temperature examples.

Furthermore, some low temperature chromium enrichments form complex shapes, seemingly to avoid contacting the oxide clusters. Several examples of these complex geometries are shown in Figure 4.6.

Observed rarely, and exclusively in the TX series samples, are segregations of Si, Ni and Ti (Figure 4.7). These segregations are typically, but not exclusively, associated with oxide clusters.

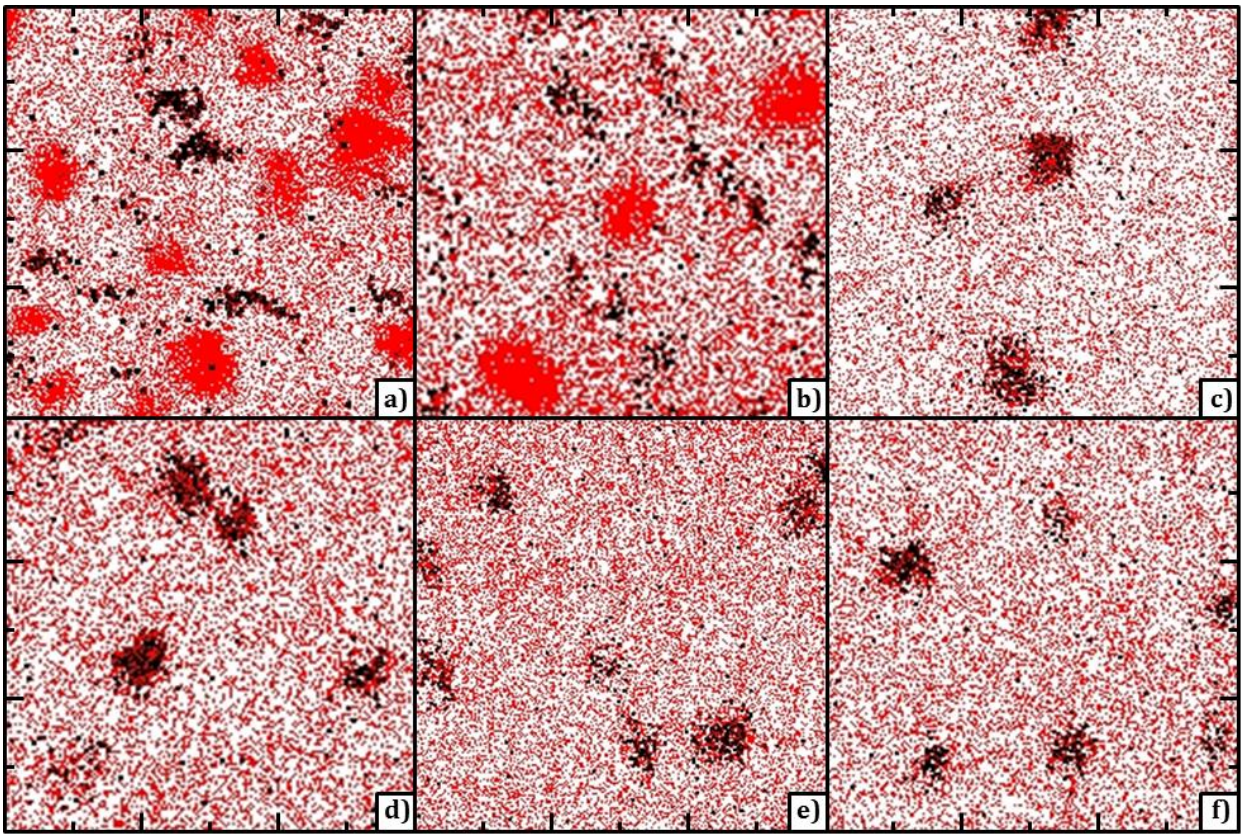

Figure 4.5 Chromium ion distribution (red) and titanium oxide ion distribution (black) as a function of irradiation temperature. Each section is a square region is a slice (30 nm x 30 nm x ~2 nm) taken from a representative area of the reconstruction. Neither the number of chromium enrichments nor the number of titanium oxide clusters in each section are necessarily indicative of the overall densities, but rather are intended to illustrate the clustering character of the chromium ions and the correlation with the titanium oxide clusters. a) 43 dpa - 385 °C b) 109 dpa - 412 °C c) 48 dpa - 495 °C d) 113 dpa - 550 °C e) 110 dpa - 670 °C f) Control.

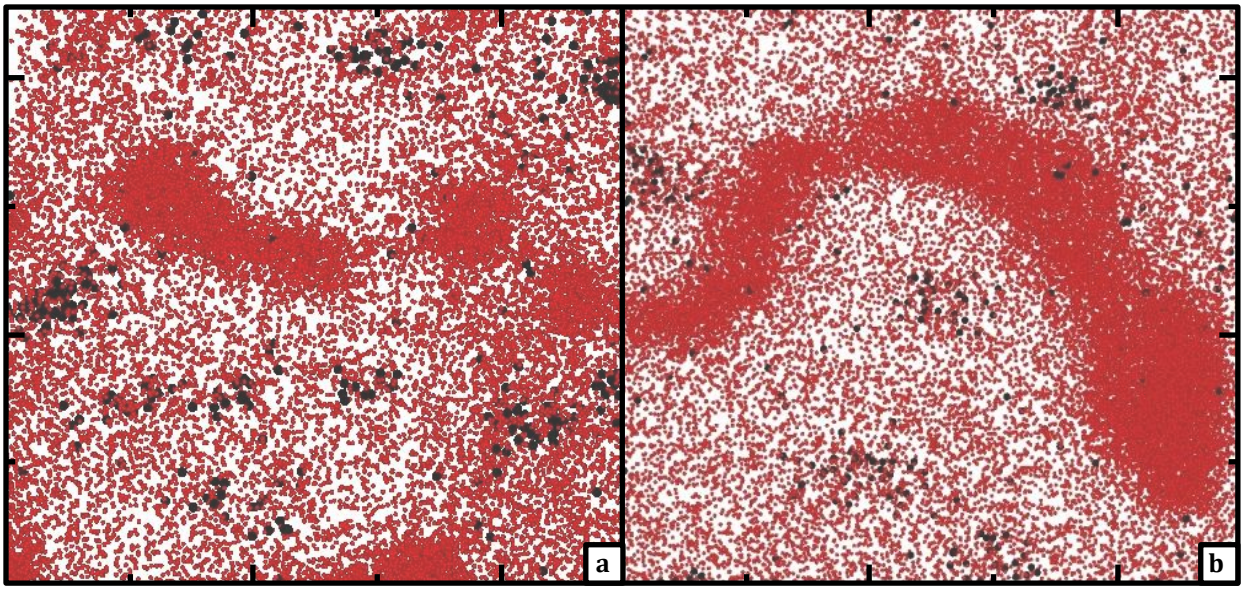

Figure 4.6 Chromium ion distributions illustrating the complex geometries formed by the chromium enrichments in low temperature irradiations. a) 385 °C b) 412 °C

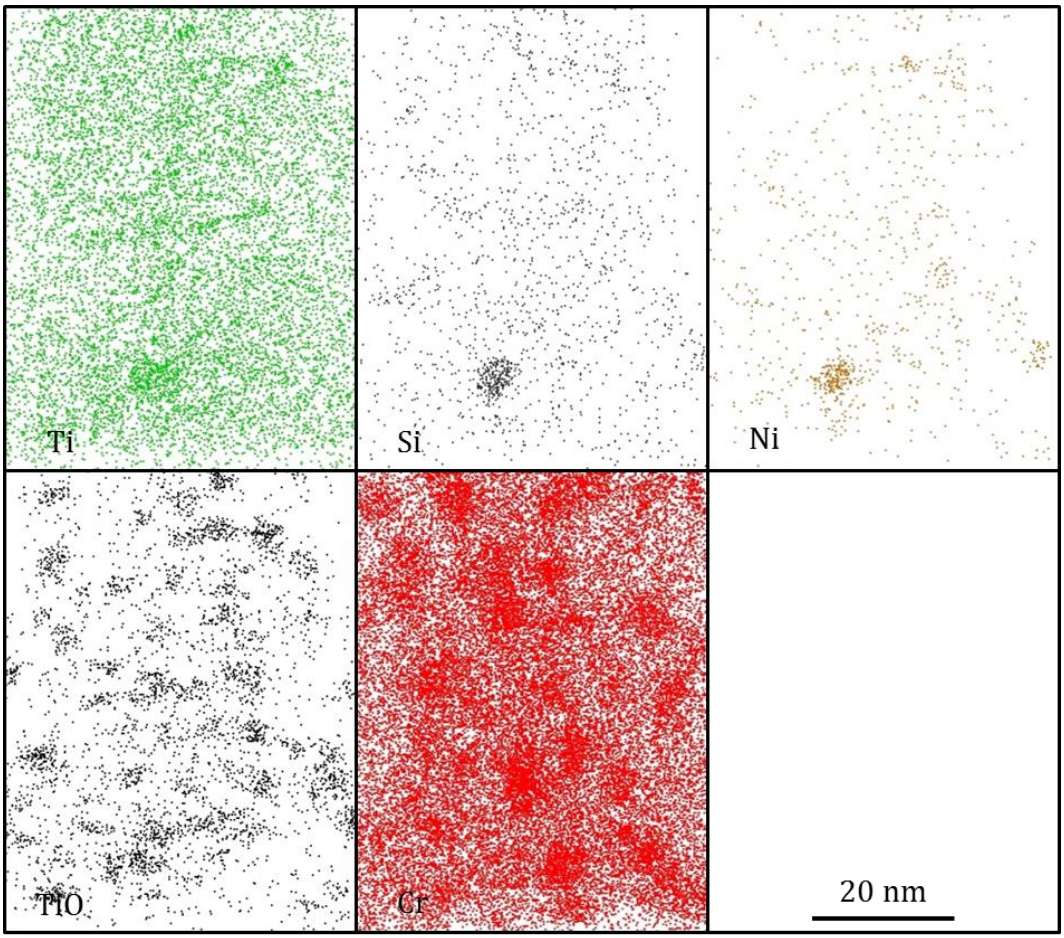

Figure 4.7 Example ion distribution of g-phase Ti-Si-Ni enrichments. These enrichments are only found in the DBB0122 heat material.

4.2 Nanoindentation

Hardness

Plotted in Figure 4.8 is the hardness measured with a Berkovich indenter as a function of irradiation condition. The low temperature sample group had substantially higher hardness values than those of the high temperature group. The high temperature sample group had similar hardness values to the control material.

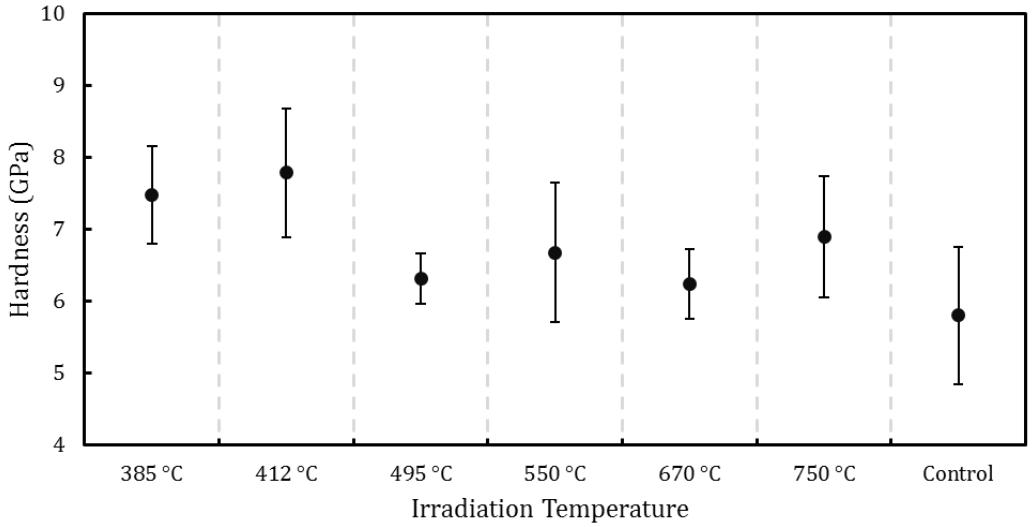

Figure 4.8 Berkovitch hardness as a function of irradiation temperature.

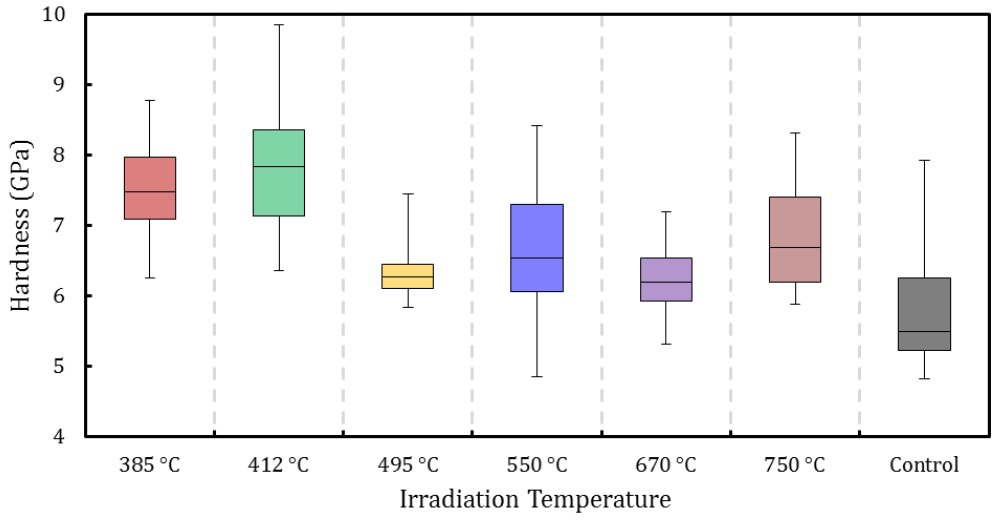

Figure 4.9 Box and whisker plots of hardness as a function of irradiation temperature.

Significant scatter is present in the hardness data, as can be seen in the box and whisker plots in Figure 4.9. This wide scatter is expected to be the result of rather coarsely polished

surfaces, compared to the indenter tip size. The surface quality was limited by the activity of the samples.

The 550 °C and 750 °C samples were substantially harder than expected, and from the other samples in the high temperature group. These samples in particular had very rough polish, which is expected to have caused surface hardening of the material.

Reduced Modulus

Evident from the plot shown in Figure 4.10, no significant change in the reduced modulus was noted as a function of irradiation condition.

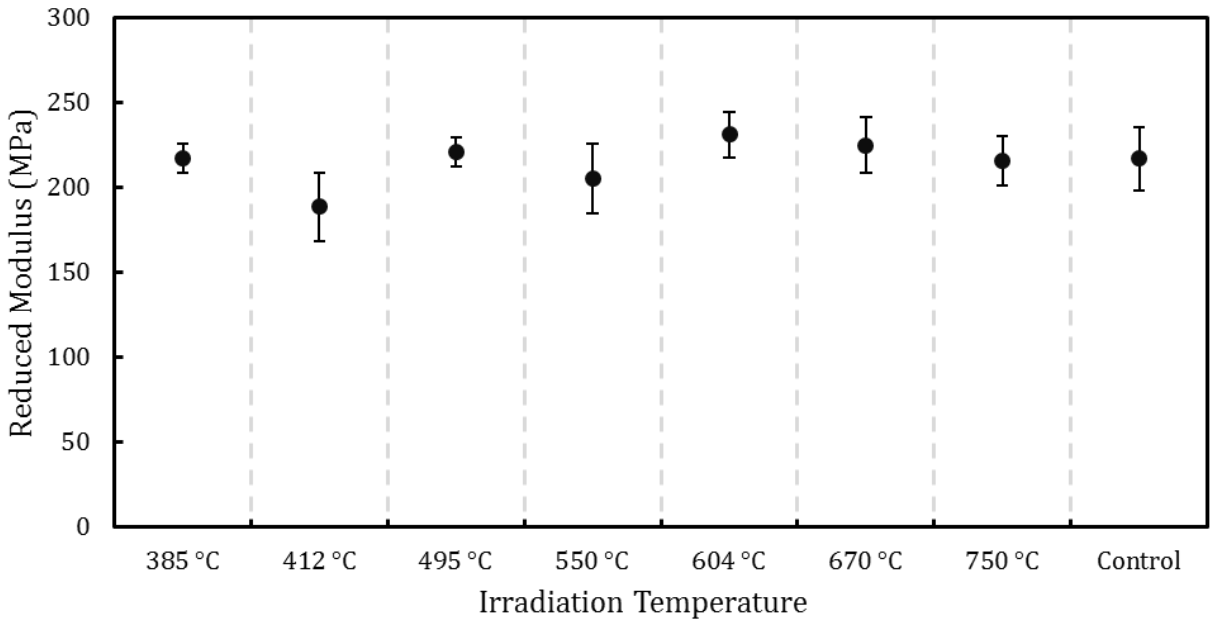

Figure 4.10 Reduced modulus as a function of irradiation temperature.

5 Discussion

5.1 Data Analysis

Method description

As described in Section 3, cluster analysis will be used to investigate the properties of the oxide clusters in the APT data. Parameter selection will make use of the plateau in parameter space which is depicted in Figure 3.18. However, this work will expand upon the idea laid out by other researchers. The particular algorithm that is used for a cluster search will change the way cluster analysis interprets the similarity of features. Nearest neighbor approaches are the most common, and are appropriate for APT application. Most APT researchers use the maximum separation method. The user must be careful to select an

algorithm that is not sensitive to aberrations in that particular dataset. What must be chosen, then, is an algorithm that performs satisfactorily in a broad range of APT datasets. The type of dataset that the algorithm should be used with can then be defined, and users can quickly identify whether their data meets that criteria.

The algorithm chosen to examine these datasets is the density-based spatial clustering of applications with noise (DBSCAN). This algorithm has been used previously to analyze clustered APT data [93]. While the cluster analysis algorithm used by IVAS is proprietary and not particularly well documented, through trial and error, it appears functionally similar to DBSCAN, though does not give the same results given the same input.

In DBSCAN, there are two parameters that describe the clustering results, the solute link distance (d_{max}) and the order. The order is the number of solutes that are required to be within d_{max} of the solute in question for it to be added to the cluster (the combination of the link distance and the order put a density constraint on the solutes in the cluster). DBSCAN is used broadly in science and in data analysis. It is powerful as it can identify clusters of arbitrary shape/size. However, it is sensitive to changing density across clusters and between clusters.

Picking the proper algorithm is fundamental to using cluster analysis. However, the method in which the algorithm is used is equally important for comparability of results. Existing methods for parameter selection were found to be inadequate to describe the ODS alloys systems found in this work. In order to systematically assess the datasets, a method of establishing cluster search parameters was developed.

After determining the location of the plateau in parameter space, the reliability of comparable cluster analysis between authors is possible by simply selecting any of the parameter sets that lie within the plateau. However, this leaves something to be desired, as again subjectivity of parameter selection becomes a necessary step in the analysis process. A method to objectively define the boundaries of the plateau should be taken. In [98], an objective function is defined as

$$(N_{rand} - N_{real})/N_{real}$$

This objective function is quite similar to the subtraction of the homogenized number of clusters from the clusters found in the test data in Figure 3.18. However, this objective function makes use of the maximum separation methods, which has some fundamental difference to the DBSCAN algorithm. First, although the maximum separation method has two input parameters, only one of the two parameters actually affects the cluster search itself: d_{max}. The maximum separation algorithm finds all the solutes that are linked by d_{max}, and groups them into clusters. Then, if the number of solutes in a cluster is less than N_{min}, the second parameter of the maximum separation method, those clusters are removed from the cluster set.

In DBSCAN, both d_{max} and order have a direct influence on the nature of the clusters found in the cluster search, since both parameters are used to evaluate each solute's inclusion in the cluster. DBSCAN is also much less prone to the single-link-effect, which is a common failure of nearest neighbor clustering algorithms. The single-link effect is the grouping of

two or more adjacent clusters together by a string of nearby atoms. By the restrictions on the number of nearest neighbors a clustered atom must have, DBSCAN significantly reduces the possibility of clusters being artificially merged in this way.

Still, having selected an improved cluster analysis algorithm, the problem of where in the plateau should the parameters be selected has not been completely resolved. The approach that has been chosen by this work is to recognize that there simply is not a set of parameters that singularly captures the "correct" cluster set. No matter what parameters are chosen, the cluster search will result in the "correct" cluster set, because that set was defined by the input parameters. The idea of one cluster set being of superior importance to another is due to the type of information the user of the algorithm is trying to illuminate in the data.

In the case of APT, we are looking to understand as precisely as possible how many clusters are in a particular dataset. So, some materials science must be used to help eliminate particle types of cluster sets. Firstly, small clusters are most likely not useful. In APT data, there are a number of clusters that only contain a handful of atoms. Since the unit cell of pyrochlore (a likely candidate for the crystal structure of the very small Y-Ti-O particles) has 88 atoms/unit cell, and the APT instrument has ~37% detection efficiency, any cluster containing less than 88*0.37=32.56~33 atoms indicates that there was not enough material located in that area to even form one unit cell of pyrochlore. While it is true that such small features may have an effect on the material properties even if they do not have a full unit cell, there is clearly a lower limit to the number of atoms in a cluster that are relevant to the cluster search.

By increasing the order parameter, the minimum number of atoms in a cluster is inherently increased because in order for an atom to have ten nearest neighbors (for example), then the minimum number of atoms in that cluster is 11, the core atom, and each of its neighbors. Interestingly, the plateau in parameter space typically occurs between order of ~8-15, and therefore the occurrence of extremely small clusters (clusters of 3-5 solute ions) does not have an effect on the cluster analysis results. Furthermore, a vanishingly small fraction of the clusters actually have a size that is close to the minimum allowable; most of the small clusters have 30-40 atoms contained within them.

The other possibility that must be addressed in order to fully commit to the concept of using the plateau method, is to show that there can only be one plateau in an APT dataset. If more than one region of stability exists in a dataset, then which region is the region that contains the relevant cluster set for examining the oxide particles? Again, an appeal to materials science is necessary. This time, a volume argument will be used.

Typically, APT datasets contain on the order of hundreds of cubic nanometers of material. In some cases, this volume can contain material from several grains. However, in order for there to be a second stable region in parameter space, there would have to be a well-defined clustering of clusters. An analogy to such a clustering would be a galaxy cluster in outer space. A galaxy cluster is a group of nearby galaxies in space. A galaxy is a cluster of stars in space. So a galaxy cluster could be thought of as a cluster of clustered stars.

On the scale of APT data, the only possibility for such an occurrence is if a large number of individual grains had been captured in the APT dataset. In that case, the clusters of atoms that indicate precipitates would be clustered within the confines of the grain. However, APT datasets simply are not large enough to capture a significant volume of distinct grains, even if one is examining materials with the smallest grain structures. MA957s smallest grains have diameters ~200 nm; even an extremely large APT dataset will only be able to capture 2 or 3 grains. Therefore, the only stable region in parameter space will be the region attributed to the oxide clusters. With these two material science motivated presumptions about APT data, the plateau method will consistently locate a single stable region in parameter space, which also happens to be the area that best captures the properties of the oxide clusters.

The final step is to develop a methodology for selecting parameter sets from the plateau. The key assertion to this approach is that no single parameter set describes the data perfectly; rather, any of the parameter sets in the plateau provide an equally valid description of the dataset. Since each dataset adequately describes the system, then the cluster properties can be measured from an ensemble average of the results of cluster analyses using all the parameter sets in the plateau. Finally, a method must be established to objectively define the borders of the plateau region. In this work, the method of choice is a statistical hypothesis test known as the two-sample Kolmogorov-Smirnoff (KS) test [103] [104].

The KS test is a non-parametric statistical hypothesis technique that compares two continuous probability distributions and determines whether or not the two distributions were sampled from the same parent distribution. The KS test calculates the distance between the cumulative distribution function of one distribution to the empirical distribution function of the other distribution. By quantifying this distance, the KS test is able to compare the central tendency and the shape of two arbitrarily shaped distributions. In the case of analyzing a single APT dataset, the parent distribution is the unsampled dataset, with no cluster analysis performed. Each cluster analysis is sampled from the same parent distribution, but since there is non-random cluster of the solutes present, a number of the cluster set should be much more similar to one another. By comparing the cluster size distributions (the number of solutes per cluster) to one another, a set of cluster search parameters can be determined such that the size distribution of each resulting cluster set passes the KS test. That is to say, each resulting cluster set is sampled from the same parent population, and that parent population is dominant clustering character of that dataset.

Using simulated data provided by E. A. Marquis at the University of Michigan, illustrated in Figure 5.2, the cluster search parameter selection method was tested on data with a known number of clusters and size distribution (the parent distribution). The first step to using the plateau method is to establish where in parameter space the plateau lies, so that the proper cluster analysis input parameters can be used.

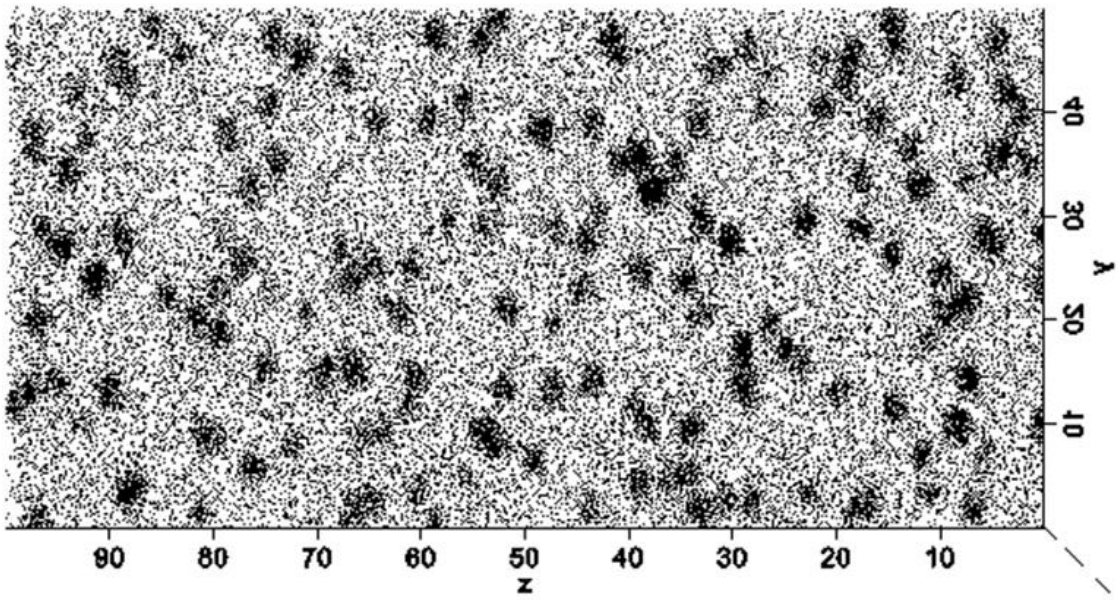

Figure 5.2 Reconstruction of simulated dataset for cluster analysis method testing.

Figure 5.1 shows a coarse scan of parameter space and illustrates the general area of the plateau.

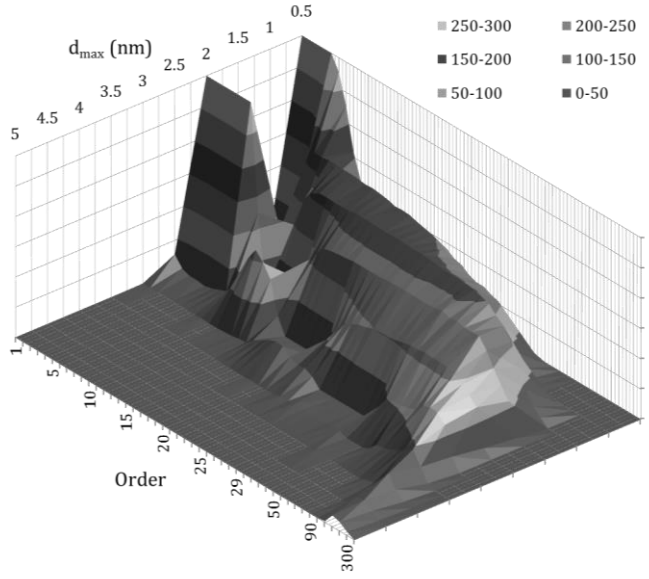

Figure 5.1 Parameter space plateau for the simulated dataset. The vertical axis is cluster count.

A higher resolution scan of parameter space will be performed to establish the boundaries of the plateau, Figure 5.3. By carefully analyzing the plateau in Figure 5.3, the boundaries

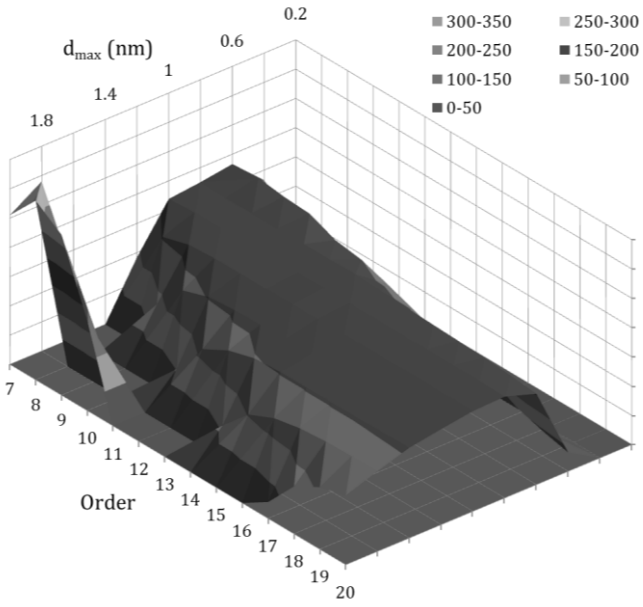

Figure 5.3 Fine scan over plateau region in parameter space.

are reduced again, and the KS test (with a significance level of 0.05) is performed on the cluster size distributions that are generated from each (d_{max}, order) pair in the plateau. The KS test is performed by first creating a reference size distribution that represents the overall size distribution of the plateau region. This is done by pooling the size distributions from all the individual pairs of d_{max} and order in the plateau. Then, each individual size distribution is compared to the pooled distribution. If the individual distribution is determined to not be sampled from the pooled distribution (according to the KS test), then that pair of input parameters are thrown out. The result of this process on the different points in the plateau is illustrated in Figure 5.4. In Figure 5.4, the points indicate the cluster analysis parameter pairs that were tested. The red points indicate parameter pairs that were removed from the analysis using the KS test, while the blue points indicate parameter pairs that passed the KS test.

Having determined the parameter pairs that are in the plateau by applying the KS test, the cluster properties of the dataset can be determined. From a total of 72 parameter pairs used to generate cluster sets, 63 passed the KS test, making up the clusters from which conclusions about the cluster properties can be drawn. The average cluster count from the 63 included parameter pairs was 171, with a standard deviation of 3. The correct number of clusters in the simulation was 175.

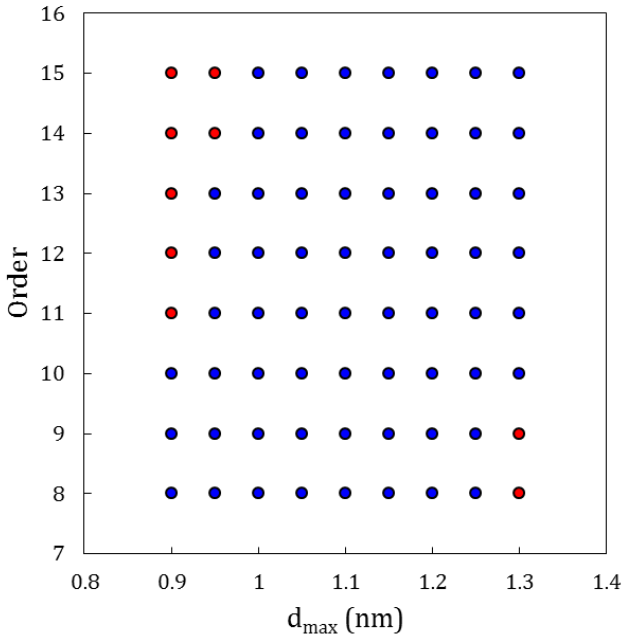

Figure 5.4 Illustration of the parameter pairs in the plateau. Blue dots indicate passed that passed the KS test, while red dots indicated pairs that failed the KS test.

Comparative histograms are shown in Figures 5.5-5.7 that illustrate the nature of the size distributions of the accepted cluster sets. These histograms are intended to show the character of the cluster sets that were drawn from the parameter space plateau. In Figure 5.5 each individual distribution is plotted with high transparency and all the accepted distributions are plotted on top of one another. This creates an image with varying degrees of light and dark. The dark areas are indicating many of the cluster size distributions overlap in that region, while the light areas indicate that clusters of that size or number are not common. To illustrate the degree to which the pooled distribution represents the individual distributions, it is plotted along with the individual size distributions in Figure 5.6. Finally, to illustrate the accuracy in size detection of the plateau method, Figure 5.7 shows the simulated size distribution plotted along with the individual size distributions. This shows that not only does the plateau method not only determines the number of clusters in the dataset accurately, it also accurately summarizes their average size, as well as the shape of the size distribution.

The modifications made to the cluster search process described in this document provide a number of advantages over current techniques. Most importantly, by pooling the results of a number of cluster analyses, an approximate uncertainty in the number of clusters identified can be calculated. By using the cluster set from a single parameter pair, there is no clear tool for defining the certainty in the number of identified clusters. Furthermore, the pooling of cluster sets allows cluster size and composition measurements to be collected from a much larger number of clusters, providing a better estimate of the size and composition of the found clusters.

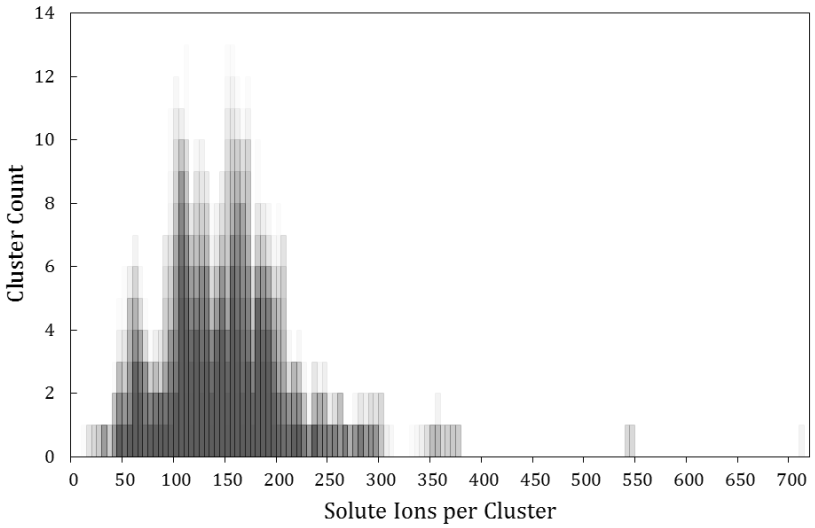

Figure 5.5 Cluster size histogram for the individual cluster sets. Each set is plotted transparently and overlaid, so the darker areas indicate where more cluster sets have clusters of the same size, and the lighter areas indicate cluster sizes or numbers that are less common.

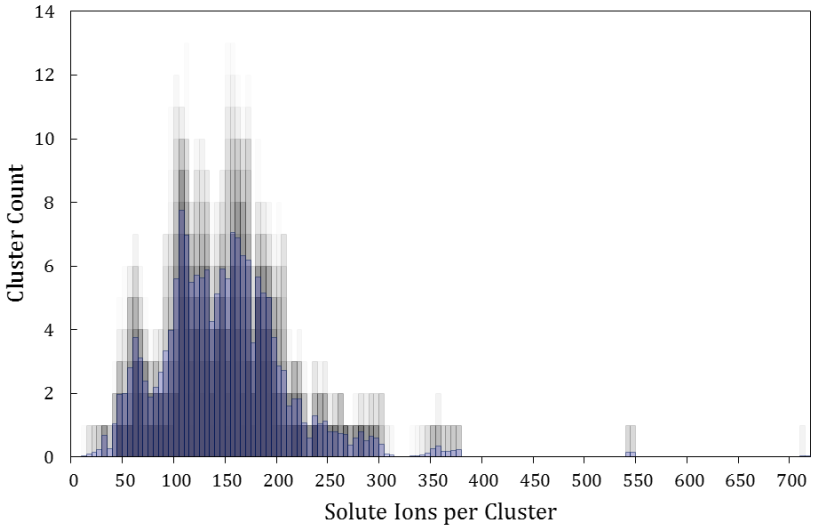

Figure 5.6 Cluster size histogram for the individual cluster sets (grey). Each set is plotted transparently and overlaid, so the darker areas indicate where more cluster sets have clusters of the same size, and the lighter areas indicate cluster sizes or numbers that are less common. Plotted over the top in blue is the pooled cluster size distribution, scaled to the individual size distributions by dividing by the number of included cluster sets. This is equivalent to showing the average number of clusters in each bin.

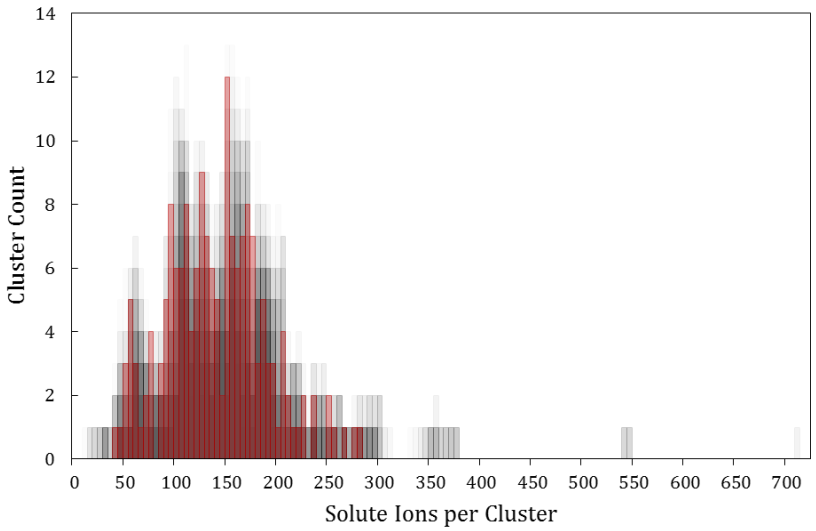

Figure 5.7 Cluster size histogram for the individual cluster sets (grey). Each set is plotted transparently and overlaid, so the darker areas indicate where more cluster sets have clusters of the same size, and the lighter areas indicate cluster sizes or numbers that are less common. Plotted over the top in red is the actual size distribution of the simulated clusters, showing that the plateau method results in not only an accurate number of identified clusters, but also the shapes of those cluster size distributions are accurate to the underlying data.

5.2 Atom probe tomography

Oxide cluster properties

Using the aforementioned cluster analysis methodology, all of the APT datasets were analyzed. Figure 5.8 shows the trend of average oxide cluster number density as a function of irradiation temperature, while Figure 5.10 shows box and whisker plots, illustrating the distribution of cluster number densities across the sample datasets for each temperature. Box and whisker plots illustrate the central tendency and extent of a distribution. The whiskers extend from the minimum observed value to the maximum, while the bottom of the box marks the 25th percentile, the line across the mid-section of the box is the median (50th percentile) and the tip of the box marks the 75th percentile. As was evident from the ion distributions in the results section, the cluster number density increases with decreased irradiation temperature. A sharp increase in cluster number density occurs at 412 °C. The oxide cluster number density saturates, no clear difference in number density

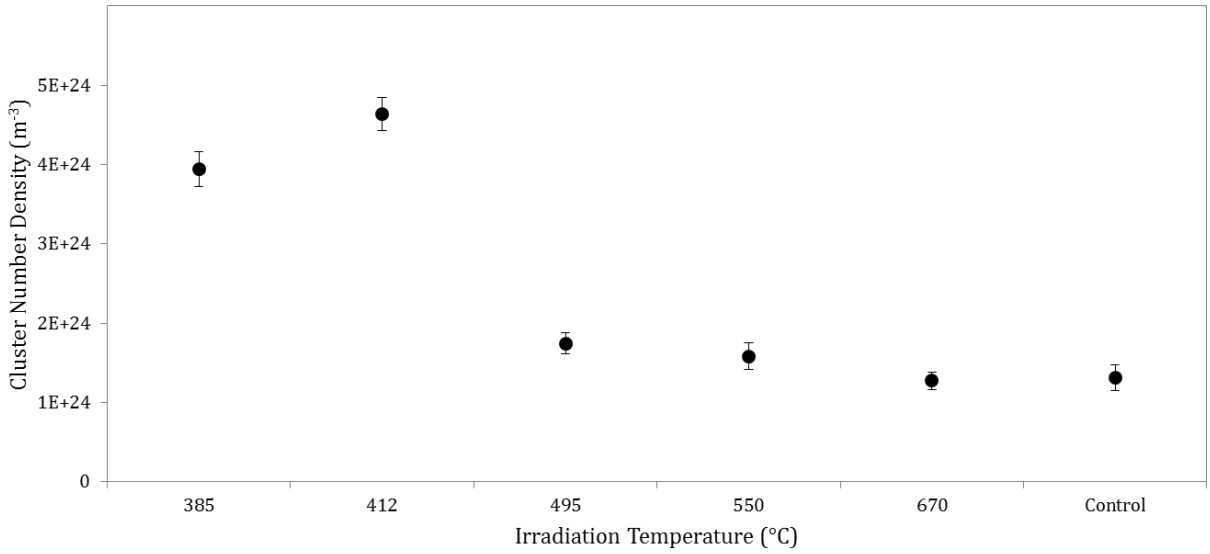

Figure 5.8 Average cluster number density as a function of irradiation temperature, with estimated standard error.

can be seen between 412 °C and 385 °C. This trend is in support of the hypothesis, that ballistically dissolved particles are being prevented from reforming at lower irradiation temperatures.

At higher irradiation temperatures, the cluster number density is very similar to that of the control material. This is explained by the higher kinetics offered by the higher temperature environment, leading to an increased reformation ability. However, as the temperature is dropped below 495 °C, the kinetics of the steady state limit the ability of the oxide clusters to reform after dissolution, resulting in a high density of particles when single clusters are broken in several smaller clusters.

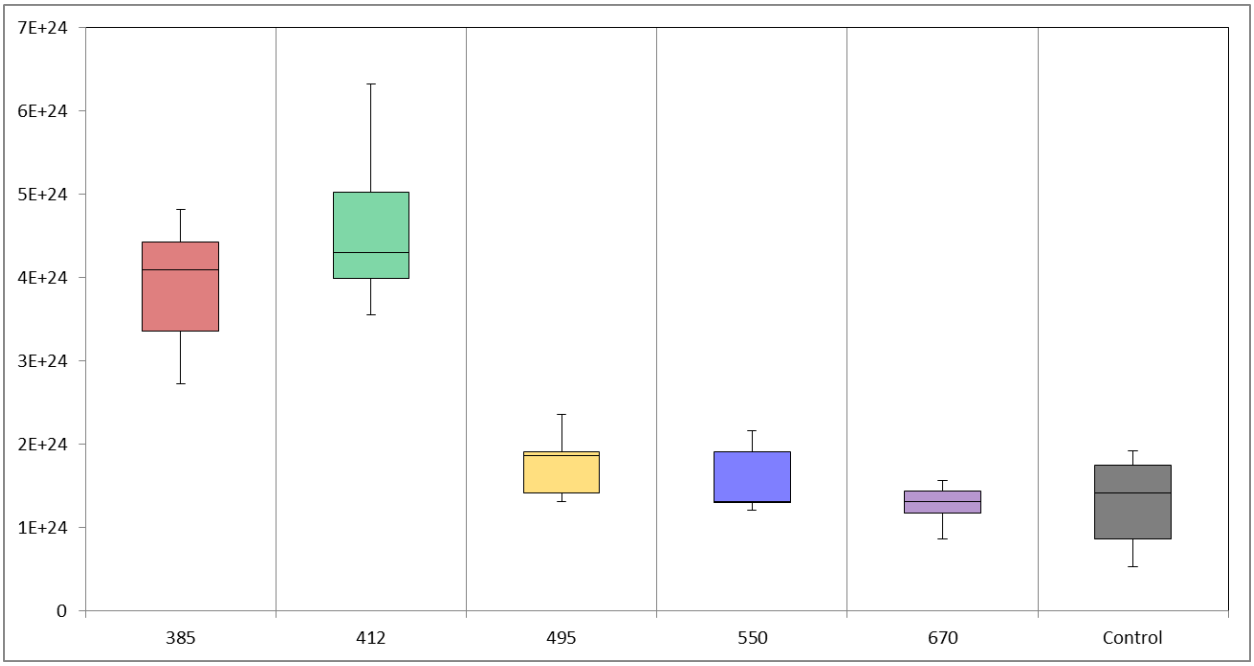

Figure 5.10 Box and whisker plots illustrating the distribution of cluster number densities across the different datasets for each irradiation condition.

Classically, the size of clusters found in APT datasets has been reported in terms of the Guinier radius. Figure 5.9 shows the average Guinier radius of clusters as a function of irradiation temperature. Although, a slight decreasing trend can be seen in the Guinier radius as the irradiation temperature is reduced, it is not obvious that any change in particle size is significant. So, while the expected trend, of decreased cluster size as temperature is reduced is followed, the magnitude of the size reduction is questionable.

To further explore this trend, shown in Figure 5.11 are box and whisker plots of the cluster

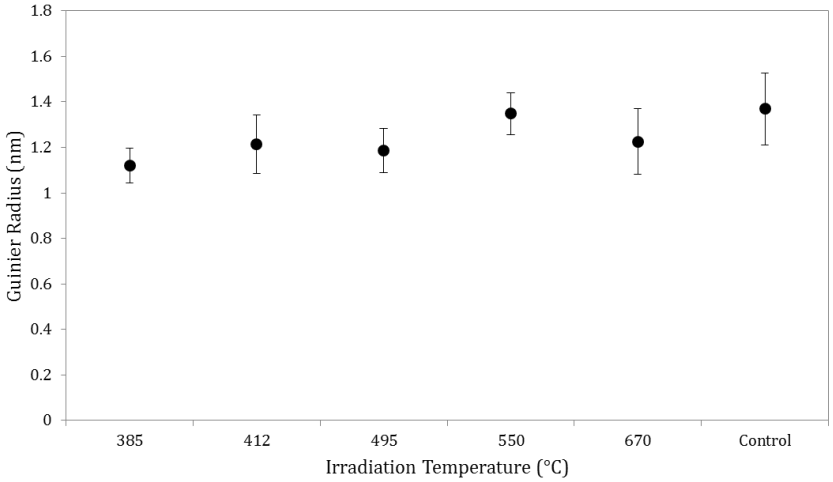

Figure 5.9 Average Guinier radius of clusters as a function of irradiation temperature. Standard errors are reported: i.e. The standard error is the standard deviation in the averages of the Guinier radius for each APT dataset.

size distributions as a function of irradiation temperature. These plots do little to

illuminate the changes in size, as their central tendencies are similar across temperature. In Figure 5.12 cluster size distributions as a function of irradiation temperature as shown. Each of these distributions is relatively normal, and the normality of the distribution increases as the irradiation temperature is reduced. This follows with expectation, as since ballistic dissolution is a random process, that the resulting oxide particle's size should be approximately normally distributed. That is to say, that the more the reformation process is impeded, the more the cluster size distributions should normalize.

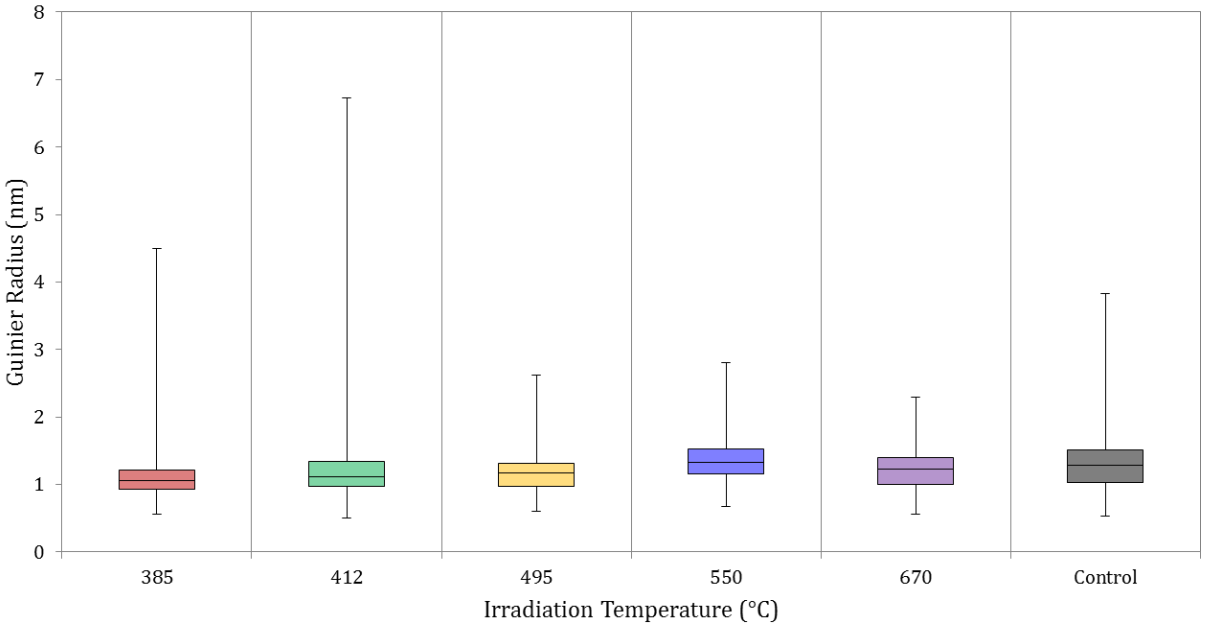

Figure 5.11 Box and whisker plot illustrating the distribution of cluster Guinier radii across the different datasets for each irradiation condition.

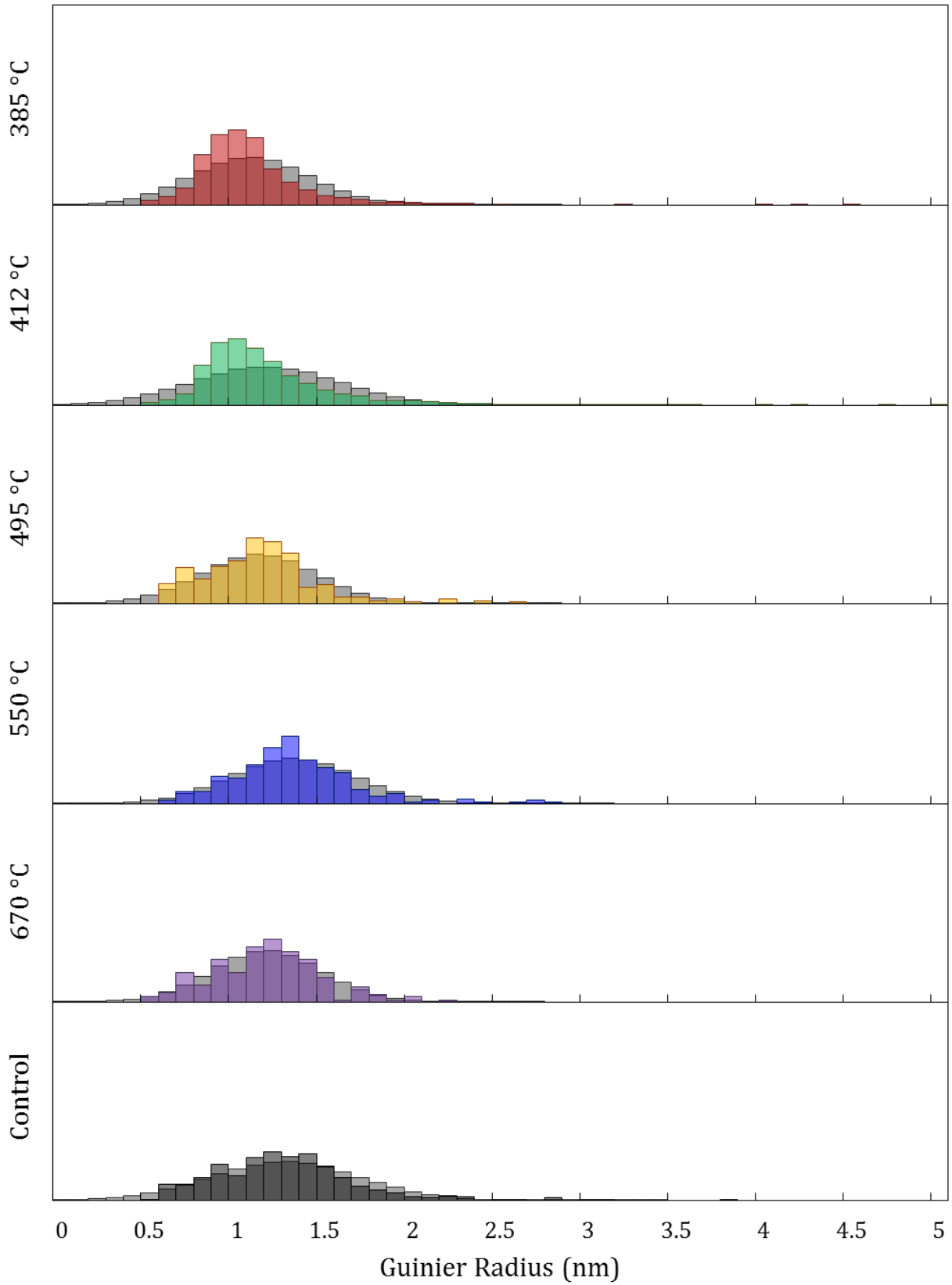

Figure 5.12 Guinier radius size distributions across irradiation temperature. The heights of the columns are relative and scaled to each other. The light grey distribution indicates the shape of a normal distribution with equivalent mean and standard deviation.

The origin of these slight changes in size is due to an aberration in APT that effects composite systems such as ODS alloys. This is known as cross over aberration. Cross over aberration occurs when the two portions of a composite material are both on the surface of the tip. If the two materials have different evaporation fields, then the material with the lower field will preferentially evaporate, leaving a pock-mark in the surface of the tip. This tip shape nonuniformity then causes a change in the local electric field, which changes the evaporation characteristics of the tip.

Furthermore, ions are modeled in the reconstruction as evaporating perpendicular to the specimen surface. When the tip shape is not hemispherical, this leads to uncertainties is the origin location of ions counts from that region. It also results in the magnification of the local atomic density near the precipitate. Cross-over aberration is responsible for significant loss of information about the precipitate in a quite complicated manner, making estimations about the effects this aberration has on the produced data difficult.

One aspect of the precipitate that is lost is the shape. By comparing images of particles of similar size in both APT and in HRTEM, shown in Figure 3.8, it is clear, that in HRTEM, the particles are cuboidal, while in APT they are round or elliptical. This is evidence that the APT technique can locally lose resolution when materials of different evaporation fields are evaporated together. Bearing this aberration in mind, a new metric for cluster size needs to be developed that is less sensitive to this problem.

Since each atom has a known volume which can be approximated, then each cluster can be ascribed a volume by counting all the ions within it. That ion count is then proportional to the cube of the cluster "radius". While this radius is not a physical value, neither is the Guinier radius, due to the unknown resolution loss which is illustrated by the shape loss, so we are not losing any information by this metric conversion. Despite it being an analysis

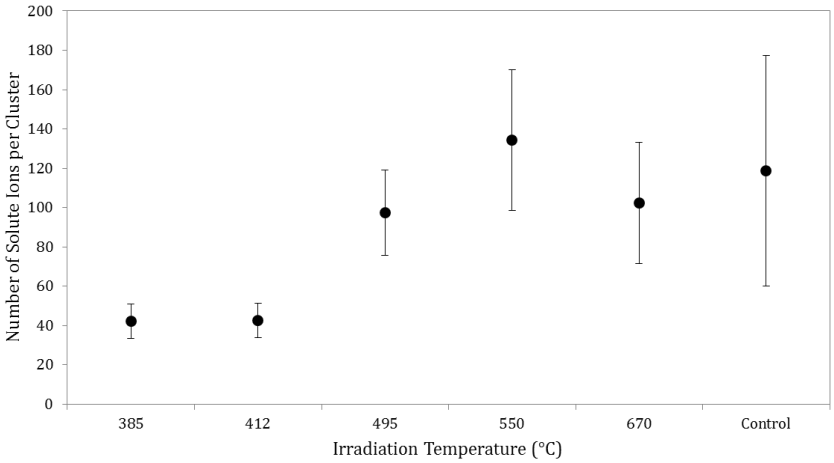

Figure 5.13 Cluster size in terms of solute ion count per cluster as a function of irradiation temperature. Errors reported are standard error. The standard error is the standard deviation in the averages of the solute ion count per cluster for each APT dataset.

parameter, rather than a physical measurement, this size metric is much less sensitive to this aberration and therefore can provide clearer insight into the particle size change as a function of irradiation temperature.

Plotted in Figure 5.13 is the average cluster solute ion count as a function of irradiation condition. Figure 5.13 clearly shows a sharp decrease in average cluster size at 412 °C. As before, a clearer picture of the change in cluster size by viewing the full cluster size distribution.

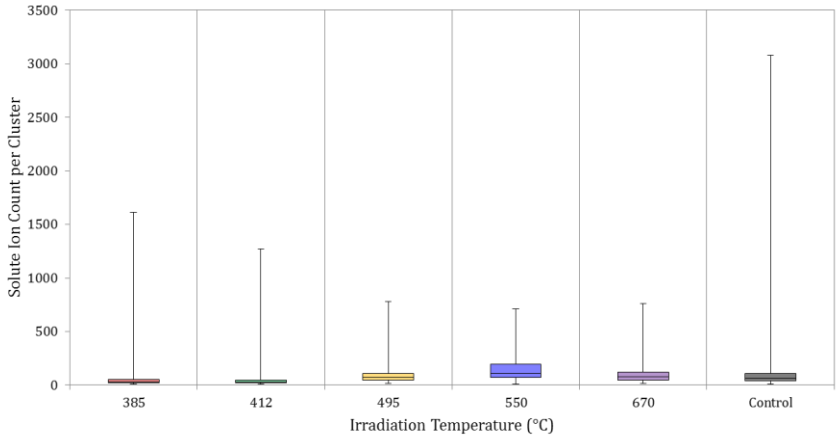

Figure 5.14 Box and whisker plot of cluster size in terms of solute ion count per cluster as a function of irradiation temperature. This overall plot is intended to indicate the presence of a low density of large clusters.

Figure 5.14 depicts the box and whisker plot of the oxide cluster size distributions as a function of irradiation temperature. Since there is such a broad range of sizes in Figure 5.14, the box and whisker plots are shown again in Figure 5.15 with the 75th percentile to the maximum omitted. A similar trend to the average values is seen in the box and whisker plots, that there is a sharp reduction in cluster size below 412 °C.

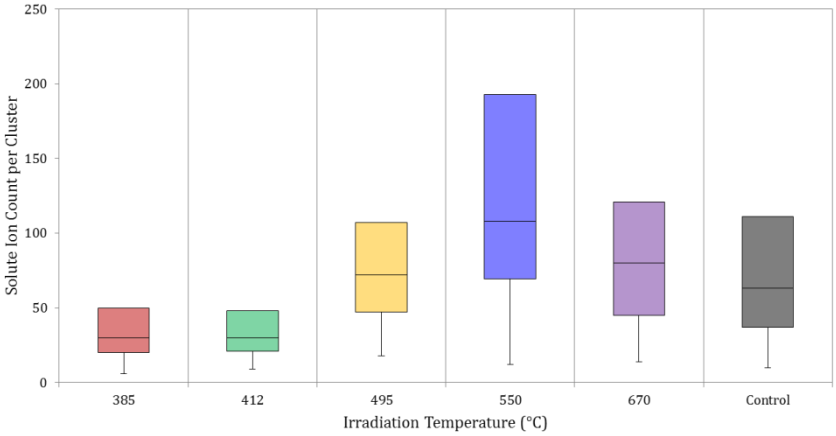

Figure 5.15 To better illustrate the central tendency of the cluster size box and whisker plots for the cluster size in terms of solute ions per cluster as a function of irradiation temperature, the fourth quartile (illustrating clusters with sizes greater than the 75% percentile) was removed from the plot.

Figure 5.16 shows the size distributions of oxide clusters as a function of irradiation temperature. While the higher temperature samples have a broad evenly distributed size distribution, the 412 °C and 385 °C samples are sharply peaked toward the very small cluster sizes. This is clear evidence in support of the hypothesis that the decreased

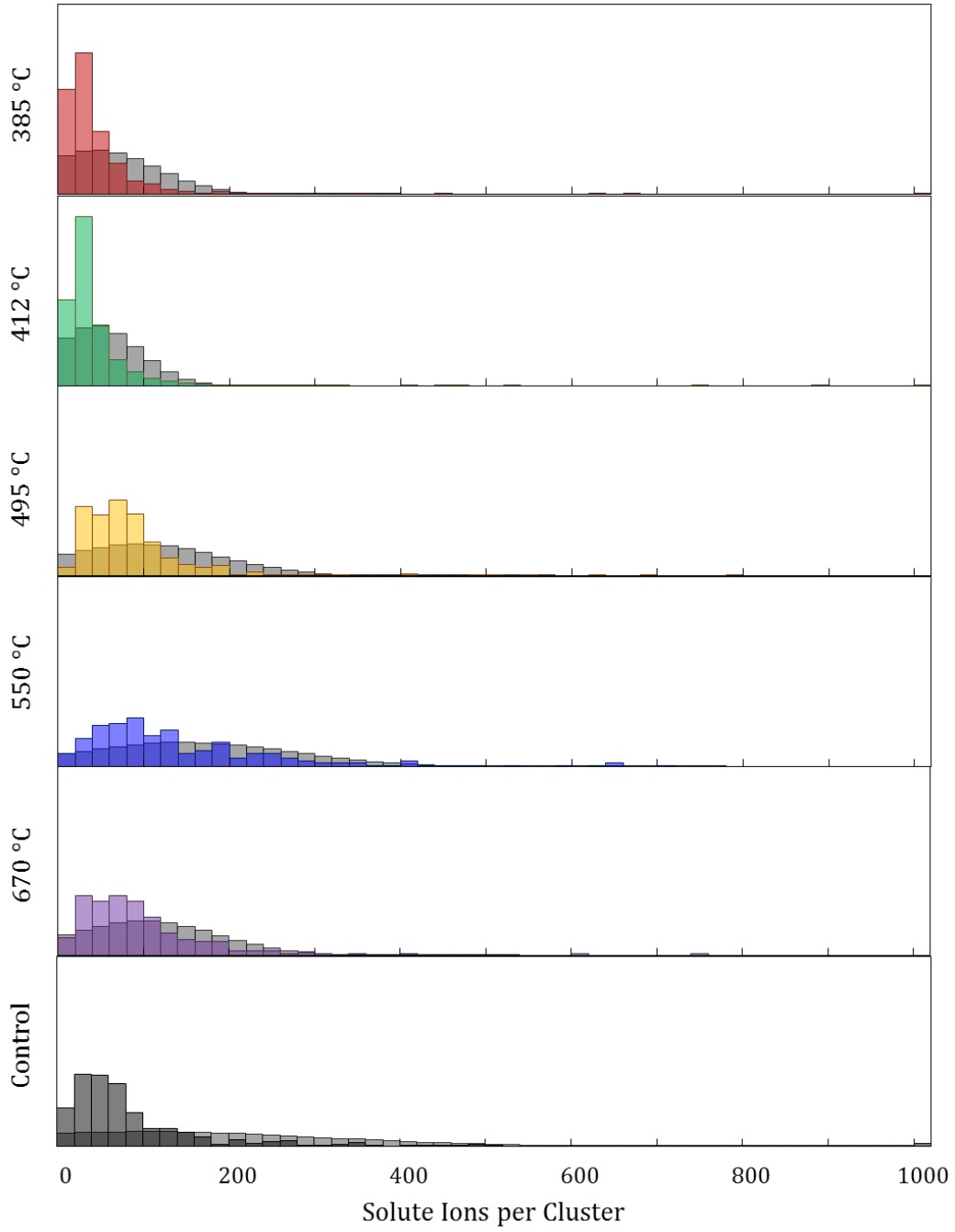

Figure 5.16 Size distributions, in terms of solute ions per cluster, across irradiation temperature. The heights of the columns are relative and scaled to each other. The light grey distribution indicates the shape of a normal distribution with equivalent mean and standard deviation.

irradiation temperature inhibits the ballistically dissolved particles from reforming.

Cluster compositions are shown in Figure 5.17-5.22. These plots are multivariate, where cluster radius is indicated by the radius of the transparent circle and composition is indicated by the circle's position on the ternary diagram. Across all irradiation temperatures, the compositions are scattered around the same central composition, about 50% titanium, 10% yttrium and 40% oxygen. Furthermore, there is little to no change, aside from statistical scatter, in composition as a function of cluster size.

It is important to point out that although this compositional measurement agrees with other APT papers on MA957, it does not align well with the stoichiometry predicted by crystallographic investigation using HRTEM. While there is still some debate evident in the literature on crystallographic analysis of MA957, the two major candidate phases are $Y_2Ti_2O_7$, and YTi_2O_5. The location of these candidate phases is also shown on the compositional plots to illustrate the substantial deviation from expectation measured by APT.

The compositional data is also supportive of the ballistic dissolution and limited reformation hypothesis, since the particles seem more or less randomly distributed around the average composition. However, evidenced by the large disagreement between HRTEM studies and APT as well as the known systematic errors in APT with the tracking and counting of O and Y, the compositional measurements are not definitive proof of ballistic dissolution. Nonetheless, the mentioned aberration are expected to be comparable for particles of approximately the same size, regardless of irradiation condition, making size for size compositional comparisons possible.

Since there is no change in composition as a function of size, it is expected that composition is comparable across both size and irradiation condition.

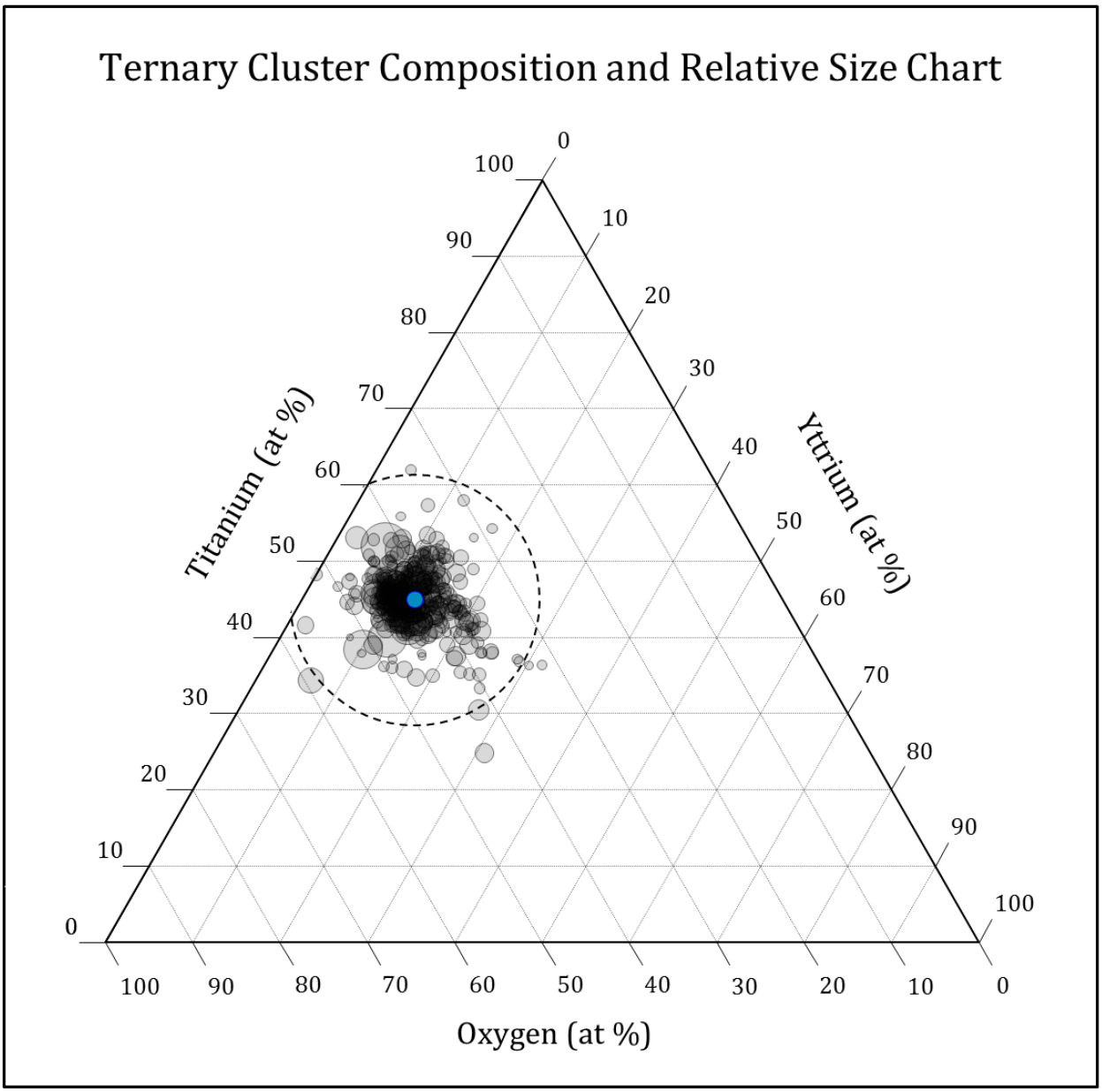

Figure 5.17 Multivariate diagram showing the compositions of the Y-Ti-O clusters in the EV control dataset under the assumption that only Y, Ti, and O atoms contribute to the composition of the particles. Each circle represents a single cluster, with the radius of the circle representing the Guinier radius of the particle, relative to the large dashed circle which has a 20 nm radius. The blue circle is located on the average composition and is shown with the average Guinier radius.

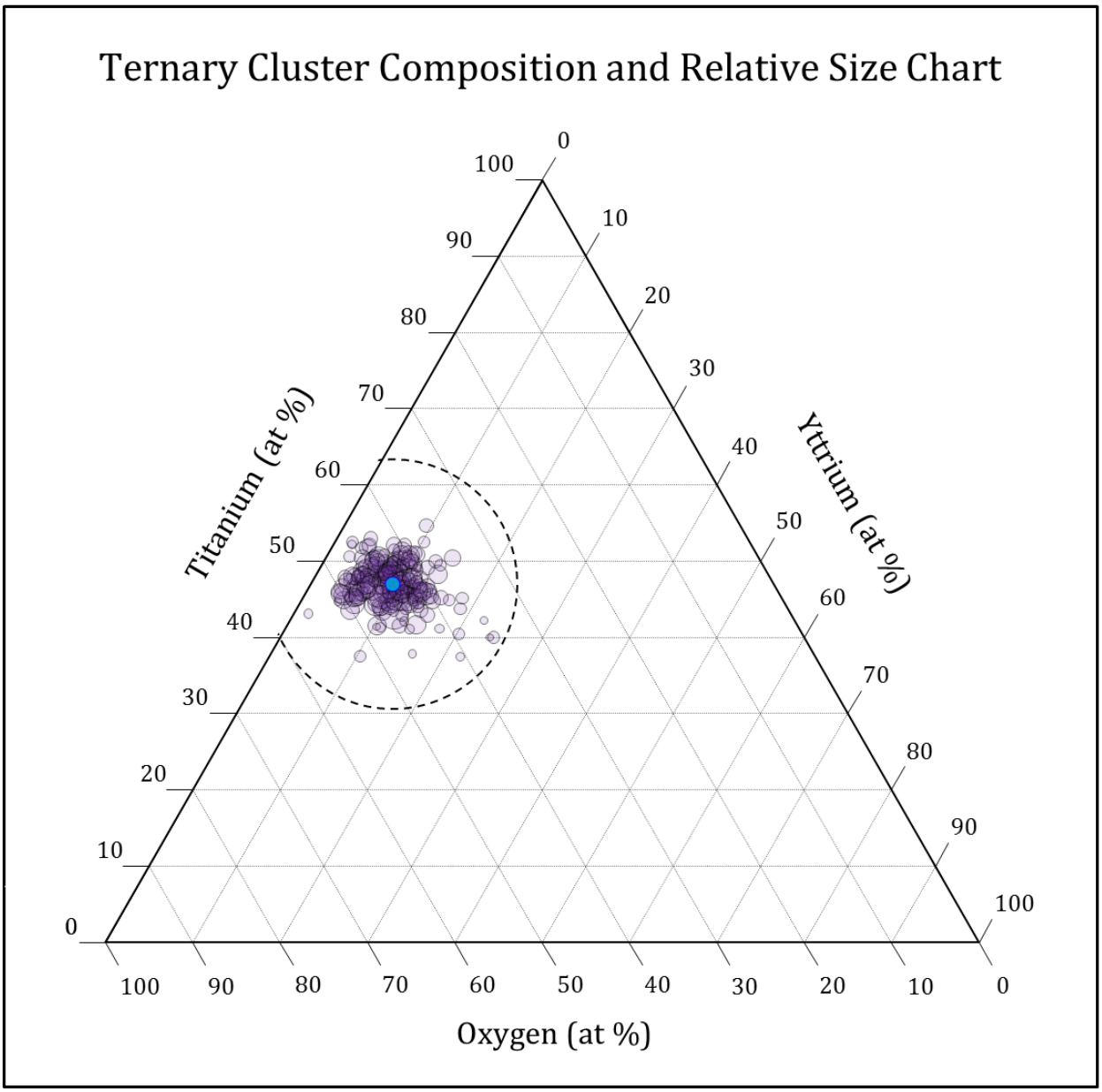

Figure 5.18 Multivariate diagram showing the compositions of the Y-Ti-O clusters in the 670 °C dataset under the assumption that only Y, Ti, and O atoms contribute to the composition of the particles. Each circle represents a single cluster, with the radius of the circle representing the Guinier radius of the particle, relative to the large dashed circle which has a 20 nm radius. The blue circle is located on the average composition and is shown with the average Guinier radius.

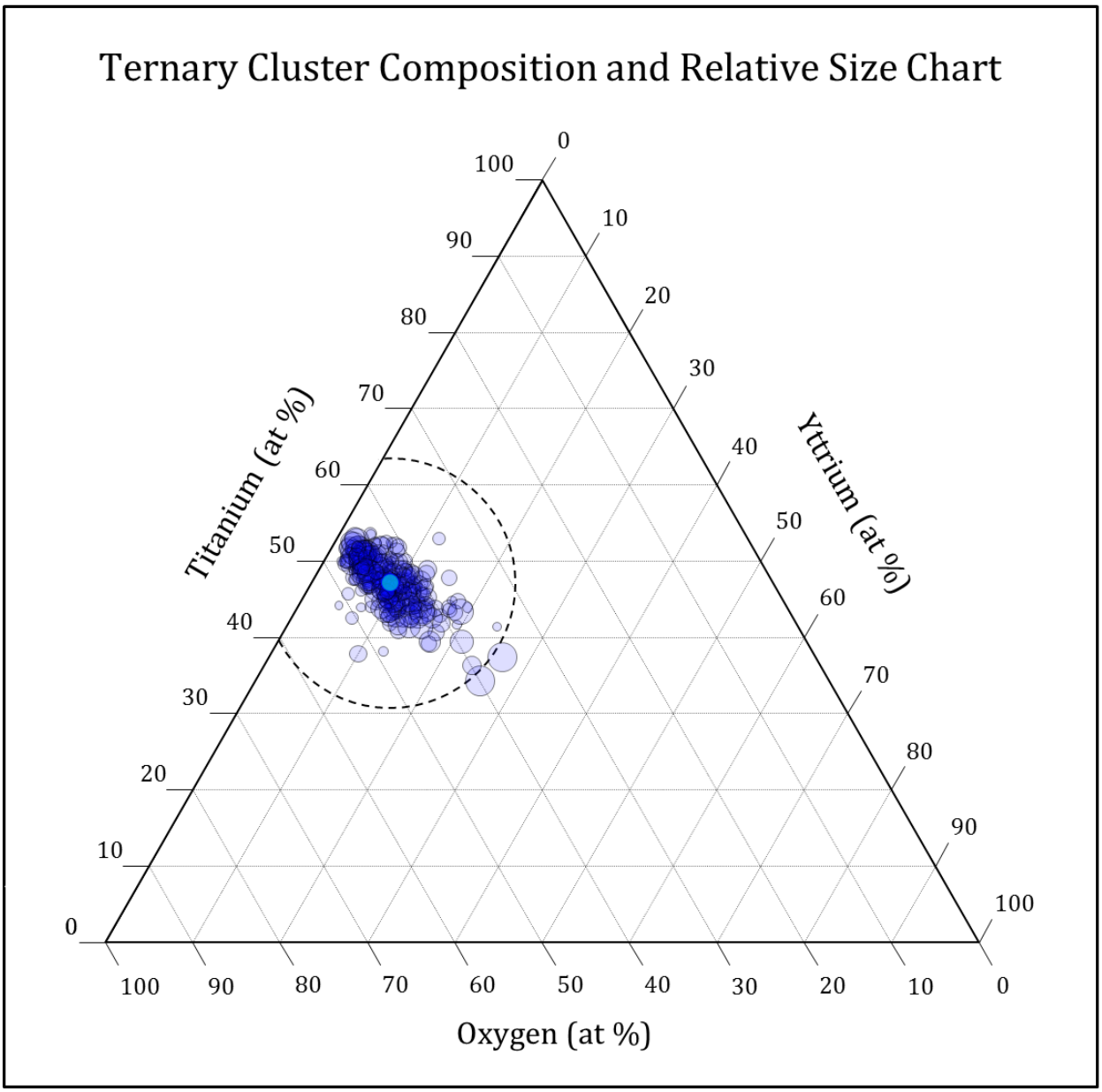

Figure 5.19 Multivariate diagram showing the compositions of the Y-Ti-O clusters in the 550 °C dataset under the assumption that only Y, Ti, and O atoms contribute to the composition of the particles. Each circle represents a single cluster, with the radius of the circle representing the Guinier radius of the particle, relative to the large dashed circle which has a 20 nm radius. The blue circle is located on the average composition and is shown with the average Guinier radius.

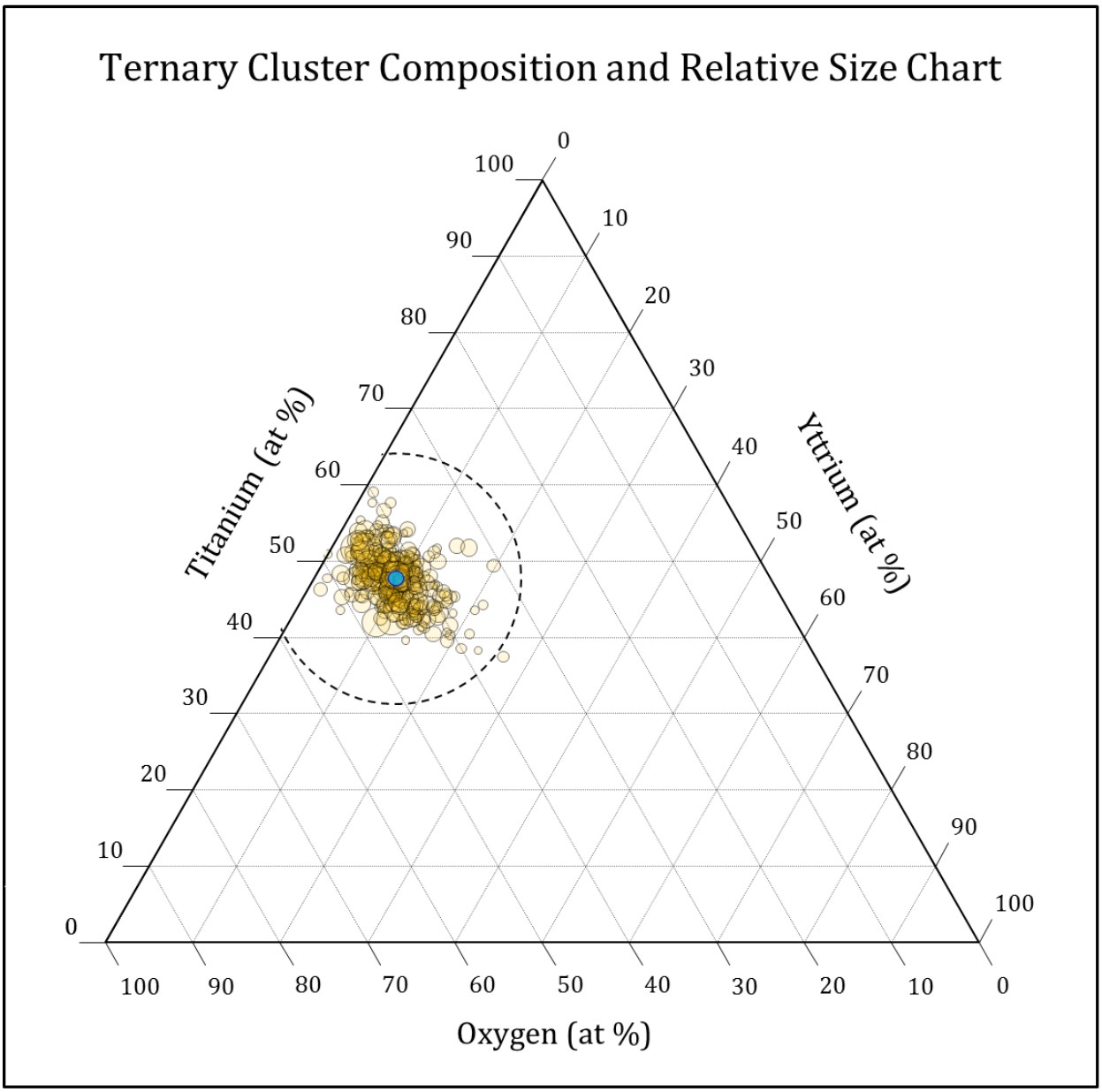

Figure 5.20 Multivariate diagram showing the compositions of the Y-Ti-O clusters in the 495 °C dataset under the assumption that only Y, Ti, and O atoms contribute to the composition of the particles. Each circle represents a single cluster, with the radius of the circle representing the Guinier radius of the particle, relative to the large dashed circle which has a 20 nm radius. The blue circle is located on the average composition and is shown with the average Guinier radius.

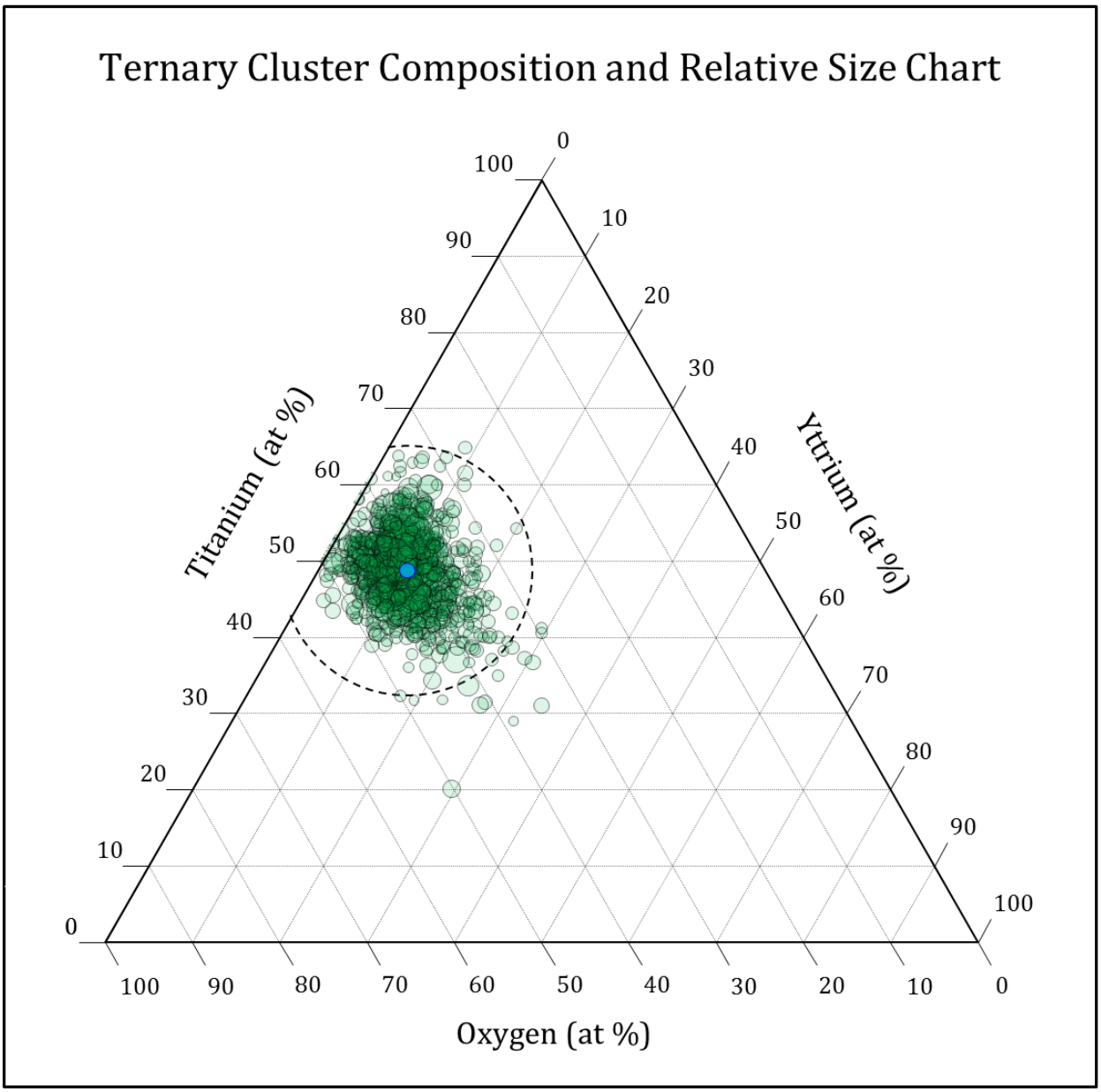

Figure 5.21 Multivariate diagram showing the compositions of the Y-Ti-O clusters in the 412 °C dataset under the assumption that only Y, Ti, and O atoms contribute to the composition of the particles. Each circle represents a single cluster, with the radius of the circle representing the Guinier radius of the particle, relative to the large dashed circle which has a 20 nm radius. The blue circle is located on the average composition and is shown with the average Guinier radius.

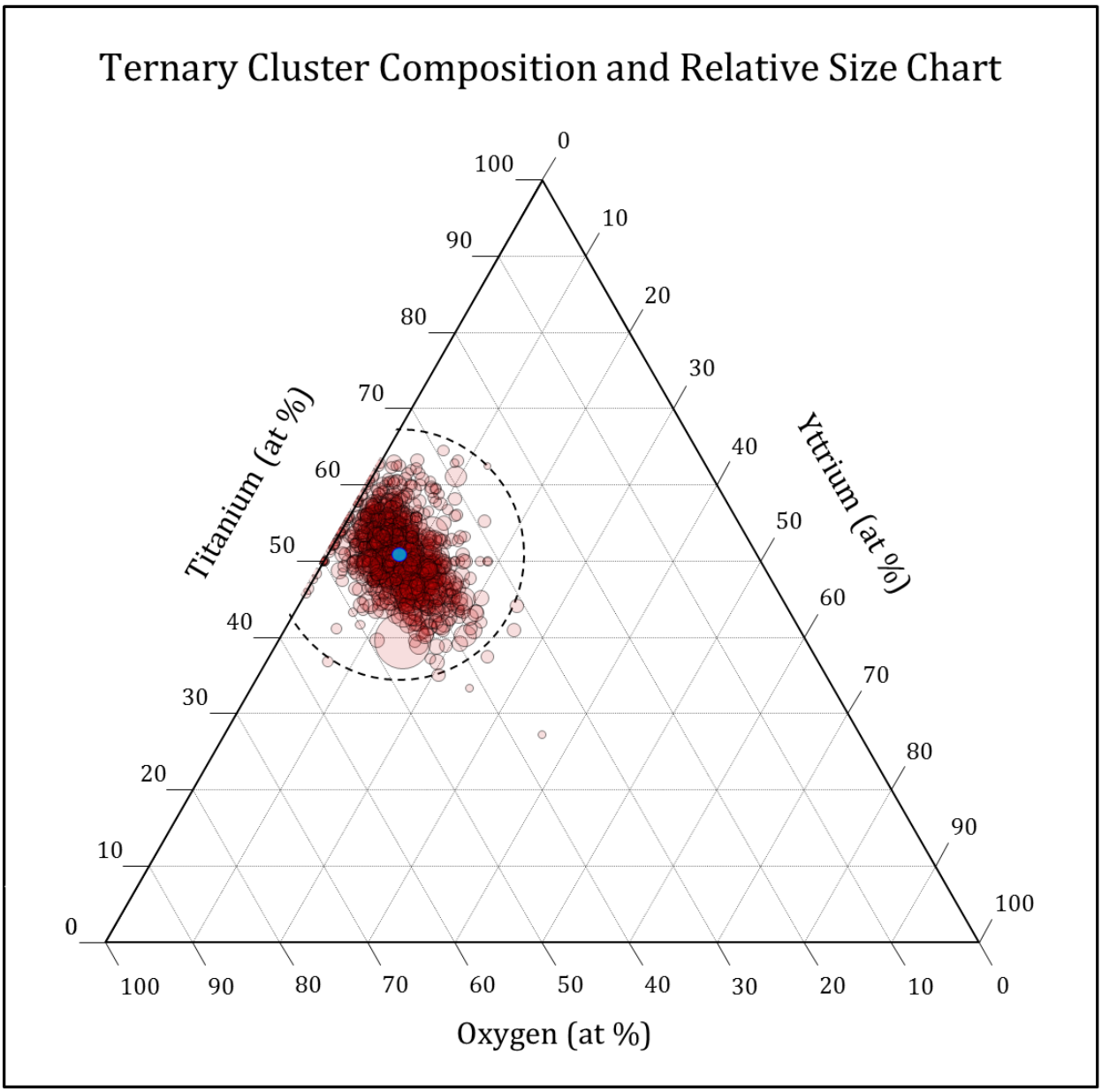

Figure 5.22 Multivariate diagram showing the compositions of the Y-Ti-O clusters in the 385 °C dataset under the assumption that only Y, Ti, and O atoms contribute to the composition of the particles. Each circle represents a single cluster, with the radius of the circle representing the Guinier radius of the particle, relative to the large dashed circle which has a 20 nm radius. The blue circle is located on the average composition and is shown with the average Guinier radius.

Grain boundary properties

Quantification of the solute enrichment at the observed grain boundaries was accomplished through the application of one-dimensional linescans. Like TiO ions were used previously as a marker for the location of the oxide particles, Ti ions will be used for the identification of grain boundaries.

Across the different irradiation conditions, the distribution of TiO (e.g. the distribution of oxide clusters) changes quite dramatically. As illustrated in Figure 5.23, at high irradiation temperatures, the TiO clusters that lie at the grain boundaries are consolidated into clearly distinguishable clusters. At low irradiation temperatures, the TiO is much more evenly distributed across the grain boundary surface. Figure 5.24-29 show the results of one dimensional titanium and titanium oxide linescans across the grain boundaries observed at each irradiation condition.

As was previously mentioned, the increase in Ti concentration indicates the location of the grain boundary along the linescan axis. When possible, the linescans were situated in the reconstruction as to avoid intersecting oxide particles. In the low temperature datasets, this was not possible due to the finely distributed TiO ions. At high irradiation temperatures, there is little to no enrichment of the TiO ions at the grain boundary. The entirety of the TiO present on the grain boundaries is consolidated in dense clusters. At low irradiation temperatures, the TiO concentration is significantly increased at the grain boundary. This indicates that the TiO ions have been redistributed along the grain boundary in the low temperature specimen, no large dense clusters are noted along the grain boundaries at low irradiation temperature.

The redistribution of TiO along the grain boundaries that is evidenced by Figure 5.24-29 supports the hypothesis that at lower irradiation temperatures, the reformation mechanism that drives the TiO back together following ballistic dissolution is inhibited. The oxide clusters that are broken apart by the incident radiation stay broken apart and redistribute the solute material across the surface of the grain boundary. Reformation becoming less inhibited as temperature increases is also supported by the data presented in Figure 5.30, which illustrates the TiO enrichment at the grain boundaries in both an overall linescan, and a selected area linescan, placed to avoid consolidated oxide particles. At higher temperatures, the TiO stays consolidated in clusters along the grain boundaries, evidencing that those particles that were dissolved ballistically were able to reform in a similar configuration as that they were in, presumably, and prior to dissolution. From the perspective of the effect on mechanical properties this redistribution of oxide solutes along the grain boundary is expected to embrittle the grain boundaries. The fact that oxides are present and redistributed along the boundary a GB weakening is not inconceivable. Figure 5.31b) shows an SEM micrograph of the fractured surface of the 412 °C tensile specimen.

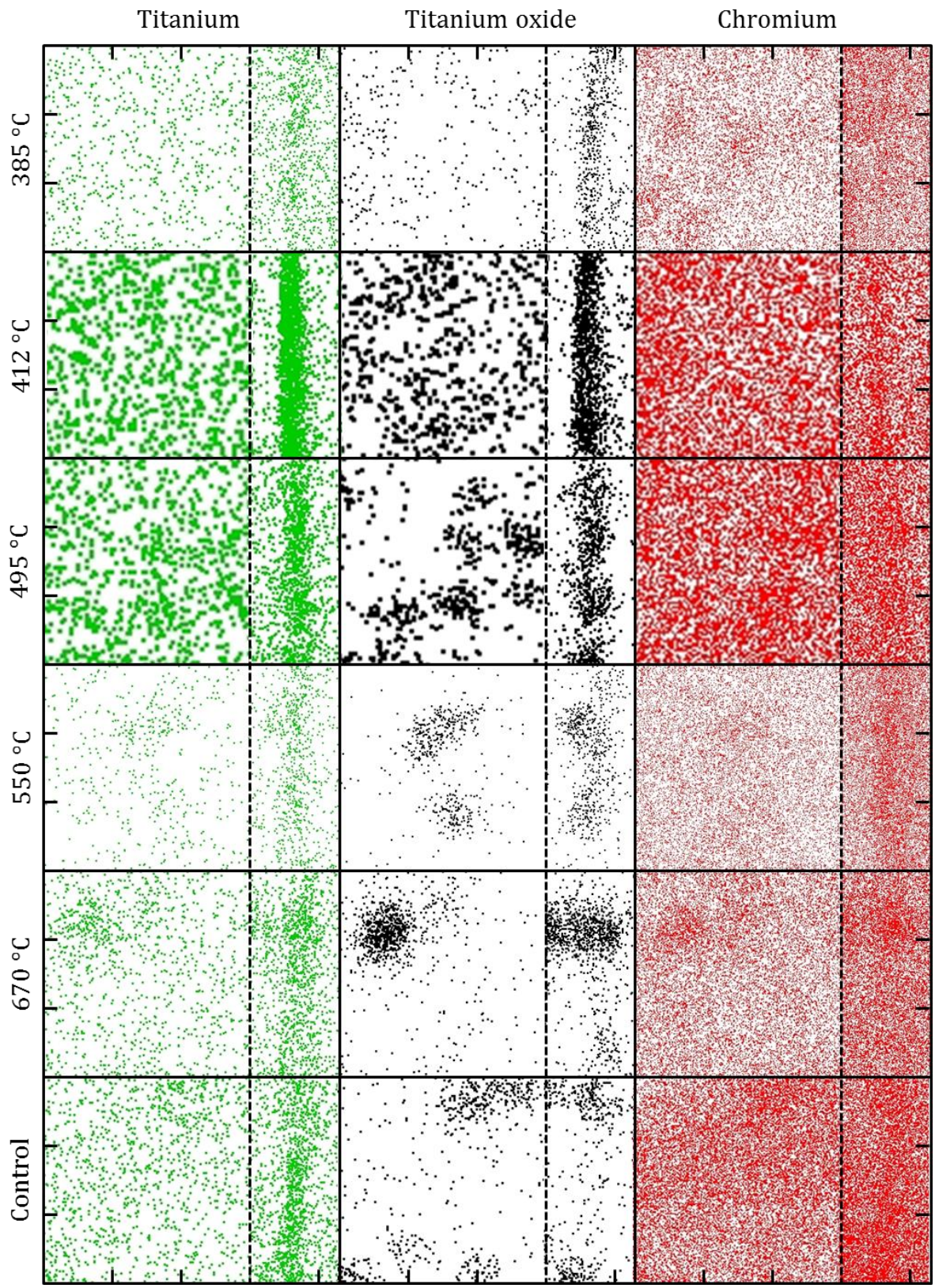

Figure 5.23 Representative distributions of titanium, titanium oxide and chromium ions on the grain boundaries across irradiation temperature. For each condition and ion species, a 15 x 15 nm face-on view of the grain boundary is shown (left) and a 15 x 6.5 nm edge-on view of the grain boundary is shown. It should be noted that the intensities of the ions in the images should not be considered, as the different sized datasets cause this aberration. Instead, notice the distribution of the ions, e.g. clustered or homogeneous.

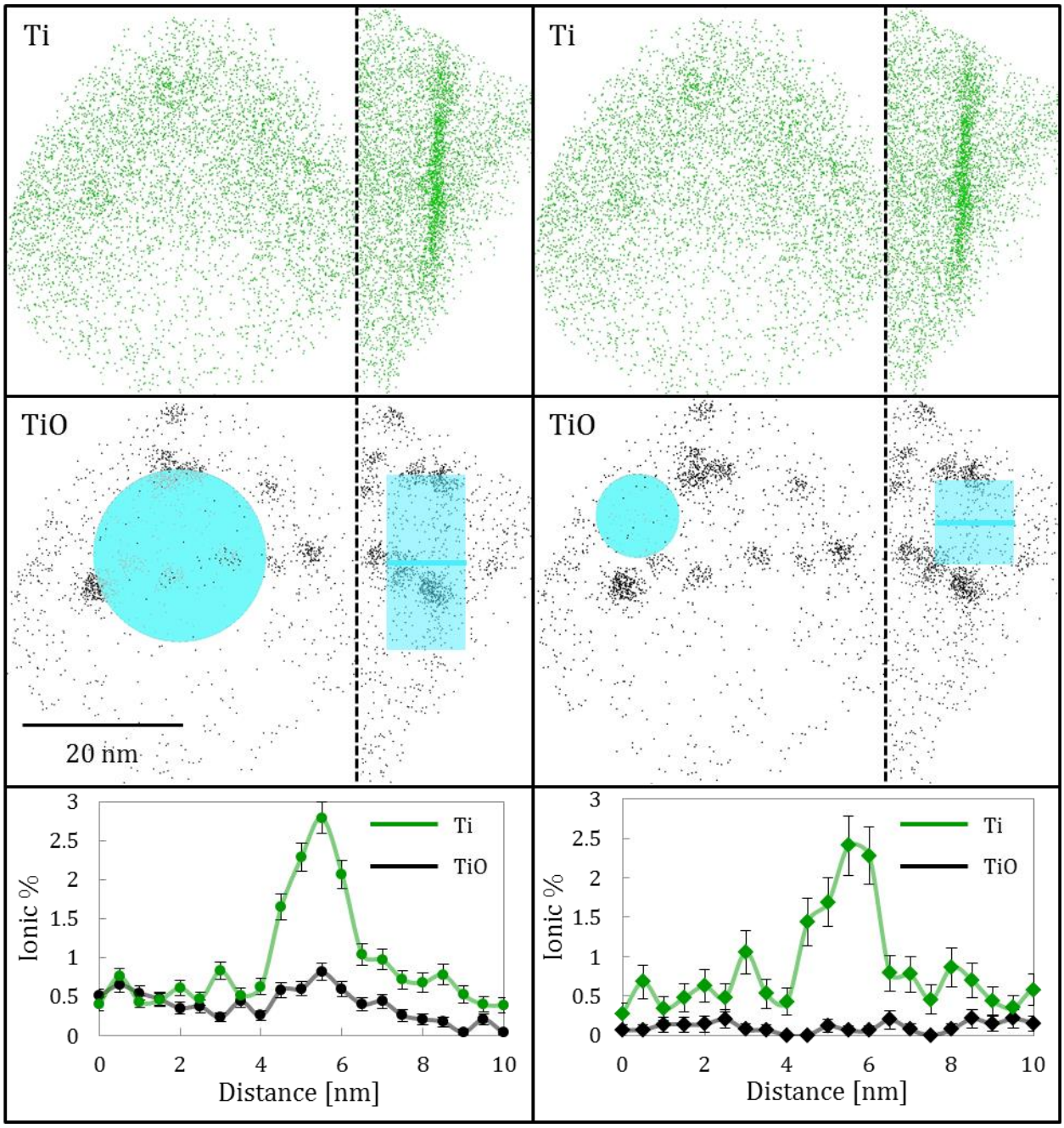

Figure 5.24 1 dimensional linescan of the ionic percent of titanium and titanium oxide ions across a grain boundary in the control material. Shown in the left section of the ion distributions on the left side are face-on ion distributions of the grain boundary, while on the right are edge-on views. The linescans utilized 0.5 nm bin widths. The left set of plots describe the placement of a large, overall linescan, while the right set describe the placement of a local linescan place to avoid consolidated titanium oxide clusters.

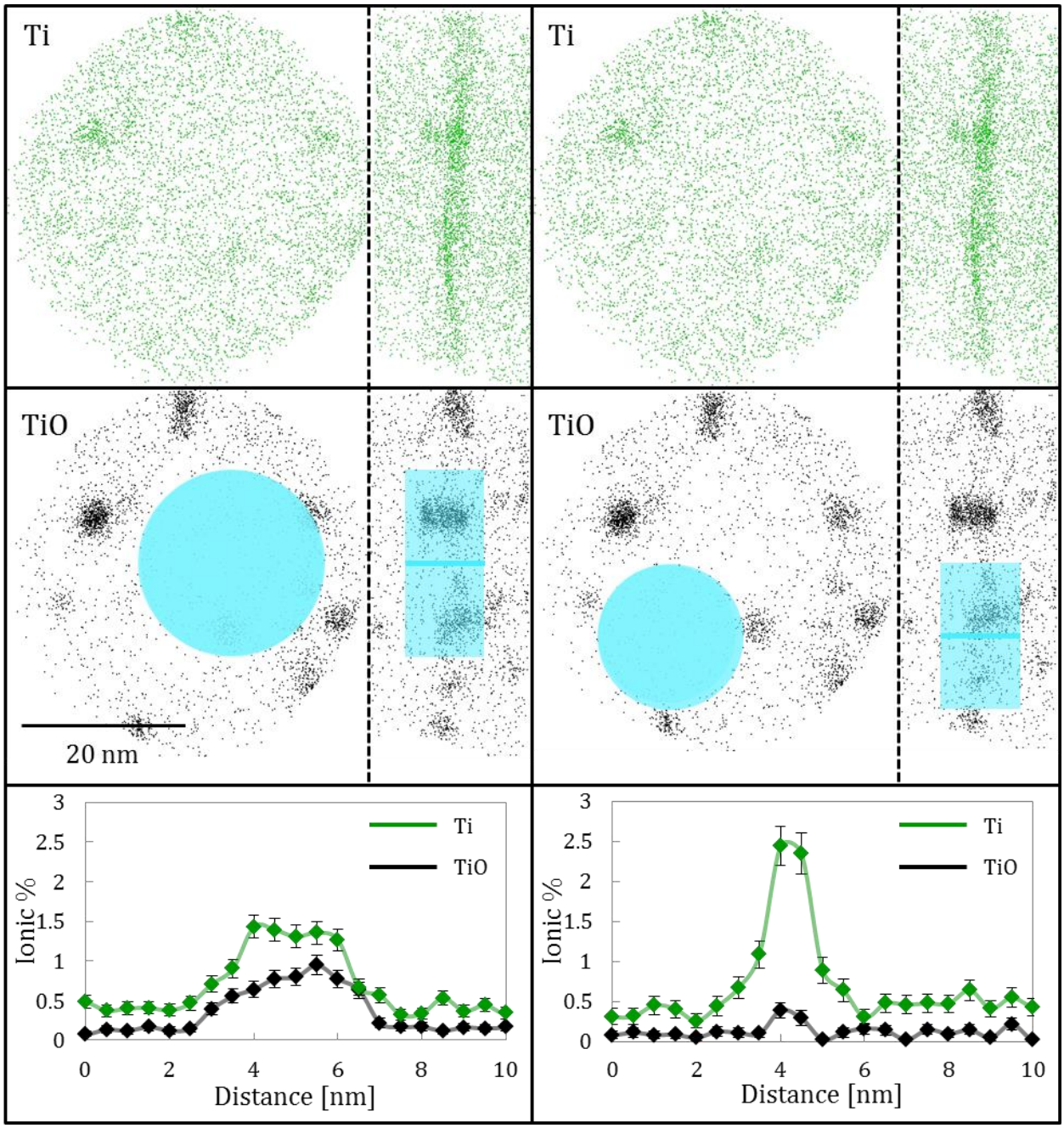

Figure 5.25 1 dimensional linescan of the ionic percent of titanium and titanium oxide ions across a grain boundary in the 670 °C material. Shown in the left section of the ion distributions on the left side are face-on ion distributions of the grain boundary, while on the right are edge-on views. The linescans utilized 0.5 nm bin widths. The left set of plots describe the placement of a large, overall linescan, while the right set describe the placement of a local linescan place to avoid consolidated titanium oxide clusters.

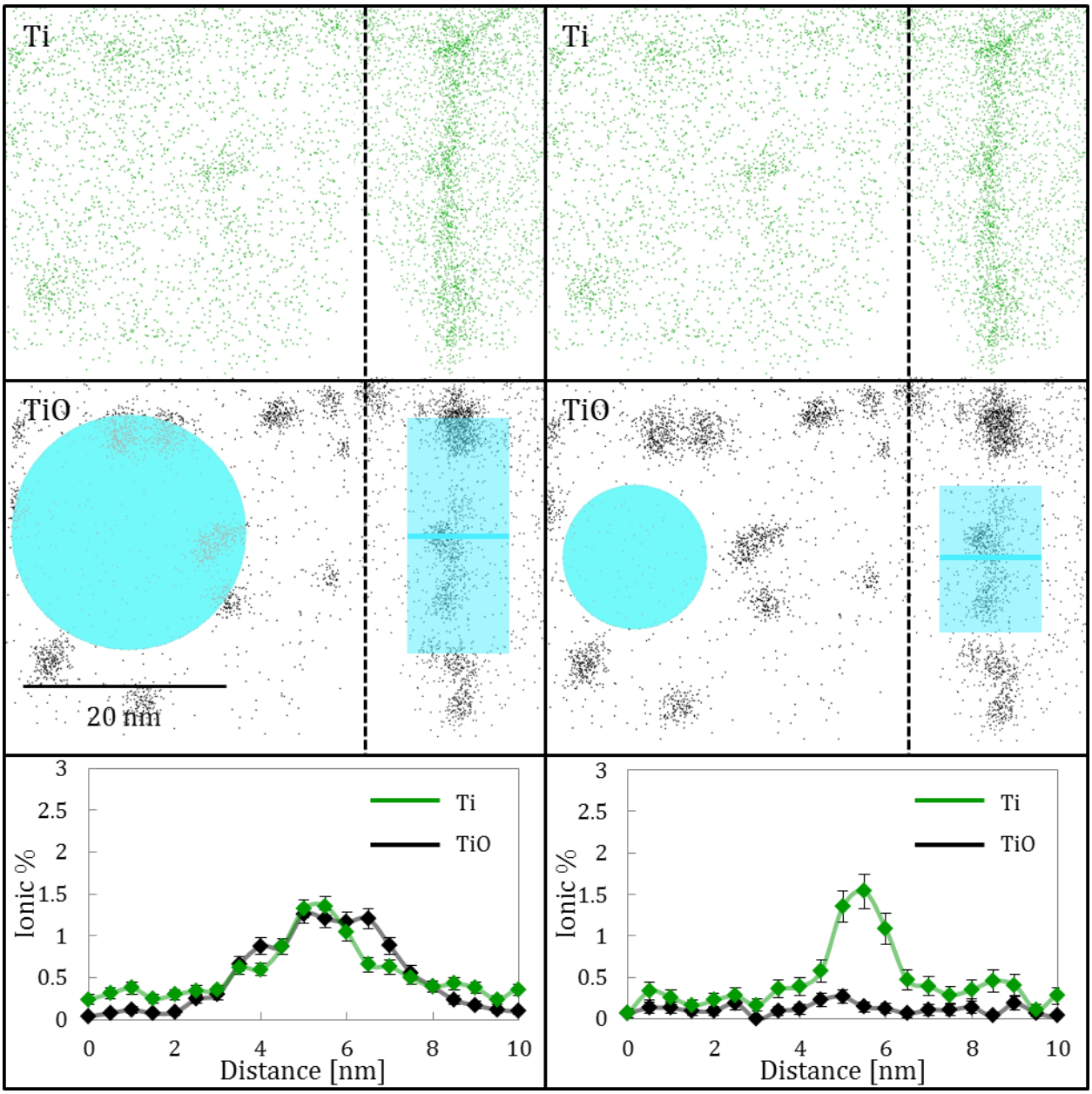

Figure 5.261 dimensional linescan of the ionic percent of titanium and titanium oxide ions across a grain boundary in the 550 °C material. Shown in the left section of the ion distributions on the left side are face-on ion distributions of the grain boundary, while on the right are edge-on views. The linescans utilized 0.5 nm bin widths. The left set of plots describe the placement of a large, overall linescan, while the right set describe the placement of a local linescan place to avoid consolidated titanium oxide clusters.

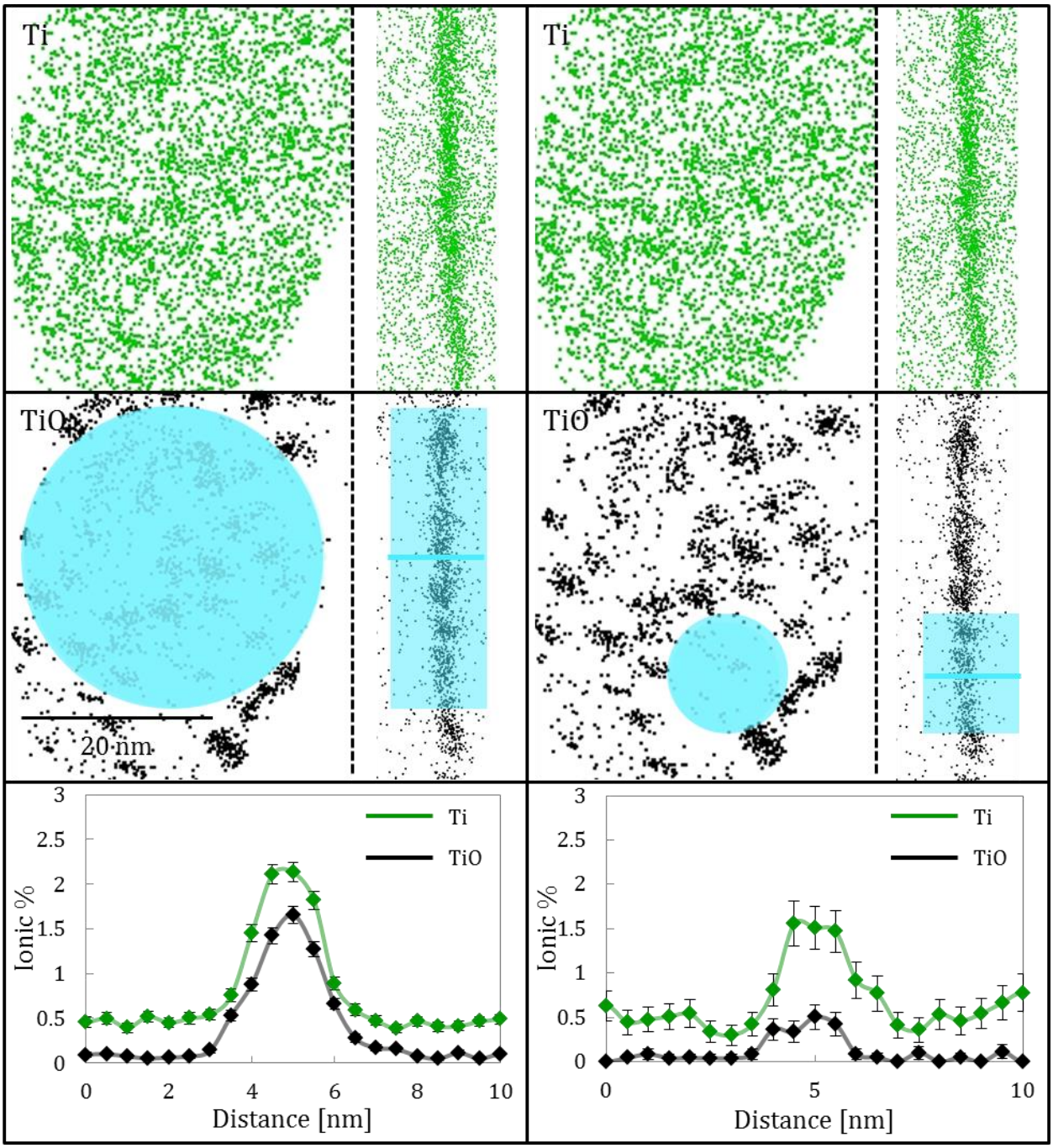

Figure 5.27 1 dimensional linescan of the ionic percent of titanium and titanium oxide ions across a grain boundary in the 495 °C material. Shown in the left section of the ion distributions on the left side are face-on ion distributions of the grain boundary, while on the right are edge-on views. The linescans utilized 0.5 nm bin widths. The left set of plots describe the placement of a large, overall linescan, while the right set describe the placement of a local linescan place to avoid consolidated titanium oxide clusters.

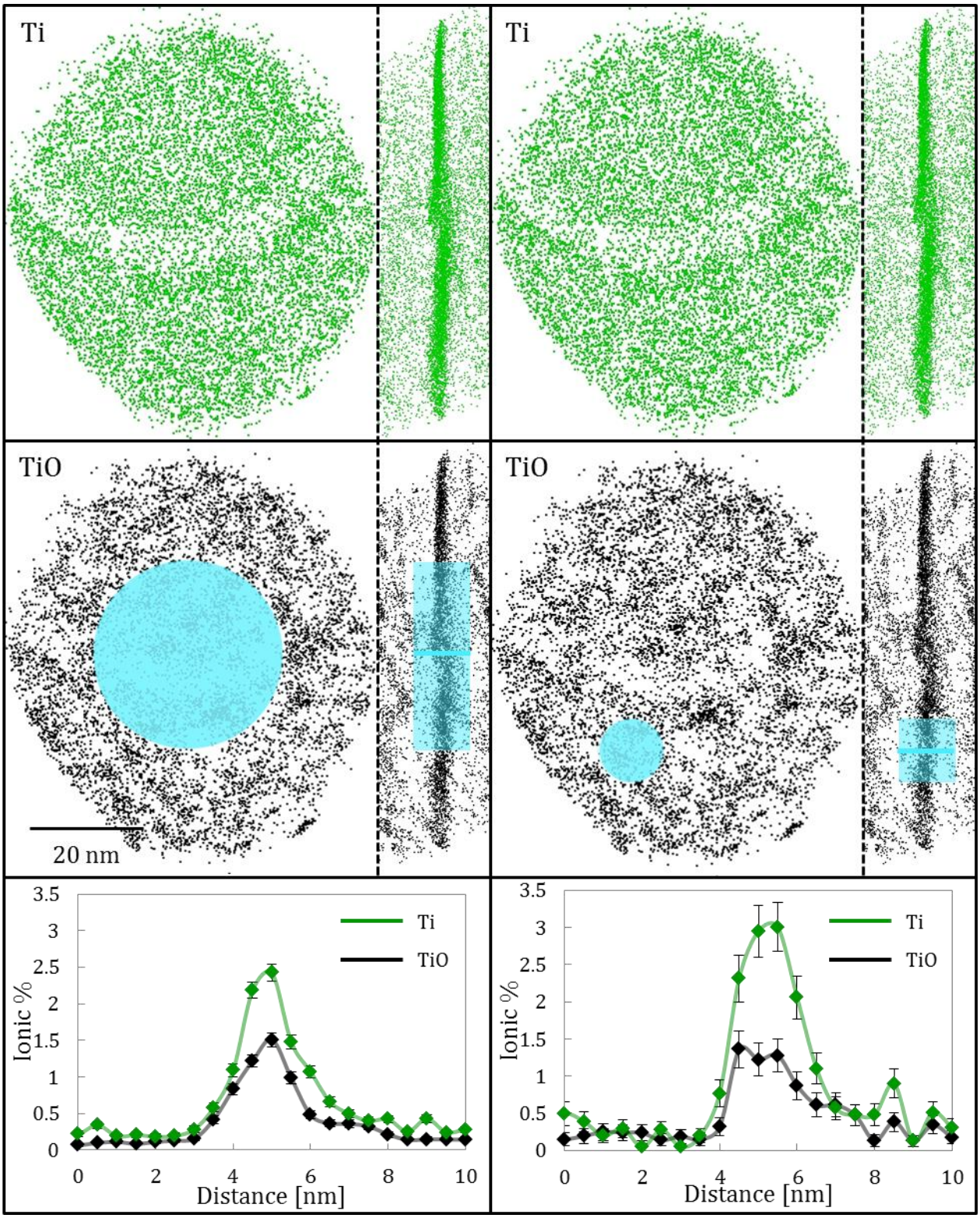

Figure 5.281 dimensional linescan of the ionic percent of titanium and titanium oxide ions across a grain boundary in the 412 °C material. Shown in the left section of the ion distributions on the left side are face-on ion distributions of the grain boundary, while on the right are edge-on views. The linescans utilized 0.5 nm bin widths. The left set of plots describe the placement of a large, overall linescan, while the right set describe the placement of a local linescan place to avoid consolidated titanium oxide clusters.

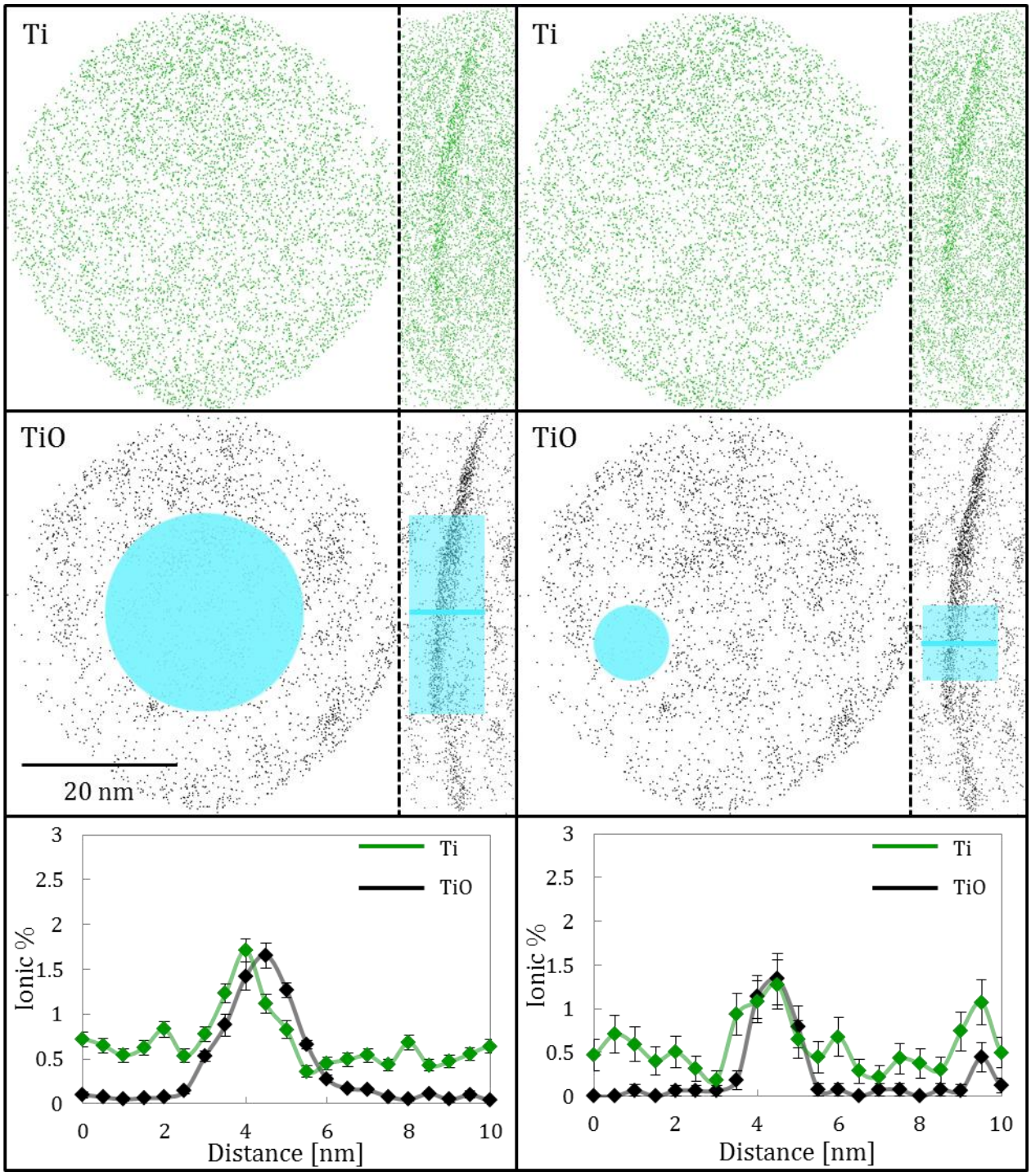

Figure 5.29 1 dimensional linescan of the ionic percent of titanium and titanium oxide ions across a grain boundary in the 385 °C material. Shown in the left section of the ion distributions on the left side are face-on ion distributions of the grain boundary, while on the right are edge-on views. The linescans utilized 0.5 nm bin widths. The left set of plots describe the placement of a large, overall linescan, while the right set describe the placement of a local linescan place to avoid consolidated titanium oxide clusters.

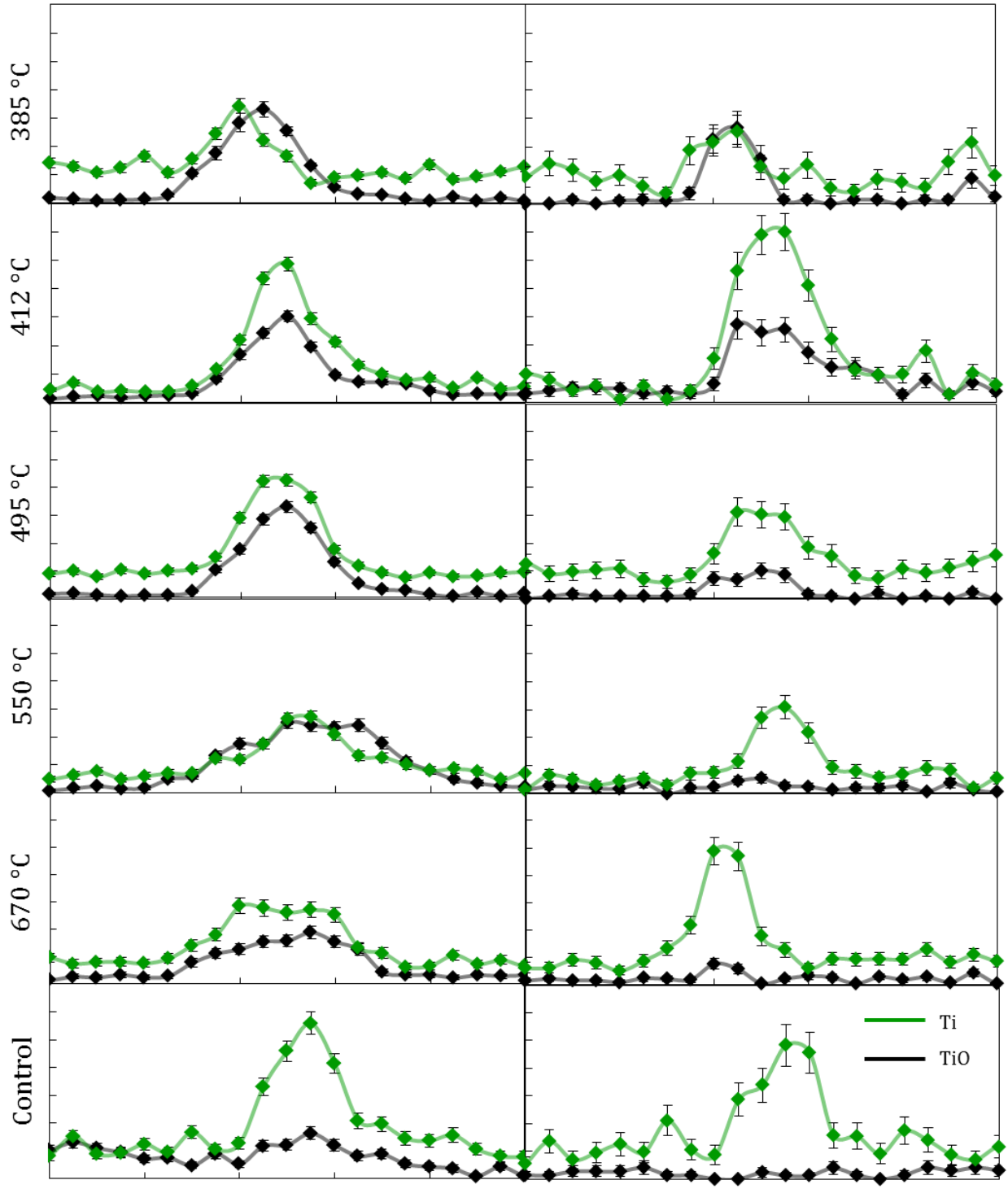

Figure 5.30 Titanium and titanium oxide 1 dimensional ionic concentration linescans across grain boundaries at each irradiation temperature. All plots use the same scale, 0-3.5% (ionic) in steps of 0.5% and the horizontal axis indicates the distance along the linescan in steps of 2 nm. The plots on the left indicate the trends observed in these solutes overall across the grain boundaries, while the plots on the right show the trends in selected area linescans where the area of interest is the grain boundary between oxide clusters.

This image was acquired by collaborating scientists at PNNL. The v-shaped fractures appear to be intergranular brittle failure that cracked parallel to the tensile direction. The failure mode perpendicular to the tensile direction appears to be ductile transgranular fracture, but the total elongation of the low temperature samples indicates significant reduction in strain under those irradiation conditions, compared to the moderate changes shown by the high temperature samples, relative to the control material.

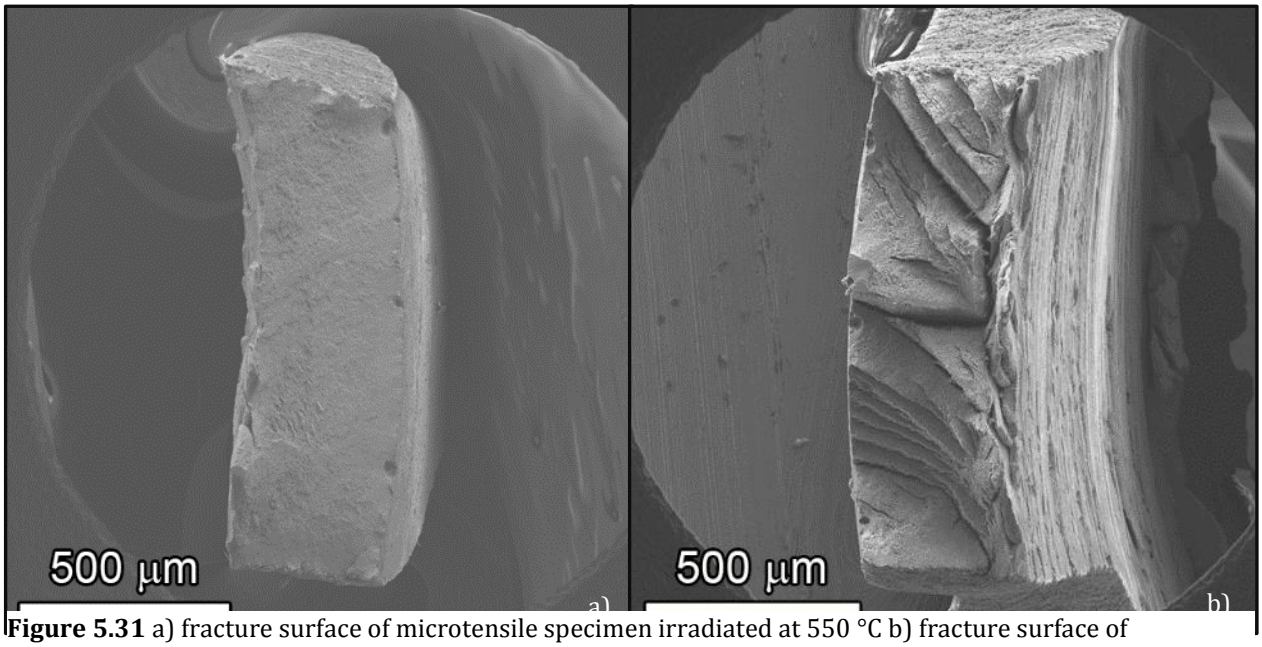

Figure 5.31 a) fracture surface of microtensile specimen irradiated at 550 °C b) fracture surface of microtensile specimen irradiated at 412 °C *[66]*.

Figure 5.23 also depicts the change in chromium enrichment at the grain boundaries across the irradiation temperatures. In the control material, chromium is enriched at the grain boundaries to about 20% (atomic) compared to the matrix composition of 15% (atomic). One-dimensional linescans show the enrichment of chromium at the grain boundaries quantitatively and are given in Figure 5.32-37. Similarly to Figure 5.24-29, the Ti enrichment peak indicates the location of the grain boundary. The high temperature specimens exhibited a similar chromium enrichment to that of the control material. However, at low temperatures, the chromium is depleted from the grain boundaries, presumably consumed during the formation of the α' precipitates, which will be discussed later.

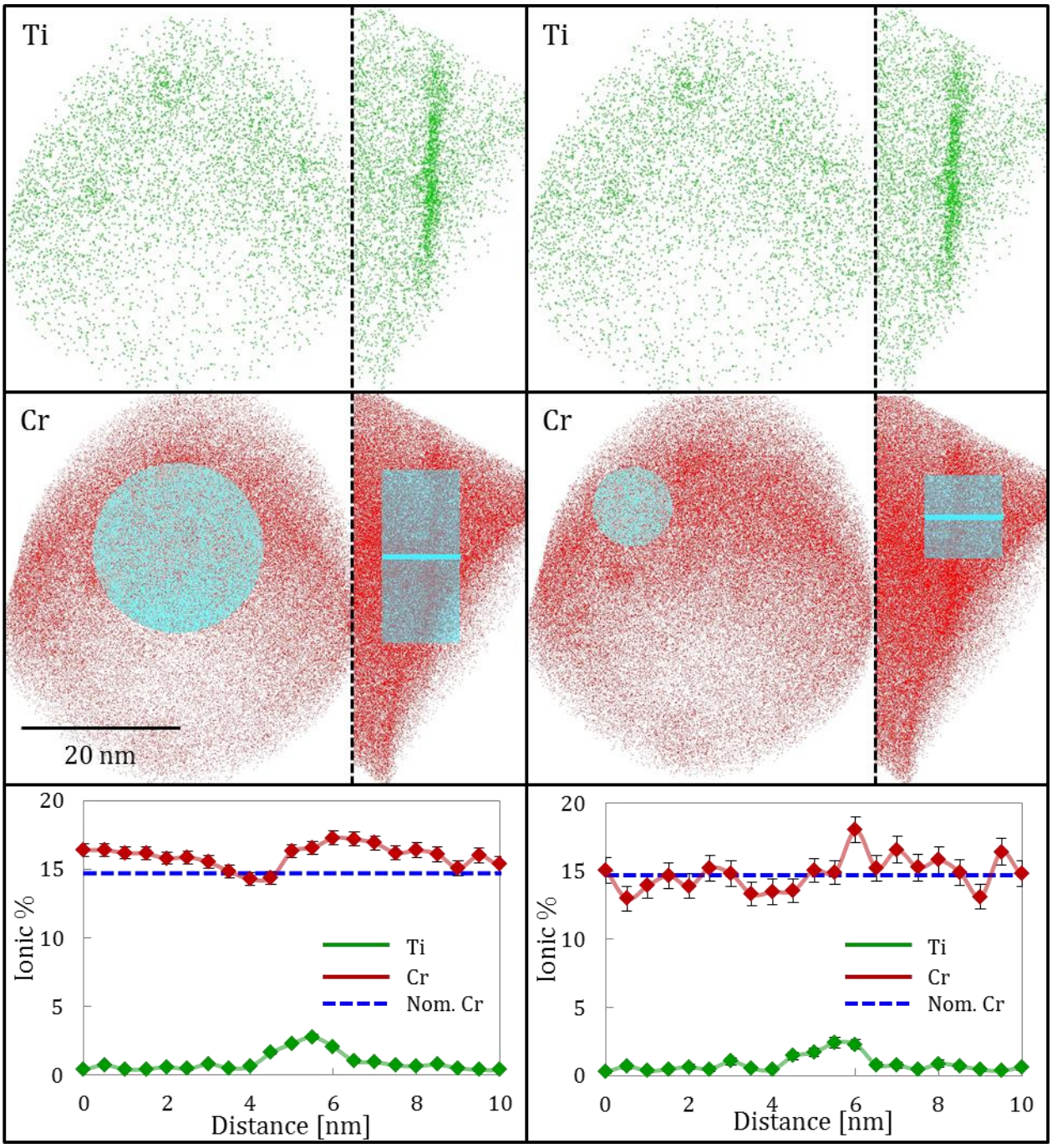

Figure 5.321 dimensional linescan of the ionic percent of titanium and chromium ions across a grain boundary in the control material. Shown in the left section of the ion distributions on the left side are face-on ion distributions of the grain boundary, while on the right are edge-on views. The linescans utilized 0.5 nm bin widths. The left set of plots describe the placement of a large, overall linescan, while the right set describe the placement of a local linescan place to avoid consolidated chromium clusters.

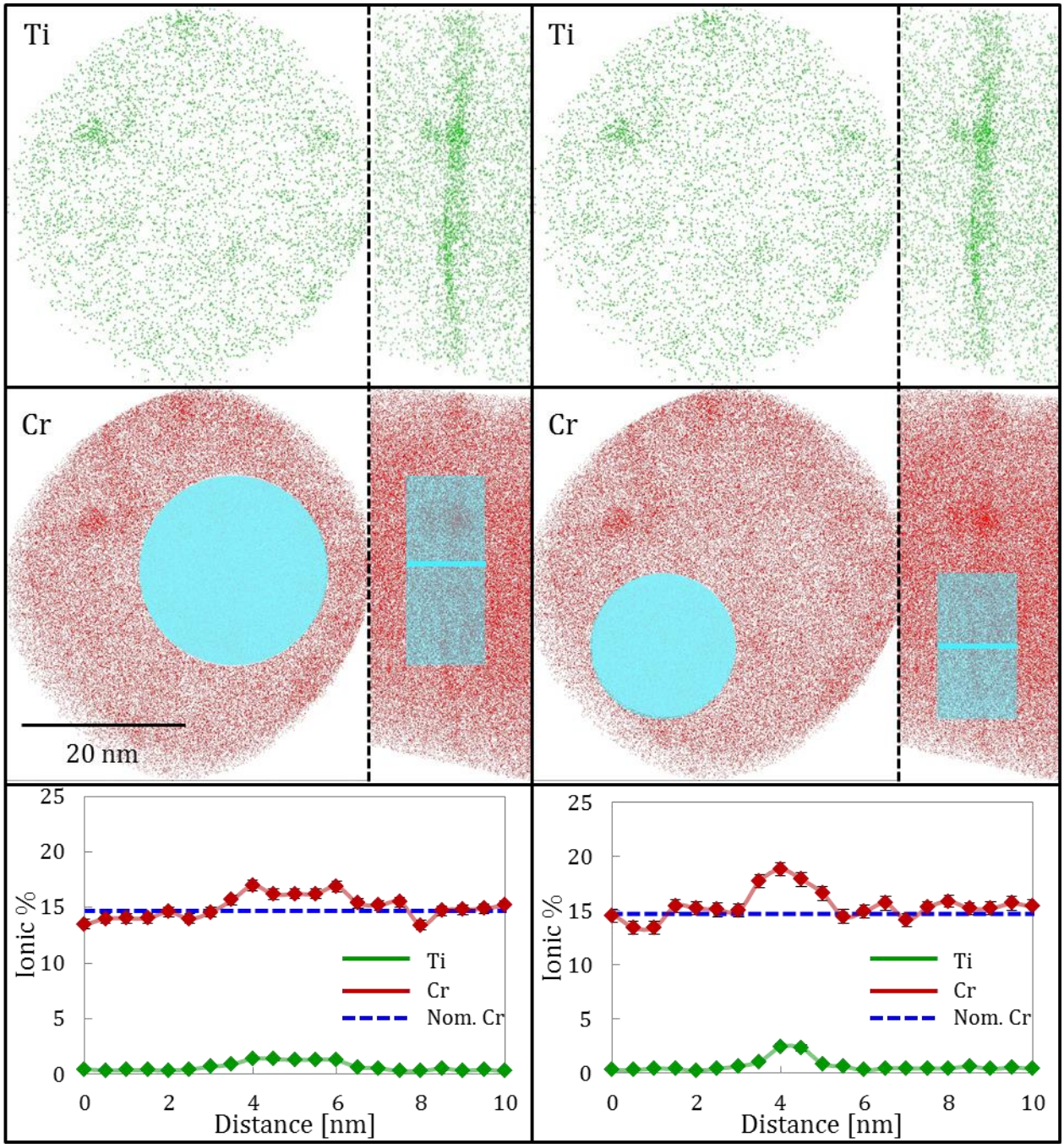

Figure 5.331 dimensional linescan of the ionic percent of titanium and chromium ions across a grain boundary in the 670 °C material. Shown in the left section of the ion distributions on the left side are face-on ion distributions of the grain boundary, while on the right are edge-on views. The linescans utilized 0.5 nm bin widths. The left set of plots describe the placement of a large, overall linescan, while the right set describe the placement of a local linescan place to avoid consolidated chromium clusters.

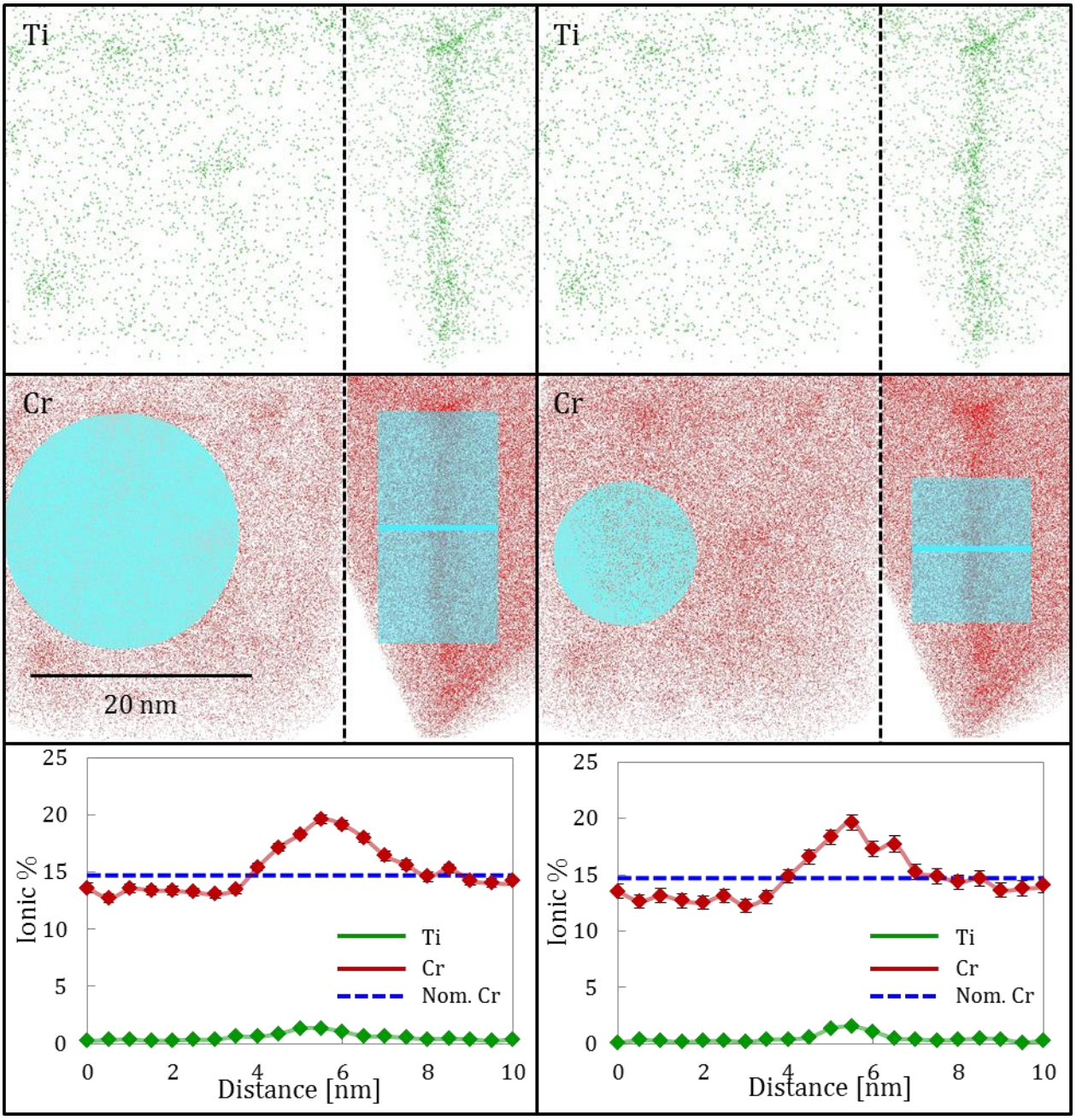

Figure 5.34 1 dimensional linescan of the ionic percent of titanium and chromium ions across a grain boundary in the 550 °C material. Shown in the left section of the ion distributions on the left side are face-on ion distributions of the grain boundary, while on the right are edge-on views. The linescans utilized 0.5 nm bin widths. The left set of plots describe the placement of a large, overall linescan, while the right set describe the placement of a local linescan place to avoid consolidated chromium clusters.

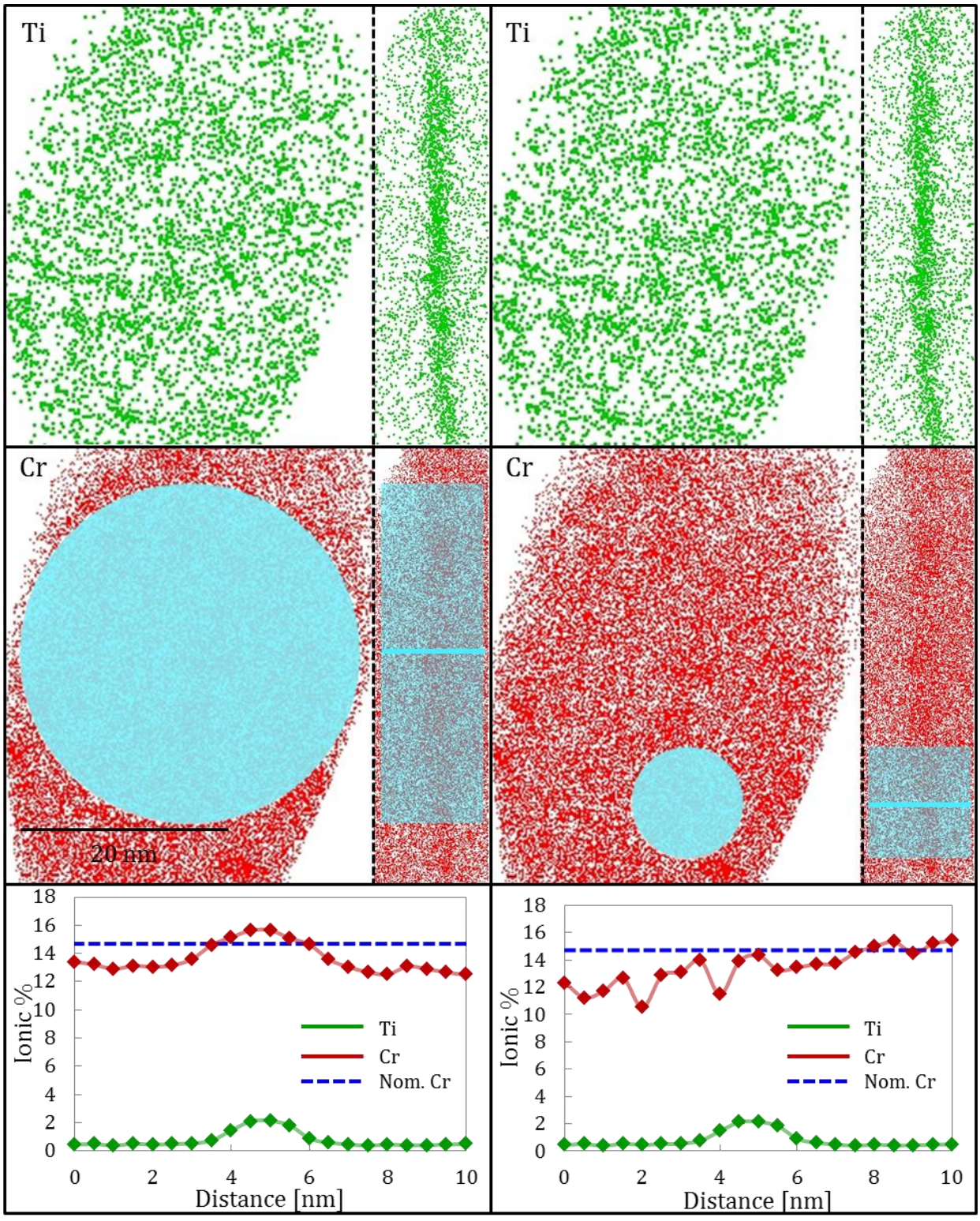

Figure 5.351 dimensional linescan of the ionic percent of titanium and chromium ions across a grain boundary in the 495 °C material. Shown in the left section of the ion distributions on the left side are face-on ion distributions of the grain boundary, while on the right are edge-on views. The linescans utilized 0.5 nm bin widths. The left set of plots describe the placement of a large, overall linescan, while the right set describe the placement of a local linescan place to avoid consolidated chromium clusters.

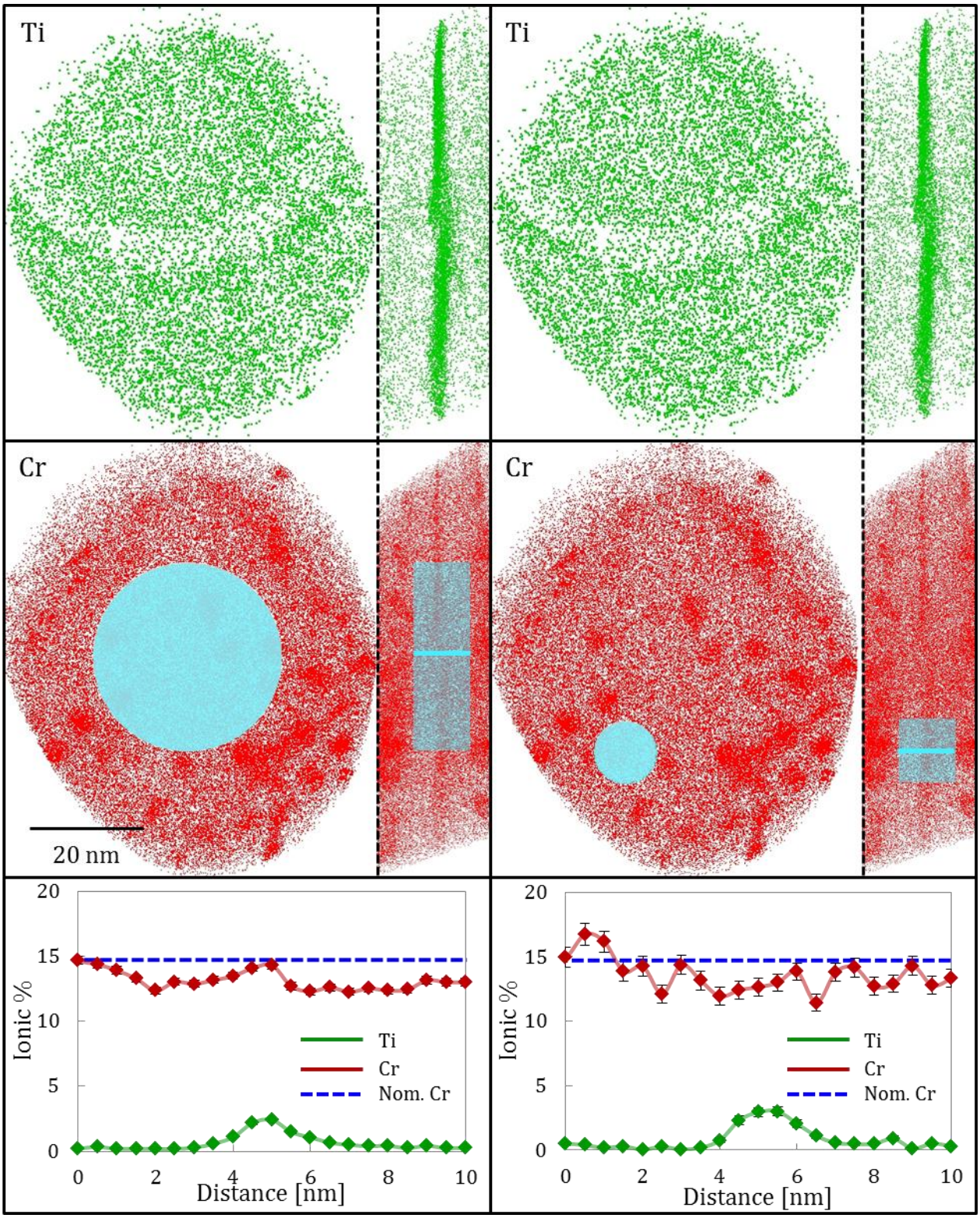

Figure 5.361 dimensional linescan of the ionic percent of titanium and chromium ions across a grain boundary in the 412 °C material. Shown in the left section of the ion distributions on the left side are face-on ion distributions of the grain boundary, while on the right are edge-on views. The linescans utilized 0.5 nm bin widths. The left set of plots describe the placement of a large, overall linescan, while the right set describe the placement of a local linescan place to avoid consolidated chromium clusters.

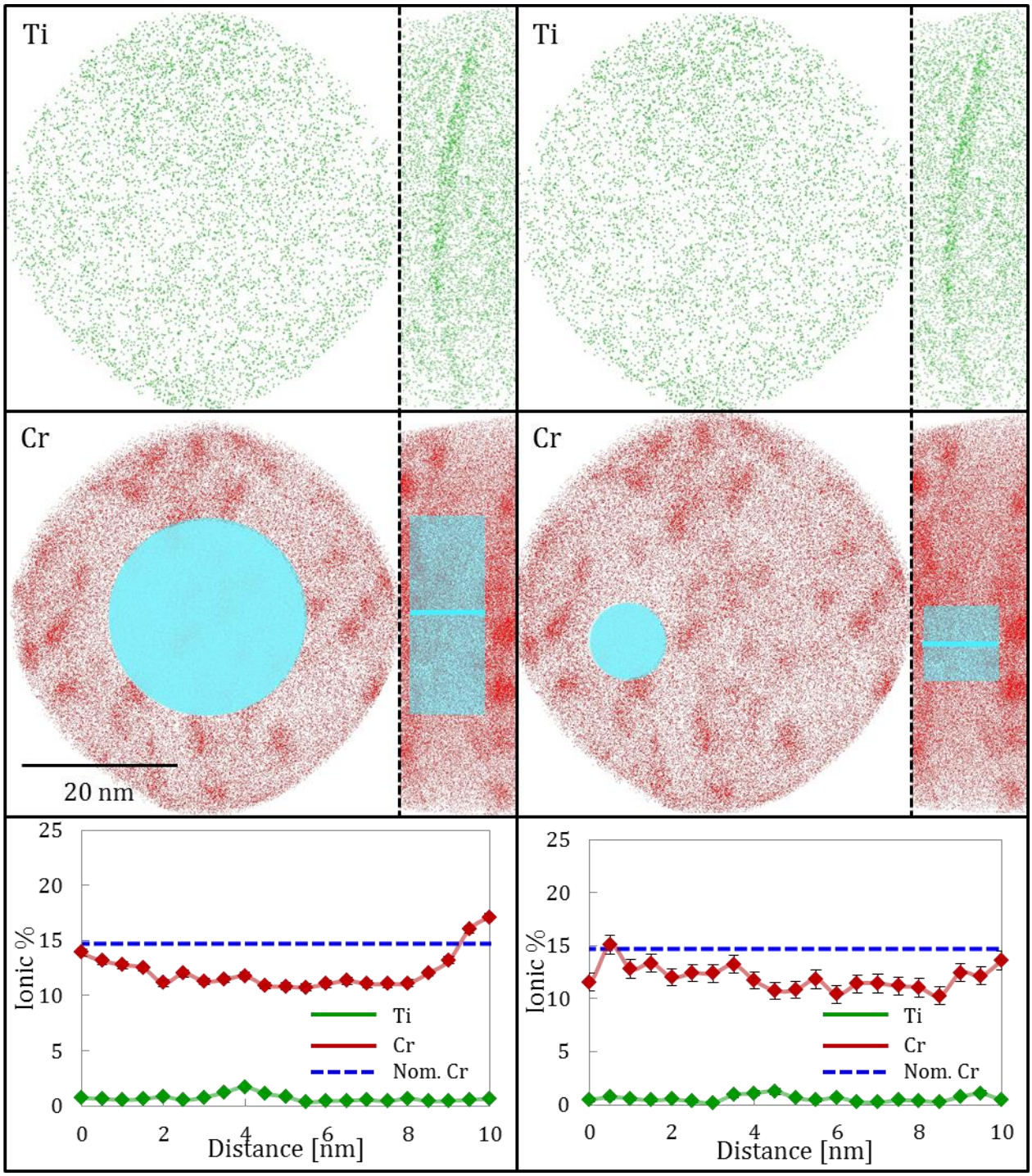

Figure 5.371 dimensional linescan of the ionic percent of titanium and chromium ions across a grain boundary in the 385 °C material. Shown in the left section of the ion distributions on the left side are face-on ion distributions of the grain boundary, while on the right are edge-on views. The linescans utilized 0.5 nm bin widths. The left set of plots describe the placement of a large, overall linescan, while the right set describe the placement of a local linescan place to avoid consolidated chromium clusters.

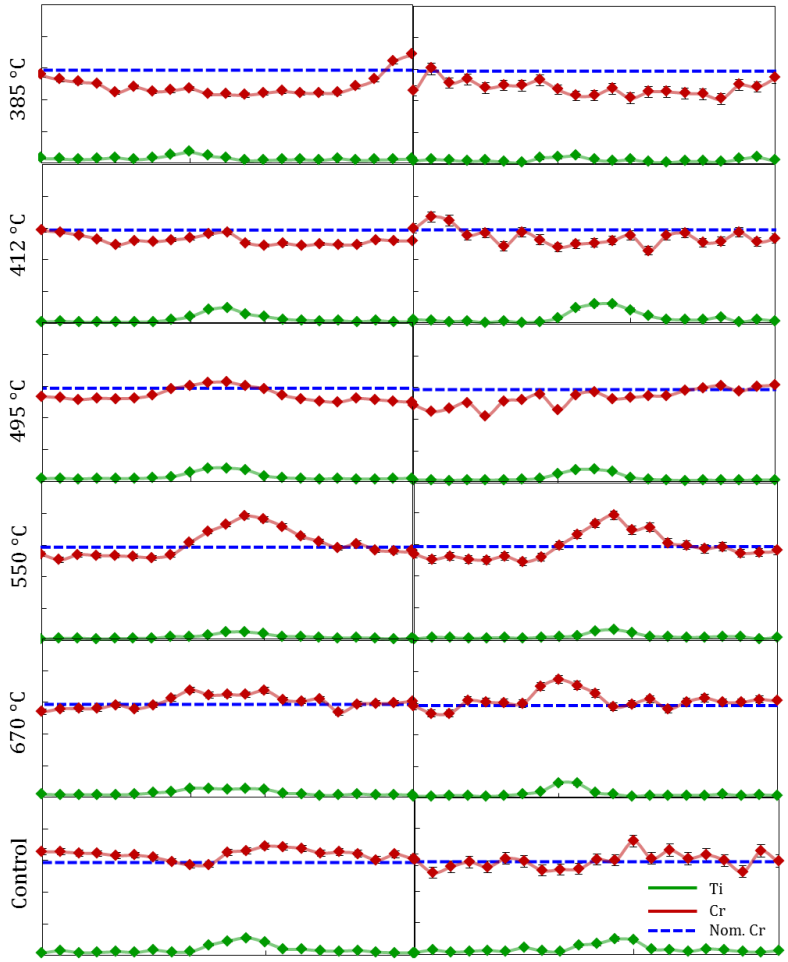

Figure 5.38 Titanium and chromium 1 dimensional ionic concentration linescans across grain boundaries at each irradiation temperature. All plots use the same scale, 0-25% (ionic) in steps of 5% and the horizontal axis indicates the distance along the linescan in steps of 2 nm. The plots on the left indicate the trends observed in these solutes overall across the grain boundaries, while the plots on the right show the trends in selected area linescans where the area of interest is the grain boundary between chromium enrichments.

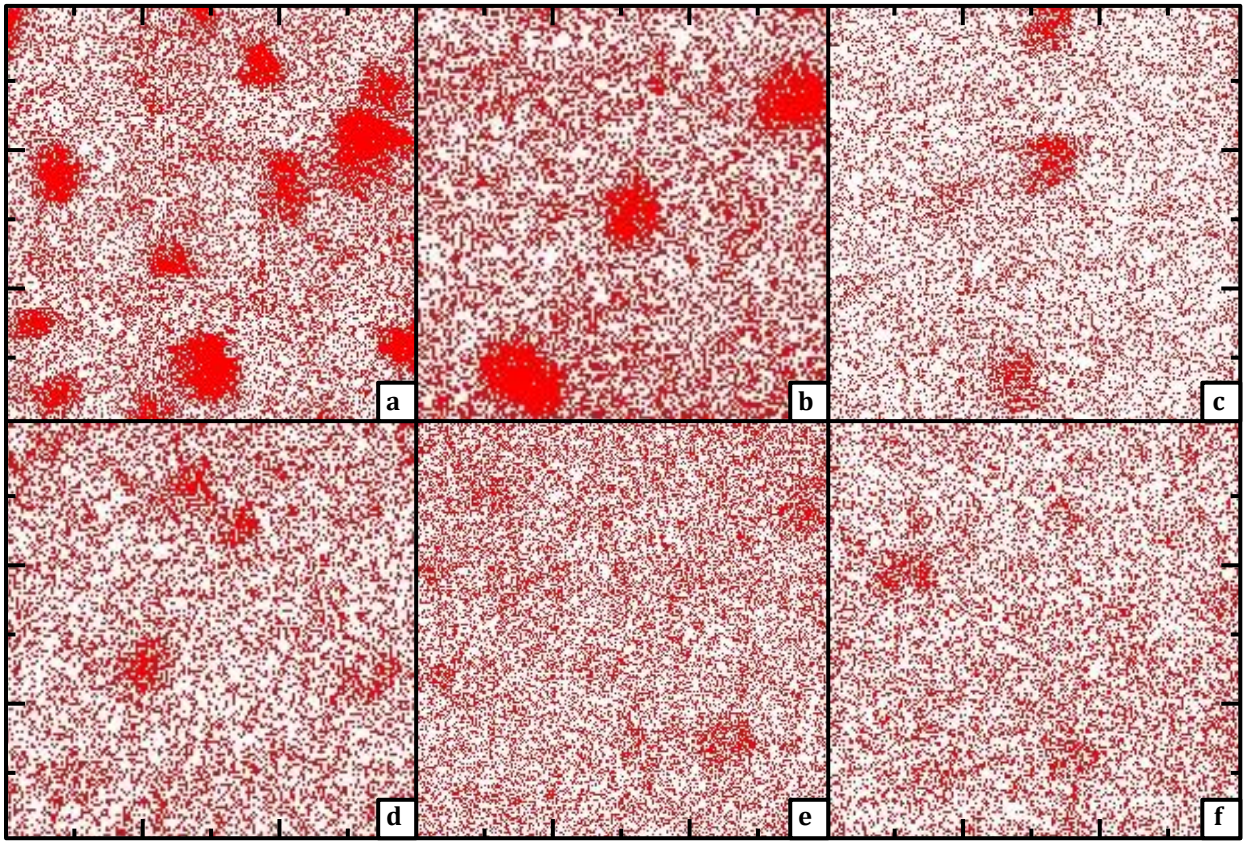

Figure 5.39 Chromium ion distribution as a function of irradiation temperature. Each section is a square region is a slice (30 nm x 30 nm x ~2 nm) taken from a representative area of the reconstruction. The number of chromium enrichments in each section is not necessarily indicative of the chromium enrichment densities overall, but rather are intended to illustrate the clustering character of the chromium ions. a) 385 °C b) 412 °C c) 495 °C d) 550 °C e) 670 °C f) Control.

Secondary phase formation

Figure 5.39 shows globular enrichments of chromium between oxide clusters in the low irradiation temperature specimens. Noted previously in other high chromium ferritic steels [105] these precipitates are thought to be α'. Due to the low temperature at which α' is thought to form, it is usually observed under irradiation, where the kinetics are enhanced enough to allow its formation in a reasonable period of time. This experimental observation of α' provides more data to drive existing thermodynamic models of the phase boundary of α'. Illustrations of various thermodynamic simulations of the α' phase boundary are shown in Figure 5.40. Temperatures and chromium concentrations of these observations have been added to the chart as points.

Interestingly, these enrichments appear in between the oxide particles. This is counter-intuitive, as in general, if precipitates, or even small defects, already exist in solution, these areas will provide high energy zones where the barrier for formation of new precipitates is lowered. This is known as heterogeneous nucleation. Therefore, a newly precipitated phase such as α' would be expected to be associated with, or even envelope, the oxide clusters. This is clearly not the case in these samples. Obvious from Figure 5.39 is an anti-correlation trend between the oxide clusters and the α' precipitates. Figure 5.42 shows

even stronger evidence of α' precipitates forming between oxide clusters due to the formation of complex, high surface area shapes in order to avoid contacting oxide clusters.

There are several possible explanations for this morphology. The first has to do with kinetics. The way the oxide clusters provide radiation tolerance is by annihilating point defects produced in displacement cascades at the oxide/matrix interface. Therefore, the region immediately surrounding the oxide particle will be depleted of point defects, which implies fewer kinetic pathways for formation of another phase. Further away from the oxide interface, the point defect concentration will be higher, apparently high enough to allow the formation of a new phase through homogeneous nucleation.

However, at 550 °C, it can be seen that the oxide interfaces are enriched with chromium.

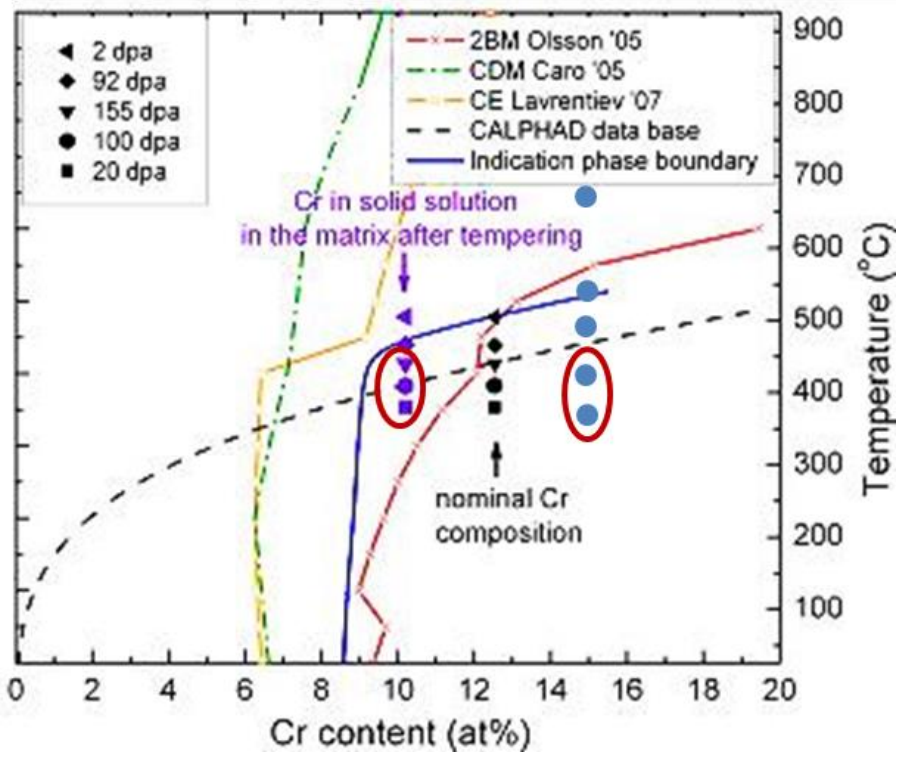

Figure 5.40 Phase diagram focusing on the *α'* phase boundary. Included are several predictions of the boundary location. Plotted in purple are experiments where *α'* was observed (circled in red) in *[105]*. Plotted in blue are the observations of *α'* precipitation (circled in red) in this study.

This is shown in Figure 5.41. The enrichment does not imply that α' was beginning to form on the interface at the higher irradiation temperature, but rather that the oxide/matrix interface was enriched with chromium to a similar extent that the grain boundaries are enriched at that temperature. The chromium content at the oxide/matrix interface at 550 °C is 20 atom% compared to the matrix concentration of 15 atom %. The grain boundary chromium content is 20 atom %; so, α' is not forming at 550 °C.

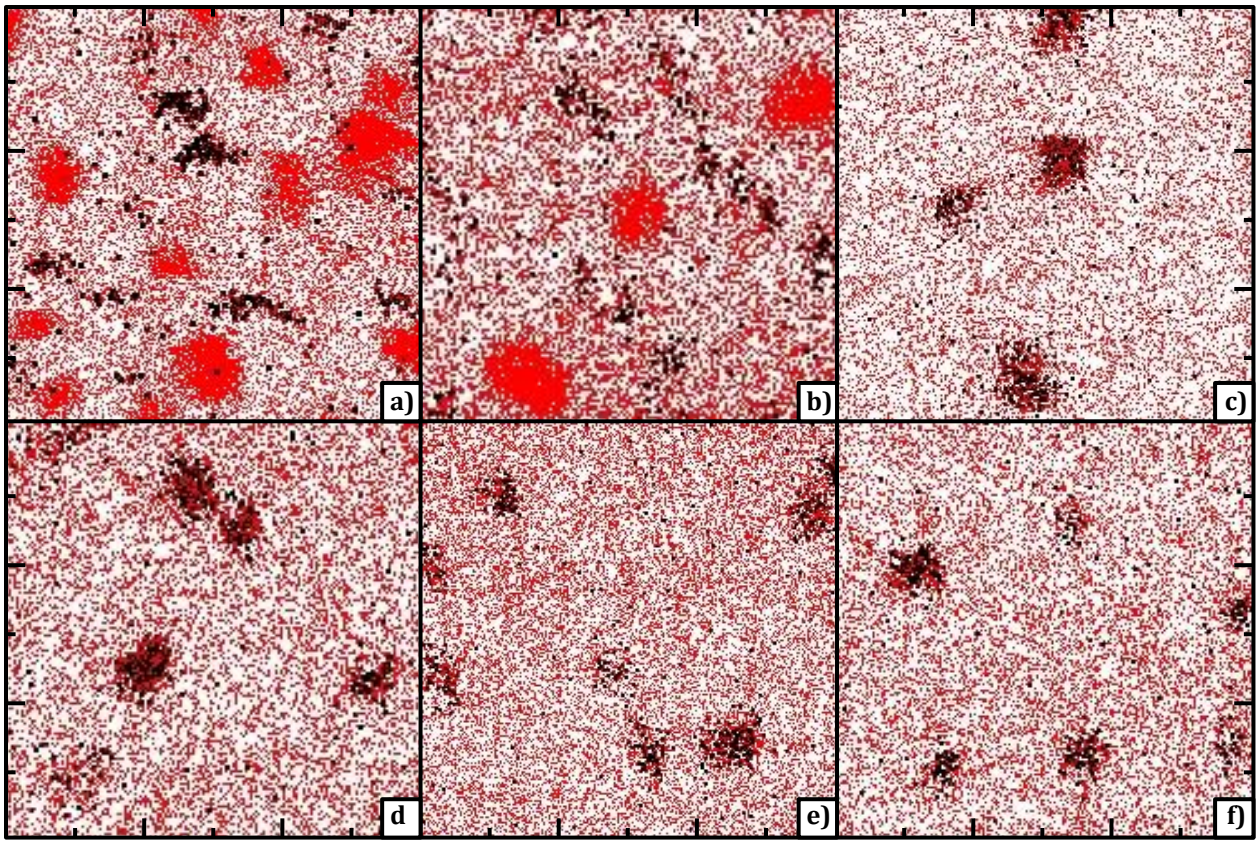

Figure 5.41 Chromium ion distribution (red) and titanium oxide ion distribution (black) as a function of irradiation temperature. Each section is a square region is a slice (30 nm x 30 nm x ~2 nm) taken from a representative area of the reconstruction. Neither the number of chromium enrichments nor the number of titanium oxide clusters in each section are necessarily indicative of the overall densities, but rather are intended to illustrate the clustering character of the chromium ions and the correlation with the titanium oxide clusters. a) 385 °C b) 412 °C c) 495 °C d) 550 °C e) 670 °C f) Control.

An alternative explanation to the varying kinetics is thermodynamically-driven precipitation. Diffusion causes the movement of chromium down a concentration gradient (e.g. away from the oxide interface) to the central area between oxide clusters. Once the chromium has normalized its concentration, then the precipitation process begins, to bring the matrix composition down to the thermodynamically stable level.

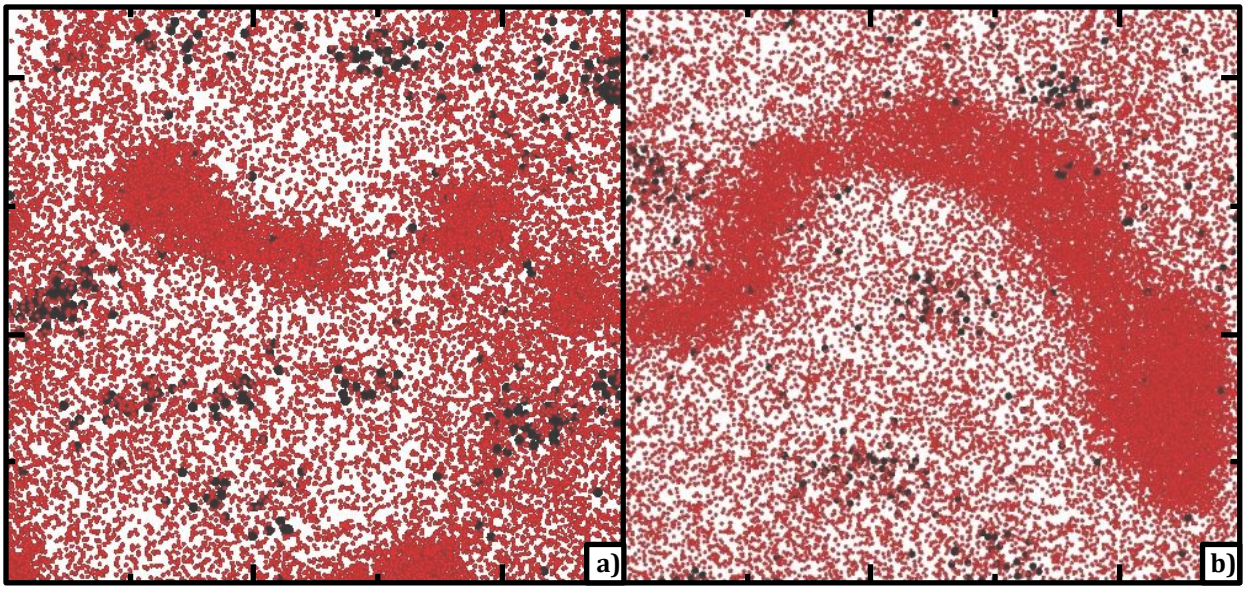

Figure 5.42 Chromium ion distributions illustrating the complex geometries formed by the chromium enrichments in low temperature irradiations. a) 385 °C b) 412 °C

Another secondary phase that was observed in the MA957 samples was g-phase. This is a phase primarily composed of nickel, titanium and silicon. Such precipitates were observed in several, but not all of the TX series samples. In some cases, these precipitates were attached to oxide clusters, in other cases they were not. Such intermetallics are unwanted impurities in the metal, products of the failure to remove all contaminate elements during the creation of the alloy. This shows that there are measurable differences in APT between the TX and EV series MA957, since no g-phase has been observed in any EV series dataset. Differences like this are not surprising, as not only were the TX and EV series specimens from different heats, they were also manufactured using different methodologies.

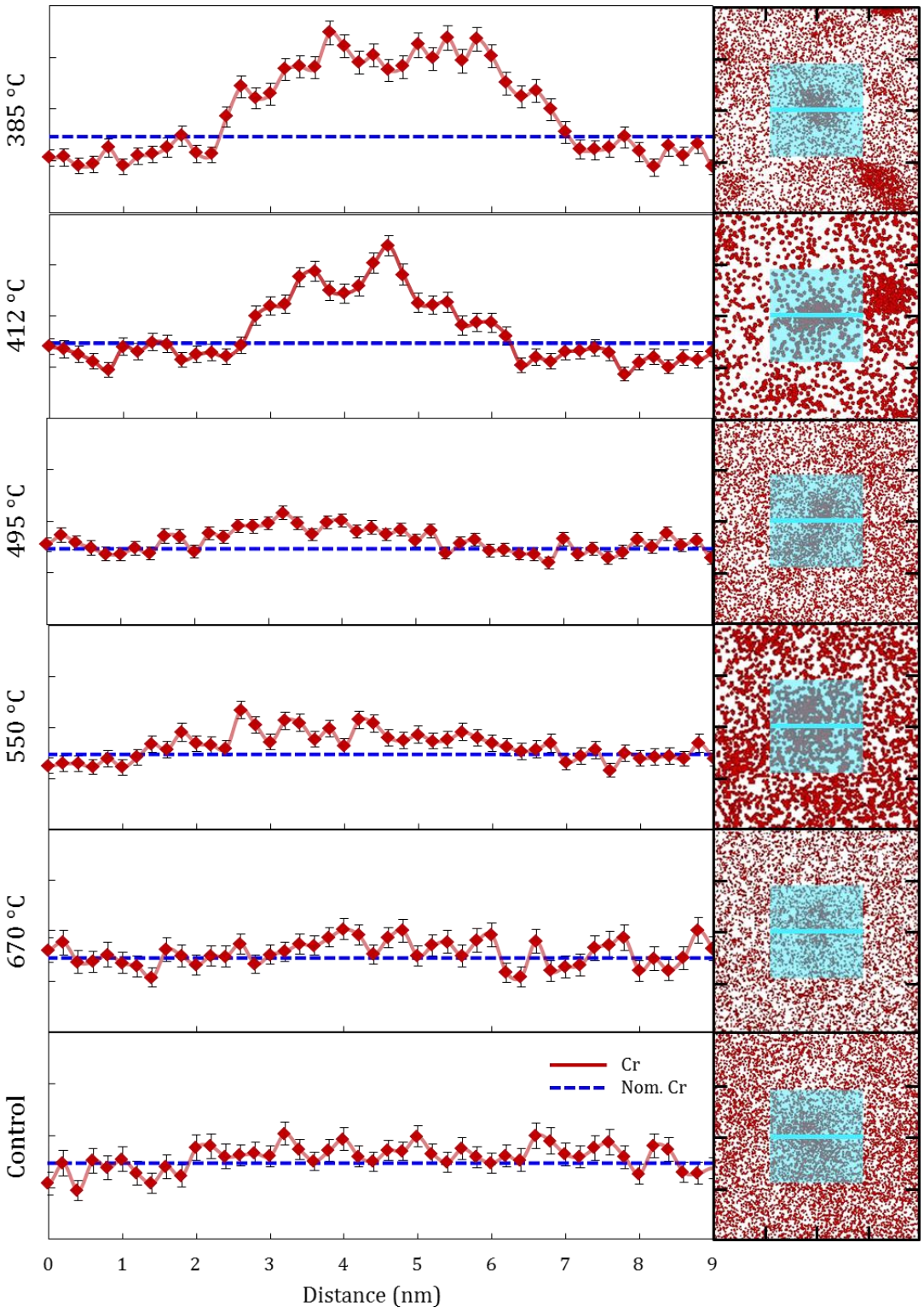

Figure 5.43 1 dimensional compositional linescans of chromium enrichments in the grain bulk across irradiation temperatures. Each plot is scaled to each other, and contains a blue dotted line that indicates the nominal chromium concentration of 14.7% (ionic). On the right, chromium ion distributions are shown with the pale blue box representing the linescan region, and the pale blue line indicating the linescan direction. The linescans used a 0.2 nm bin width.

5.3 Nanoindentation

Figure 4.8 displayed the Berkovich hardness as a function of irradiation temperature. The results of the Berkovich hardness testing experiments matched the trends that were expected based on the initial tensile testing data from PNNL. That is, that the hardness of the control material was comparable to the high irradiation temperature specimens, but a significant increase in hardness is observed in the lower temperature specimens. There is rather significant scatter present in the observed hardness values of the specimens. The scatter is a result of the relatively coarse polishing (relative to indenter tip size) used on the specimens. The activity of the samples prevented finer polishing from being pursued. The increased median hardness values at both 550 °C and 750 °C were due to particularly coarse polishing on those samples, causing surface hardening. Comparing to literature values it was found that the NI data had a systematic increase in hardness from the expected values by 0.5 to 1.0 GPa [106].

No significant change in the reduced modulus was noted as a function of irradiation condition. Since there is no expectation of the elastic modulus to be changed by the irradiation processes, the failure to identify a change in the reduced modulus is not surprising.

6 Conclusions

After irradiation to high dose, the characteristics of the property-controlling Y-Ti-O oxide particles have been investigated using APT. The mechanical response of the specimens has also been investigated with nanoindentation. At irradiation temperatures of 412 °C and below, a substantial increase in oxide cluster number density and decrease in oxide cluster size has been observed. A substantial increase in hardness was also observed at these irradiation conditions. This study demonstrated that the reformation processes for the oxide particles following ballistic dissolution by incident radiation is reduced at 412 °C and below. This leads to the observed increase in oxide cluster number density and the reduction in oxide cluster size. Furthermore, the redistribution of solutes from dissolved Y-Ti-O clusters along the grain boundaries at 412 °C and below is thought to induce grain boundary embrittlement, leading to the brittle tensile failure modes observed by collaborating scientists. In addition to the characterization of Y-Ti-O particles, the intermetallic phase α' was observed in the 412 °C and lower irradiation temperature samples. The precipitation of this phase offers further experimental insight into the phase boundary of this low-temperature phase in ferritic alloys with high chromium content. It is suggested that this brittle phase could also play a role in the reduction in total elongation and embrittlement observed in the specimens irradiated at 412 °C and below.

7 References

[1] International Atomic Energy Agency, "IAEA International Peer Review Mission on Mid-and-Long-Term Roadmap Towards the Decomissioning of TEPCO's Fukushima Daiichi Nuclear Power Station Units 1-4," International Atomic Energy Agency, Tokyo and Fukushima Prefecture, 2015.

[2] United States Department of Energy, "A Technology Roadmap for Generation IV Nuclear Energy Systems," 2002.

[3] United States Department of Energy, "Technology Roadmap Update for Generation IV Nuclear Energy Systems," 2014.

[4] International Atomic Energy Agency, "Boiling Water Reactor Simulator with Active Safety Systems," October 2009. [Online]. Available: http://www.iaea.org/NuclearPower/Downloads/Simulators/Conventional.BWR.Manual.2009-10-05.pdf.

[5] International Atomic Energy Agency, "Pressurized Water Reactor Simulator," September 2005. [Online]. Available: http://www-pub.iaea.org/MTCD/publications/PDF/tcs-22_2nd_web.pdf.

[6] T. R. Allen, J. T. Busby, R. L. Klueh, S. A. Maloy and M. B. Toloczko, *Journal of Materials,* vol. 60, pp. 15-23, 2008.

[7] G. R. Odette, M. J. Alinger and B. D. Wirth, *Ann. Rev. Mater. Res.,* vol. 38, pp. 471-503, 2008.

[8] W. Grimes, R. J. Konings and L. Edwards, *Nat. Mater.,* vol. 7, pp. 683-685, 2008.

[9] D. Olander, Fundamental Aspects of Nuclear Reactor Fuel Elements, Springfield, VA: National Technical Information Service, U. S. Dept. of Commerce, 1976.

[10] W. Corwin, T. Burchell, W. Halsey, G. Hayner, Y. Katoh, J. Klett, T. McGreevy, R. Nanstad, W. Ren, L. Snead, R. Stoller and D. Wilson, "Updated Gerenation IV Reactors Integrated Materials Technology Program Plan," U.S. Department of Energy, Oak Ridge, Tennessee, 2005.

[11] S. J. Zinkle and J. T. Busby, *Materials Today,* vol. 12, no. 11, pp. 12-19, 2009.

[12] P. Yvon and F. Carre, *Journal of Nuclear Materials,* vol. 385, pp. 217-222, 2009.

[13] C. Cawthorne and E. J. Fulton, *Nature,* vol. 216, pp. 575-576, 1966.

[14] B. Raj and Vijayalakshmi, "Joint ICTP/IAEA School on Physics and Technology of Fast Reactor Systems," International Atomic Energy Agency, Trieste, Italy, 2009.

[15] R. E. Stoller and L. R. Greenwood, *Journal of Nuclear Materials,* Vols. 271-272, pp. 57-62, 1999.

[16] G. H. Kinchin and R. S. Pease, "The displacement of atoms in solids by radiation," *Reports on progress in physics,* vol. 18, no. 1, p. 1, 1955.

[17] D. G. Cacuci, Handbook of Nuclear Engineering, Karlsruhe, Germany: Springer, 2010.

[18] A. Suoidi, M. Hou, C. S. Becquart and C. Domain, *Journal of Nuclear Materials,* vol. 295, pp. 179-188, 2001.

[19] G. Gottstein, Physical Foundations of Materials Science, New York: Springer, 2004.

[20] R. L. Coble, *Journal of Applied Physics (US),* vol. 34, 1963.

[21] C. Herring, *Journal of applied physics,* vol. 21, no. 5, pp. 437-445, 1950.

[22] N. F. Mott and F. R. N. Nabarro, "Dislocation theory and transient creep," Physical society bristol conference report, Bristol, 1948.

[23] A. D. Brailsford and R. Bullough, *Journal of Nuclear Materials,* vol. 44, no. 2, pp. 121-135, 1972.

[24] J. L. Straalsund, R. W. Powell and B. A. Chin, *Journal of Nuclear Materials,* Vols. 108-109, pp. 299-305, 1982.

[25] C. Cawthorne and E. J. Fulton, *Nature,* vol. 216, pp. 575-576, 1967.

[26] H. R. Brager and J. L. Straalsund, *Journal of Nuclear Materials,* vol. 46, no. 2, pp. 134-158, 1973.

[27] S. D. Harkness, J. A. Tesk and C. Y. Li, *Nuclear Technology,* vol. 9, no. 1, pp. 24-30, 1970.

[28] H. Wiedersich, *Radiation Effects,* vol. 12, no. 1-2, pp. 111-125, 1972.

[29] A. D. Brailsford and R. Bullough, *Journal of Nuclear Materials,* vol. 44, no. 2, pp. 121-135, 1972.

[30] F. A. Nichols, *Journal of Nuclear Materials,* vol. 30, no. 1, pp. 143-165, 1969.

[31] J. J. Fischer, "Dispersion Strengthened Ferritic Alloy for Use in Liquid Metal Fast Breeder Reactors". United States of America Patent 4075010 A, 21 February 1978.

[32] J. Benjamin, *Metall. Trans.,* vol. 1, pp. 2943-2951, 1970.

[33] I. Chant and K. L. Murty, *J. O. M.,* vol. 62, no. 9, pp. 67-74, 2010.

[34] G. B. Alexander and T. K. Glasgow, "A brief history of oxide dispersion-strengthened alloys," in *Mechanical properties of metallic composites*, New York, Marcel Dekker, Inc., 1993, pp. 5-23.

[35] W. D. Coolidge, *Trans. Am. Inst. Electr. Eng.,* vol. 29, p. 961, 1910.

[36] C. S. Smith, *Mining Metall.,* vol. 11, p. 213, 1930.

[37] R. Irmann, *Metallurgia,* vol. 46, p. 125, 1952.

[38] R. Irmann, *Iron Age,* vol. 177, no. 17, p. 104, 1955.

[39] L. J. Bonis and N. J. Grant, *Trans. AIME,* vol. 224, p. 308, 1962.

[40] G. B. P. W. H. Alexander, "Process for Producing Sintered Metals with Dispersed Oxides". U. S. Patent 3019103, 30 Jan. 1962.

[41] B. Bovarnick and H. W. Flood, *Prog. Powder Metallurgy,* vol. 20, p. 64, 1964.

[42] F. V. Lenel and G. S. Ansel, *Powder Metallurgy,* p. 267, 1961.

[43] S. M. Wolf, *Journal of Metals,* vol. 19, no. 6, p. 22, 1967.

[44] M. Quatinez and J. W. Wheeton, "Dispersion-strengthened nickel produced from ultrafine comminuted powders," NASA TN D-5421, 1969.

[45] Y. Wu, J. Ciston, S. Kraemer, N. Bailey, G. R. Odette and P. Hosemann, *Acta Materialia,* vol. 111, pp. 108-115, 2016.

[46] M. B. Toloczko, "Irradiation Effects Studies on MA957," in *The Fuel Cycle R&D Initiative*, 2012.

[47] P. He, M. Klimenkov, R. Lindau and A. Möslang, *J. Nucl. Mat.,* vol. 428, pp. 131-138, 2012.

[48] J. J. Huet and V. Leroy, *Nucl. Technol.,* vol. 24, pp. 216-224, 1975.

[49] M. J. Alinger, G. R. Odette and G. E. Lucas, *J. Nucl. Mat.,* Vols. 307-311, no. 1, pp. 484-489, 2002.

[50] H. Kishimoto, M. J. Alinger, G. Odette and T. Yamamoto, *J. Nucl. Mat.,* Vols. 329-333, no. A, pp. 369-371, 2004.

[51] B. Fournier, A. Steckmeyer, A. Rouffe, J. Malaplate, J. Garnier, M. Ratti, P. Wident, L. Ziolek, I. Tournie, V. Rabeau, J. M. Gentzbittel, T. Kruml and I. Kubena, *J. Nucl. Mat.,* vol. 430, pp. 142-149, 2012.

[52] M. K. Miller and D. T. Hoelzer, *J. Nucl. Mat.,* vol. 418, pp. 307-310, 2011.

[53] G. R. Odette and D. T. Hoelzer, *J.O.M.,* vol. 62, pp. 84-92, 2010.

[54] P. Olier, M. H. Mathon, D. Numes, D. Hamon, L. Toualbie, Y. d. Carlan and L. Chaffron, *J. Nucl. Mat.,* vol. 428, pp. 40-46, 2012.

[55] M. Song, C. Sun, J. Jang, C. H. Han, T. K. Kim, K. T. Hartwig and X. Zhang, *Journal of Alloys and Compounds,* vol. 577, pp. 247-256, 2013.

[56] P. He, T. Liu, A. Möslang, R. Lindau, R. Ziegler, J. Hoffman, P. Kurinsky, L. Commin, P. Vladimirov, S. Nikitenko and M. Silveir, *Mater. Chem. Phys. ,* vol. 136, pp. 990-998, 2012.

[57] J. Ciston, Y. Wu, G. R. Odette and P. Hosemann, "Fusion Materials Semiannual Progress Report for the Period Ending Dec. 31, 2011," 2011.

[58] T. Stan, W. Y, G. R. Odette, K. E. Sickafus, H. A. Dabkowski and B. D. Gaulin, *Metal. Mater. Trans. A,* vol. 44, no. 10, pp. 4505-4512, 2013.

[59] Y. Wu, E. M. Haney, N. J. Cunningham and G. R. Odette, *Acta Mat.,* vol. 60, pp. 3456-3468, 2012.

[60] D. Bhattachararyya, P. Dickerson, G. R. Odette, S. A. Maloy, A. Misra and M. A. Nastasi, *Philos. Mag. A,* vol. 92, pp. 2089-2107, 2012.

[61] J. Ribis, *J. Nucl. Mat.,* vol. 434, pp. 178-188, 2013.

[62] N. J. Cunningham, G. R. Odette and E. Stergar, "Further Atom Probe Tomography Studies of Nanostructured Ferritic Alloy MA957 in Three Conditions," 2010.

[63] M. B. Toloczko, F. A. Garner and S. A. Maloy, *J. Nucl. Mat.,* vol. 428, pp. 170-175, 2012.

[64] N. Bailey, E. Stergar, M. Toloczko and P. Hosemann, *Microsc. Microanal.,* vol. 18, no. 2, pp. 1418-1419, 2012.

[65] M. K. Miller, D. T. Hoelzer, E. A. Kenik and K. F. Russell, *Microsc. Microanal.,* vol. 10, no. 2, pp. 708-709, 2004.

[66] M. B. Toloczko, A. G. Certain, P. Hosemann and N. Bailey, "Update on Effect of Irradiation on Microstructure and Tensile Properties of MA957," in *The Fuel Cycle R&D Initiative*, 2013.

[67] A. M. Ermi, L. R. Greenwood and H. L. Heinisch, "Irradiation Parameters for the FFTF Materials Open Test Assemblies from 1983 to 1992," 1994.

[68] M. Toloczko and F. Garner, "ASTM STP 1447," *ASTM International,* pp. 454-467, 2004.

[69] M. B. Toloczko, F. A. Garner and C. R. Eiholzer, *Journal of Nuclear Materials,* Vols. 258-263, no. 2, pp. 1163-1166, 1998.

[70] P. Hosemann, Y. Dai, E. Stergar, H. Leitner, E. Olivas, A. Nelson and S. Maloy, *Exp. Mech.,* vol. 51, pp. 1095-1102, 2011.

[71] P. Hosemann, E. Stergar, L. Peng, Y. Dai, S. A. Maloy, M. A. Pouchon, K. Shiba, D. Hamaguchi and H. Leitner, *J. Nucl. Mat.,* vol. 417, no. 1-3, pp. 274-278, 2011.

[72] R. Rachbauer, S. Massl, E. Stergar, P. Felfer and P. H. Mayrhofer, *Surf. Coat. Technol.,* vol. 204, pp. 1811-1816, 2010.

[73] D. J. Larson, D. T. Foord, A. K. Petford-Long, T. C. Anthony, I. M. Rozdilsky, A. Cerezo and G. W. D. Smith, *Ultramicroscopy,* vol. 75, no. 3, pp. 147-159, 1998.

[74] M. K. Miller, K. F. Russel, K. Thompson, R. Alvis and D. J. Larson, *Microsc. and Microanal.,* vol. 13, no. 6, pp. 428-436, 2007.

[75] B. Gault, M. P. Moody, J. M. Cairney and S. P. Ringer, Atom Probe Microscopy, Springer Series in Materials Science, 2012.

[76] D. J. Larson, T. J. Prosa, R. M. Ulfig, B. P. Geiser and T. F. Kelly, Local Electrode Atom Probe Tomography: A User's Guide, New York: Springer, 2013.

[77] E. W. Muller, *Z. Phys.,* vol. 120, no. 5-6, pp. 270-282, 1943.

[78] E. W. Muller, *Z. Phys.,* vol. 131, no. 1, pp. 136-142, 1951.

[79] E. W. Muller, *Journal of Applied Physics,* vol. 27, no. 5, pp. 474-476, 1956.

[80] Cameca, Cameca, [Online]. Available: http://www.cameca.com/instruments-for-research/leap5000.aspx. [Accessed 6 7 2016].

[81] R. Gomer and L. W. Swanson, *J. Chem. Phys.,* vol. 38, p. 1613, 1963.

[82] R. K. Biswas and R. G. Forbes, *J. Phys. D: Appl. Phys.,* vol. 15, no. 7, pp. 1323-1338, 1982.

[83] R. G. Forbes, *J. Phys. D: Appl. Phys.,* vol. 15, no. 11, pp. L149-L152, 1982.

[84] K. Chibane and R. G. Forbes, *Surf. Sci.,* vol. 122, no. 2, pp. 191-215, 1982.

[85] R. Gomer, *J. Chem. Phys.,* vol. 31, p. 341, 1959.

[86] K. Hirose and M. Tsukada, *Phys. Rev. Lett.,* vol. 73, no. 1, p. 150, 1994.

[87] Cameca Inc., "IVAS User Guide, Version: 3.6.6," 29 Quai des Grésillons, 92622 Gennevilliers Cedex (France), 2014.

[88] R. Gomer, Field Emission and Field Ionisation, Cambridge: Harvard University, 1961.

[89] D. J. Bacon, U. F. Kocks and R. O. Scattergood, *Philosophical Magazine,* vol. 28, no. 6, pp. 1241-1263, 1973.

[90] H. C. Romesburg, Cluster analysis for researchers, North Carolina: Lulu Press, 2004.

[91] E. A. Marquis and J. M. Hyde, *Materials Science and Engineering R,* vol. 69, pp. 37-62, 2010.

[92] L. T. Stephenson, M. P. Moody, B. Gault and S. P. Ringer, *Philos. Mag. A,* vol. 93, no. 8, pp. 975-989, 2013.

[93] L. T. Stephenson, M. P. Moody, P. V. Liddicoat and S. P. Ringer, *Microsc. Microanal.,* vol. 13, p. 448, 2007.

[94] J. M. Hyde, E. A. Marquis, K. B. Wilford and T. J. Williams, *Ultramicroscopy,* vol. 111, pp. 440-447, 2011.

[95] J. M. Hyde and C. A. English, "An Analysis of the Structure of Irradiation Induced Cu-enriched Clusters in Low and High Nickel Reactor Pressure Vessel Steels," in *Materials Research Society*, Boston, MA, 2000.

[96] R. P. Kolli and D. N. Seidman, *Microscopy and Microanalysis,* vol. 13, pp. 272-284, 2007.

[97] J. M. Hyde and C. A. English, *Mat. Res. Soc. Symp. Porc.,* vol. 650, pp. R6.6.1-R6.6.12, 2000.

[98] C. A. Williams, D. Haley, E. A. Marquis, G. D. W. Smith and M. P. Moody, *Ultramicroscopy,* vol. 132, pp. 271-278, 2013.

[99] W. C. Oliver and G. M. Pharr, *Journal of Materials Research,* vol. 7, no. 6, pp. 1564-1583, 1992.

[100] W. C. Oliver and G. M. Pfarr, *Journal of Materials Research,* vol. 19, no. 1, pp. 3-20, 2004.

[101] J. R. Riley, R. A. Bernal, Q. Li, H. D. Espinosa, G. T. Wang and L. J. Lauhon, "Atom probe tomography of a-axis GaN nanowires: analysis of nonstoichiometric evaporation behavior," *ACS Nano,* vol. 6, no. 5, pp. 3898-3906, 2012.

[102] H. Sakasegawa, L. Chaffron, F. Legendre, L. Boulanger and M. B. Y. d. C. T. Cozzika, "Correlation between chemical composition and size of very small oxide particles in the MA957 ODS ferritic alloy," *Journal of Nuclear Materials,* vol. 384, no. 2, pp. 115-118, 2009.

[103] A. Kolmogorov, *G. Ist. Attuari,* vol. 4, pp. 83-91, 1933.

[104] N. Smirnov, *Annals of Mathematical Statistics,* vol. 19, pp. 279-281, 1948.

[105] O. Anderglu, *Journal of Nuclear Materials,* vol. 430, pp. 194-204, 2012.

[106] P. Dayal, D. Bhattacharyya, W. M. Mook, E. G. Fu, Y. Q. Wang, D. G. Carr, O. Anderoglu, N. A. Mara, A. Misra, R. P. Harrison and L. Edwards, *Journal of Nuclear Materials,* vol. 438, no. 1-3, pp. 108-115.

[107] D. Vaumousse, A. Cerezo and P. Warren, *Ultramicroscopy,* vol. 95, pp. 215-221, 2003.

[108] E. W. Muller, *Phys. Rev.,* vol. 102, no. 3, pp. 618-624, 1956.

[109] S. Ishino, N. Sekimura and H. Abe, "Eff. of Rad. on Mat.: 23th Int. Symp.".

[110] M. B. Toloczko and F. A. Garner, "ASTM STP 1447," in *ASTM International*, West Conshocken, PA, 2004.

[111] U.S. Department of Energy, "GIF R&D Outlook for Generation IV Nuclear Energy Systems," 2009.

[112] Y. K. Rao, Stoichiometry and Thermodynamics of Metallurgical Processes, Cambridge, NY: Cambridge University Press, 1985.

[113] G. R. Odette, P. J. Maziasz and J. A. Spitznagel, *J. Nucl. Mat.,* vol. 103, p. 1239, 1981.

[114] L. K. Mansur and W. A. Coughlan, *J. Nucl. Mat.,* vol. 119, pp. 1-25, 1983.

[115] R. E. Stoller and G. R. Odette, "Eff. of Rad. on Mat.: 13th Int. Symp.".

[116] P. J. Maziasz, *J. Nucl. Mat.,* vol. 205, p. 118, 1993.

[117] H. Trinkaus, *J. Nucl. Mat.,* vol. 118, p. 39, 1983.

[118] G. R. Odette, *J. Nucl. Mat.,* Vols. 155-157, p. 921, 1988.

8 Bibliography

[1] International Atomic Energy Agency, "IAEA International Peer Review Mission on Mid-and-Long-Term Roadmap Towards the Decomissioning of TEPCO's Fukushima Daiichi Nuclear Power Station Units 1-4," International Atomic Energy Agency, Tokyo and Fukushima Prefecture, 2015.

[2] United States Department of Energy, "A Technology Roadmap for Generation IV Nuclear Energy Systems," 2002.

[3] United States Department of Energy, "Technology Roadmap Update for Generation IV Nuclear Energy Systems," 2014.

[4] International Atomic Energy Agency, "Boiling Water Reactor Simulator with Active Safety Systems," October 2009. [Online]. Available: http://www.iaea.org/NuclearPower/Downloads/Simulators/Conventional.BWR.Manual.2009-10-05.pdf.

[5] International Atomic Energy Agency, "Pressurized Water Reactor Simulator," September 2005. [Online]. Available: http://www-pub.iaea.org/MTCD/publications/PDF/tcs-22_2nd_web.pdf.

[6] T. R. Allen, J. T. Busby, R. L. Klueh, S. A. Maloy and M. B. Toloczko, *Journal of Materials,* vol. 60, pp. 15-23, 2008.

[7] G. R. Odette, M. J. Alinger and B. D. Wirth, *Ann. Rev. Mater. Res.,* vol. 38, pp. 471-503, 2008.

[8] W. Grimes, R. J. Konings and L. Edwards, *Nat. Mater.,* vol. 7, pp. 683-685, 2008.

[9] D. Olander, Fundamental Aspects of Nuclear Reactor Fuel Elements, Springfield, VA: National Technical Information Service, U. S. Dept. of Commerce, 1976.

[10] W. Corwin, T. Burchell, W. Halsey, G. Hayner, Y. Katoh, J. Klett, T. McGreevy, R. Nanstad, W. Ren, L. Snead, R. Stoller and D. Wilson, "Updated Gerenation IV Reactors Integrated Materials Technology Program Plan," U.S. Department of Energy, Oak Ridge, Tennessee, 2005.

[11] S. J. Zinkle and J. T. Busby, *Materials Today,* vol. 12, no. 11, pp. 12-19, 2009.

[12] P. Yvon and F. Carre, *Journal of Nuclear Materials,* vol. 385, pp. 217-222, 2009.

[13] C. Cawthorne and E. J. Fulton, *Nature,* vol. 216, pp. 575-576, 1966.

[14] B. Raj and Vijayalakshmi, "Joint ICTP/IAEA School on Physics and Technology of Fast Reactor Systems," International Atomic Energy Agency, Trieste, Italy, 2009.

[15] R. E. Stoller and L. R. Greenwood, *Journal of Nuclear Materials,* Vols. 271-272, pp. 57-62, 1999.

[16] G. H. Kinchin and R. S. Pease, "The displacement of atoms in solids by radiation," *Reports on progress in physics,* vol. 18, no. 1, p. 1, 1955.

[17] D. G. Cacuci, Handbook of Nuclear Engineering, Karlsruhe, Germany: Springer, 2010.

[18] A. Suoidi, M. Hou, C. S. Becquart and C. Domain, *Journal of Nuclear Materials,* vol. 295, pp. 179-188, 2001.

[19] G. Gottstein, Physical Foundations of Materials Science, New York: Springer, 2004.

[20] R. L. Coble, *Journal of Applied Physics (US),* vol. 34, 1963.

[21] C. Herring, *Journal of applied physics,* vol. 21, no. 5, pp. 437-445, 1950.

[22] N. F. Mott and F. R. N. Nabarro, "Dislocation theory and transient creep," Physical society bristol conference report, Bristol, 1948.

[23] A. D. Brailsford and R. Bullough, *Journal of Nuclear Materials,* vol. 44, no. 2, pp. 121-135, 1972.

[24] J. L. Straalsund, R. W. Powell and B. A. Chin, *Journal of Nuclear Materials,* Vols. 108-109, pp. 299-305, 1982.

[25] C. Cawthorne and E. J. Fulton, *Nature,* vol. 216, pp. 575-576, 1967.

[26] H. R. Brager and J. L. Straalsund, *Journal of Nuclear Materials,* vol. 46, no. 2, pp. 134-158, 1973.

[27] S. D. Harkness, J. A. Tesk and C. Y. Li, *Nuclear Technology,* vol. 9, no. 1, pp. 24-30, 1970.

[28] H. Wiedersich, *Radiation Effects,* vol. 12, no. 1-2, pp. 111-125, 1972.

[29] A. D. Brailsford and R. Bullough, *Journal of Nuclear Materials,* vol. 44, no. 2, pp. 121-135, 1972.

[30] F. A. Nichols, *Journal of Nuclear Materials,* vol. 30, no. 1, pp. 143-165, 1969.

[31] J. J. Fischer, "Dispersion Strengthened Ferritic Alloy for Use in Liquid Metal Fast Breeder Reactors". United States of America Patent 4075010 A, 21 February 1978.

[32] J. Benjamin, *Metall. Trans.,* vol. 1, pp. 2943-2951, 1970.

[33] I. Chant and K. L. Murty, *J. O. M.,* vol. 62, no. 9, pp. 67-74, 2010.

[34] G. B. Alexander and T. K. Glasgow, "A brief history of oxide dispersion-strengthened alloys," in *Mechanical properties of metallic composites*, New York, Marcel Dekker, Inc., 1993, pp. 5-23.

[35] W. D. Coolidge, *Trans. Am. Inst. Electr. Eng.,* vol. 29, p. 961, 1910.

[36] C. S. Smith, *Mining Metall.,* vol. 11, p. 213, 1930.

[37] R. Irmann, *Metallurgia,* vol. 46, p. 125, 1952.

[38] R. Irmann, *Iron Age,* vol. 177, no. 17, p. 104, 1955.

[39] L. J. Bonis and N. J. Grant, *Trans. AIME,* vol. 224, p. 308, 1962.

[40] G. B. P. W. H. Alexander, "Process for Producing Sintered Metals with Dispersed Oxides". U. S. Patent 3019103, 30 Jan. 1962.

[41] B. Bovarnick and H. W. Flood, *Prog. Powder Metallurgy,* vol. 20, p. 64, 1964.

[42] F. V. Lenel and G. S. Ansel, *Powder Metallurgy,* p. 267, 1961.

[43] S. M. Wolf, *Journal of Metals,* vol. 19, no. 6, p. 22, 1967.

[44] M. Quatinez and J. W. Wheeton, "Dispersion-strengthened nickel produced from ultrafine comminuted powders," NASA TN D-5421, 1969.

[45] Y. Wu, J. Ciston, S. Kraemer, N. Bailey, G. R. Odette and P. Hosemann, *Acta Materialia,* vol. 111, pp. 108-115, 2016.

[46] M. B. Toloczko, "Irradiation Effects Studies on MA957," in *The Fuel Cycle R&D*

Initiative, 2012.

[47] P. He, M. Klimenkov, R. Lindau and A. Möslang, *J. Nucl. Mat.,* vol. 428, pp. 131-138, 2012.

[48] J. J. Huet and V. Leroy, *Nucl. Technol.,* vol. 24, pp. 216-224, 1975.

[49] M. J. Alinger, G. R. Odette and G. E. Lucas, *J. Nucl. Mat.,* Vols. 307-311, no. 1, pp. 484-489, 2002.

[50] H. Kishimoto, M. J. Alinger, G. Odette and T. Yamamoto, *J. Nucl. Mat.,* Vols. 329-333, no. A, pp. 369-371, 2004.

[51] B. Fournier, A. Steckmeyer, A. Rouffe, J. Malaplate, J. Garnier, M. Ratti, P. Wident, L. Ziolek, I. Tournie, V. Rabeau, J. M. Gentzbittel, T. Kruml and I. Kubena, *J. Nucl. Mat.,* vol. 430, pp. 142-149, 2012.

[52] M. K. Miller and D. T. Hoelzer, *J. Nucl. Mat.,* vol. 418, pp. 307-310, 2011.

[53] G. R. Odette and D. T. Hoelzer, *J.O.M.,* vol. 62, pp. 84-92, 2010.

[54] P. Olier, M. H. Mathon, D. Numes, D. Hamon, L. Toualbie, Y. d. Carlan and L. Chaffron, *J. Nucl. Mat.,* vol. 428, pp. 40-46, 2012.

[55] M. Song, C. Sun, J. Jang, C. H. Han, T. K. Kim, K. T. Hartwig and X. Zhang, *Journal of Alloys and Compounds,* vol. 577, pp. 247-256, 2013.

[56] P. He, T. Liu, A. Möslang, R. Lindau, R. Ziegler, J. Hoffman, P. Kurinsky, L. Commin, P. Vladimirov, S. Nikitenko and M. Silveir, *Mater. Chem. Phys. ,* vol. 136, pp. 990-998, 2012.

[57] J. Ciston, Y. Wu, G. R. Odette and P. Hosemann, "Fusion Materials Semiannual Progress Report for the Period Ending Dec. 31, 2011," 2011.

[58] T. Stan, W. Y, G. R. Odette, K. E. Sickafus, H. A. Dabkowski and B. D. Gaulin, *Metal. Mater. Trans. A,* vol. 44, no. 10, pp. 4505-4512, 2013.

[59] Y. Wu, E. M. Haney, N. J. Cunningham and G. R. Odette, *Acta Mat.,* vol. 60, pp. 3456-3468, 2012.

[60] D. Bhattachararyya, P. Dickerson, G. R. Odette, S. A. Maloy, A. Misra and M. A.

Nastasi, *Philos. Mag. A,* vol. 92, pp. 2089-2107, 2012.

[61] J. Ribis, *J. Nucl. Mat.,* vol. 434, pp. 178-188, 2013.

[62] N. J. Cunningham, G. R. Odette and E. Stergar, "Further Atom Probe Tomography Studies of Nanostructured Ferritic Alloy MA957 in Three Conditions," 2010.

[63] M. B. Toloczko, F. A. Garner and S. A. Maloy, *J. Nucl. Mat.,* vol. 428, pp. 170-175, 2012.

[64] N. Bailey, E. Stergar, M. Toloczko and P. Hosemann, *Microsc. Microanal.,* vol. 18, no. 2, pp. 1418-1419, 2012.

[65] M. K. Miller, D. T. Hoelzer, E. A. Kenik and K. F. Russell, *Microsc. Microanal.,* vol. 10, no. 2, pp. 708-709, 2004.

[66] M. B. Toloczko, A. G. Certain, P. Hosemann and N. Bailey, "Update on Effect of Irradiation on Microstructure and Tensile Properties of MA957," in *The Fuel Cycle R&D Initiative*, 2013.

[67] A. M. Ermi, L. R. Greenwood and H. L. Heinisch, "Irradiation Parameters for the FFTF Materials Open Test Assemblies from 1983 to 1992," 1994.

[68] M. Toloczko and F. Garner, "ASTM STP 1447," *ASTM International,* pp. 454-467, 2004.

[69] M. B. Toloczko, F. A. Garner and C. R. Eiholzer, *Journal of Nuclear Materials,* Vols. 258-263, no. 2, pp. 1163-1166, 1998.

[70] P. Hosemann, Y. Dai, E. Stergar, H. Leitner, E. Olivas, A. Nelson and S. Maloy, *Exp. Mech.,* vol. 51, pp. 1095-1102, 2011.

[71] P. Hosemann, E. Stergar, L. Peng, Y. Dai, S. A. Maloy, M. A. Pouchon, K. Shiba, D. Hamaguchi and H. Leitner, *J. Nucl. Mat.,* vol. 417, no. 1-3, pp. 274-278, 2011.

[72] R. Rachbauer, S. Massl, E. Stergar, P. Felfer and P. H. Mayrhofer, *Surf. Coat. Technol.,* vol. 204, pp. 1811-1816, 2010.

[73] D. J. Larson, D. T. Foord, A. K. Petford-Long, T. C. Anthony, I. M. Rozdilsky, A. Cerezo and G. W. D. Smith, *Ultramicroscopy,* vol. 75, no. 3, pp. 147-159, 1998.

[74] M. K. Miller, K. F. Russel, K. Thompson, R. Alvis and D. J. Larson, *Microsc. and*

Microanal., vol. 13, no. 6, pp. 428-436, 2007.

[75] B. Gault, M. P. Moody, J. M. Cairney and S. P. Ringer, Atom Probe Microscopy, Springer Series in Materials Science, 2012.

[76] D. J. Larson, T. J. Prosa, R. M. Ulfig, B. P. Geiser and T. F. Kelly, Local Electrode Atom Probe Tomography: A User's Guide, New York: Springer, 2013.

[77] E. W. Muller, *Z. Phys.,* vol. 120, no. 5-6, pp. 270-282, 1943.

[78] E. W. Muller, *Z. Phys.,* vol. 131, no. 1, pp. 136-142, 1951.

[79] E. W. Muller, *Journal of Applied Physics,* vol. 27, no. 5, pp. 474-476, 1956.

[80] Cameca, Cameca, [Online]. Available: http://www.cameca.com/instruments-for-research/leap5000.aspx. [Accessed 6 7 2016].

[81] R. Gomer and L. W. Swanson, *J. Chem. Phys.,* vol. 38, p. 1613, 1963.

[82] R. K. Biswas and R. G. Forbes, *J. Phys. D: Appl. Phys.,* vol. 15, no. 7, pp. 1323-1338, 1982.

[83] R. G. Forbes, *J. Phys. D: Appl. Phys.,* vol. 15, no. 11, pp. L149-L152, 1982.

[84] K. Chibane and R. G. Forbes, *Surf. Sci.,* vol. 122, no. 2, pp. 191-215, 1982.

[85] R. Gomer, *J. Chem. Phys.,* vol. 31, p. 341, 1959.

[86] K. Hirose and M. Tsukada, *Phys. Rev. Lett.,* vol. 73, no. 1, p. 150, 1994.

[87] Cameca Inc., "IVAS User Guide, Version: 3.6.6," 29 Quai des Grésillons, 92622 Gennevilliers Cedex (France), 2014.

[88] R. Gomer, Field Emission and Field Ionisation, Cambridge: Harvard University, 1961.

[89] D. J. Bacon, U. F. Kocks and R. O. Scattergood, *Philosophical Magazine,* vol. 28, no. 6, pp. 1241-1263, 1973.

[90] H. C. Romesburg, Cluster analysis for researchers, North Carolina: Lulu Press, 2004.

[91] E. A. Marquis and J. M. Hyde, *Materials Science and Engineering R,* vol. 69, pp. 37-62,

2010.

[92] L. T. Stephenson, M. P. Moody, B. Gault and S. P. Ringer, *Philos. Mag. A,* vol. 93, no. 8, pp. 975-989, 2013.

[93] L. T. Stephenson, M. P. Moody, P. V. Liddicoat and S. P. Ringer, *Microsc. Microanal.,* vol. 13, p. 448, 2007.

[94] J. M. Hyde, E. A. Marquis, K. B. Wilford and T. J. Williams, *Ultramicroscopy,* vol. 111, pp. 440-447, 2011.

[95] J. M. Hyde and C. A. English, "An Analysis of the Structure of Irradiation Induced Cu-enriched Clusters in Low and High Nickel Reactor Pressure Vessel Steels," in *Materials Research Society*, Boston, MA, 2000.

[96] R. P. Kolli and D. N. Seidman, *Microscopy and Microanalysis,* vol. 13, pp. 272-284, 2007.

[97] J. M. Hyde and C. A. English, *Mat. Res. Soc. Symp. Porc.,* vol. 650, pp. R6.6.1-R6.6.12, 2000.

[98] C. A. Williams, D. Haley, E. A. Marquis, G. D. W. Smith and M. P. Moody, *Ultramicroscopy,* vol. 132, pp. 271-278, 2013.

[99] W. C. Oliver and G. M. Pharr, *Journal of Materials Research,* vol. 7, no. 6, pp. 1564-1583, 1992.

[100] W. C. Oliver and G. M. Pfarr, *Journal of Materials Research,* vol. 19, no. 1, pp. 3-20, 2004.

[101] J. R. Riley, R. A. Bernal, Q. Li, H. D. Espinosa, G. T. Wang and L. J. Lauhon, "Atom probe tomography of a-axis GaN nanowires: analysis of nonstoichiometric evaporation behavior," *ACS Nano,* vol. 6, no. 5, pp. 3898-3906, 2012.

[102] H. Sakasegawa, L. Chaffron, F. Legendre, L. Boulanger and M. B. Y. d. C. T. Cozzika, "Correlation between chemical composition and size of very small oxide particles in the MA957 ODS ferritic alloy," *Journal of Nuclear Materials,* vol. 384, no. 2, pp. 115-118, 2009.

[103] A. Kolmogorov, *G. Ist. Attuari,* vol. 4, pp. 83-91, 1933.

[104] N. Smirnov, *Annals of Mathematical Statistics,* vol. 19, pp. 279-281, 1948.

[105] O. Anderglu, *Journal of Nuclear Materials,* vol. 430, pp. 194-204, 2012.

[106] P. Dayal, D. Bhattacharyya, W. M. Mook, E. G. Fu, Y. Q. Wang, D. G. Carr, O. Anderoglu, N. A. Mara, A. Misra, R. P. Harrison and L. Edwards, *Journal of Nuclear Materials,* vol. 438, no. 1-3, pp. 108-115.

[107] D. Vaumousse, A. Cerezo and P. Warren, *Ultramicroscopy,* vol. 95, pp. 215-221, 2003.

[108] E. W. Muller, *Phys. Rev.,* vol. 102, no. 3, pp. 618-624, 1956.

[109] S. Ishino, N. Sekimura and H. Abe, "Eff. of Rad. on Mat.: 23th Int. Symp.".

[110] M. B. Toloczko and F. A. Garner, "ASTM STP 1447," in *ASTM International*, West Conshocken, PA, 2004.

[111] U.S. Department of Energy, "GIF R&D Outlook for Generation IV Nuclear Energy Systems," 2009.

[112] Y. K. Rao, Stoichiometry and Thermodynamics of Metallurgical Processes, Cambridge, NY: Cambridge University Press, 1985.

[113] G. R. Odette, P. J. Maziasz and J. A. Spitznagel, *J. Nucl. Mat.,* vol. 103, p. 1239, 1981.

[114] L. K. Mansur and W. A. Coughlan, *J. Nucl. Mat.,* vol. 119, pp. 1-25, 1983.

[115] R. E. Stoller and G. R. Odette, "Eff. of Rad. on Mat.: 13th Int. Symp.".

[116] P. J. Maziasz, *J. Nucl. Mat.,* vol. 205, p. 118, 1993.

[117] H. Trinkaus, *J. Nucl. Mat.,* vol. 118, p. 39, 1983.

[118] G. R. Odette, *J. Nucl. Mat.,* Vols. 155-157, p. 921, 1988.